Nonlinear optical microscopy for tissue imaging and analysis in anatomic pathology

Kseniya S. Shin

A dissertation
submitted in partial fulfillment of the
requirements for the degree of

Doctor of Philosophy

University of Washington

2020

Reading Committee:

Dan Fu, Chair

Joshua C. Vaughan

Cody Schlenker

Program Authorized to Offer Degree:
Chemistry

University of Washington

Abstract

Nonlinear optical microscopy for tissue imaging and analysis in anatomic pathology

Kseniya S. Shin

Chair of the Supervisory Committee:
Chair Dan Fu
Department of Chemistry

Stimulated Raman Scattering (SRS) microscopy provides chemical information for imaged tissue at submicron resolution. In the experiments described, I combine SRS with other non-linear microscopies, including second harmonic generation (SHG) microscopy and two-photon fluorescence (TPF) microscopy, to develop a methodology for tissue imaging and analysis with anatomic pathology diagnostic challenges in mind. Employing an interdisciplinary approach in collaboration with experts in the field I investigate the diagnostic potential of a multimodal approach to complex tissues such as brain, breast, and bone, illuminating the immense potential non-linear optical microscopy has to offer to pathologists and clinicians as they strive to improve patient care.

TABLE OF CONTENTS

LIST OF FIGURES

LIST OF TABLES

ACKNOWLEDGMENTS

First, I must acknowledge the land the University of Washington is on and the people, past and present. The university that has become my home is located on the unceded ancestral land of the Duwamish people, and in acknowledging that this is the Duwamish traditional land, I resist the erasure of indigenous histories. Additionally, I assert my full commitment as I work towards honoring and inviting the truth and hopefully contributing to the subsequent healing of our community.

The work presented in this dissertation and work that happened outside of my research is an accomplishment I cannot credit myself alone. There are many teachers, mentors, colleagues, friends, family, and even strangers who have contributed stones for the foundation that supported me in this journey.

I honor my parents for bringing me into this life and providing an early crucial opportunity to attend school across the world from home. You did so despite the astonishing reservations you experienced as anybody would when sending their child into a foreign country for a better future. I know it was an immense sacrifice. Twenty years of my life passed, and you, my parents, were patient as you saw merely pictures of important milestones and marched on your separate route. At the same time, the losses have paved a way to my many dreams being realized in the ways that make me know that I am unequivocally a very fortunate person.

I thank my most loyal friend, partner, and love, Joshua Aldrich, who always has faith in my strength and resilience and was always there at the most needed time to remind me. As a true partner in life, I am so happy to share this accomplishment with you.

I thank my children for simply being them and challenging me in ways I did not know one

could and stimulating the type of growth of which I never thought I was capable. Parenting them made me deeply understand the quote by Chief Seattle, "We do not inherit the Earth from our ancestors: we borrow it from our children."

I thank the elder NormaAlicia Pino (Purépecha/Comcáac/Guaicura) for so many gifts of wisdom that I will continue to rely on for many years to come. I also thank Uncle Phil Dan (Swinomish) for welcoming me into his family. Your hope and charge will not be forgotten. May you rest in peace.

I would like to acknowledge the support of our current and former research group members (Andrew Francis, Benjamin Figueroa, Bryce Manifold, Nora Munger, Andrew Hill, and Fiona Xu). In particular, I would like to thank Andrew Francis for sharing the office with me and providing timely and necessary feedback, ideas, and inspirations for research. I want to thank Nora Munger and Elena Thomas for their support in challenging times. Additionally, I would like to thank the undergraduate students who worked closely with me, including Mint Laohajaratsang, Helen Men, Angel Wong, Garrett Britt, Rachel Hu, and Colburn Cobb-Bruno. It has been my privilege to teach, mentor, and learn so much from you all.

I want to thank Eleanor Chen, Suzanne Dintzis, and Gordana Juric-Sekhar for support and mentorship during my graduate research years. Your expertise, generous time, and resource investment were essential for this work and my growth as a researcher.

Finally, I would like to acknowledge the support of my advisor, Dan Fu. This dissertation is possible in large part because you created the opportunity for me to join your lab, learn from strong colleagues, and learn so much from you as you patiently provided the resources, guidance, crucial advice, and many lessons that only strengthen me as a scientist. My heart is filled with gratitude as I reflect on these last three years.

DEDICATION

Efimiya Samoylova - you encouraged and supported several generations on educational path and sacrificed much in order to do that. Your legacy will live on.

Chapter 1

INTRODUCTION

1.1 Thesis Structure

The work presented in this thesis is organized into 4 major chapters. The first chapter introduces challenges faced by anatomic pathologists as they practice in hospitals in combination with a review of the main microscopy tools utilized in this work. The second through fourth chapters will focus on primary research I conducted and the resulting publications I co-authored.

1.2 Brief Overview: Challenges Experienced in Anatomic Pathology

The inner workings of a pathology service are often obscure to patients and the general public. Pathologists focus on studying disease processes at macro, micro, and molecular levels. The information provided by a pathologist is used by clinicians and health care professionals in direct contact with patients, to determine the course of treatment. There are two main divisions within pathology including clinical and anatomic pathology. A clinical pathologist works with bodily fluids, conducts tests for toxicology, studies and diagnoses blood disorders, researches topics in immunology and serology, investigates and diagnoses infectious diseases in a laboratory setting. Professionals working in anatomic pathology study organs and tissue through gross and microscopic examination and can be divided into sub-specialties of surgical pathology (further subdivided by organ system), cytopathology, and autopsy (hospital or forensic) pathology. The work in this dissertation focuses primarily on anatomic pathology applications, with the remainder of this section discussing the primary challenges faced

by anatomic pathologist as they strive to deliver fast, accurate, and actionable diagnostic information for clinicians.

An anatomic pathologist uses the understanding of the human body's normal structure and function, clinical history, radiographic images, and the ability to consider these facts in tandem with morphological observations to make gross and microscopic diagnosis. The pathology setting dictates the type and complexity of techniques required for microscopic analysis. One such setting that is very time-constrained is surgery, when intraoperative diagnosis can significantly alter the course of treatment. For example, tumor margin assessment is conducted through both gross and microscopic examination to ensure complete removal of lesional tissue. Intraoperative microscopic examination is done using cryosectioning of tissue. In order to achieve this, the submitted tissues is embedded into an optimal cutting temperature (OCT) compound that is a blend of clear, water-soluble formulations of glycols and resins. A cryostat is used to freeze the tissue to below -20 °C enabling easier sectioning into typically 4 μm thick sections. The sections are subsequently fixed and stained with hematoxylin (basophilic and used to highlight chromatin in nuclei) and eosin (acidophilic and used to highlight protein containing components of the cell). Texture heterogeneity poses a challenge during cryosectioning. Such texture heterogeneity can often show up as a freeze artefact - the diffuse or focal splitting of sections or cellular rarefaction resulting in a loss of diagnostic information. Freeze artefacts can result in misinterpretations and subsequent diagnostic pitfalls. This is particularly common in fatty or myxoid tissue. Furthermore, tissues like bone and other mineralized samples are difficult to cut and frequently only gross examination is conducted. The final examination for such samples is deferred until after surgery so that demineralization using acids can be performed.

Another setting that permits the use of more complex tools is after biopsy or surgery where a comprehensive analysis of a specimen is conducted to address pertinent questions including the primary diagnosis of a lesion, extent of disease, prognostic markers guiding treatment, among others. Microscopic evaluation of biopsied or resected tissue also uses H&E stained tissue slides to facilitate morphological observations. When warranted by a

diagnostic protocol, special stains, immunohistochemistry, cytogenetics, and fluorescence microscopy are executed on tissue slides. The methods necessary to produce tissue slides for a pathologist's interpretation are not trivial and require a team of professionals, including histologists who continuously work to optimize tissue processing methods. Such efforts are crucial for generating tissue slides adequate for examination by a pathologist. In addition to the effort required, techniques like paraffin embedding are a time consuming process requiring at least 24 hours turn around time before the slides are available for examination. Tissue processing also involves many solvents that are costly from a budgetary point of view as well as our planet's health. After cost of labor and resources, the resulting histology is not without challenging artefacts that need to be accounted for when interpreting the slides. Similar to intraoperative frozen sections that can have freeze artefacts, the formalin fixed paraffin embedded (FFPE) sections can suffer from tissue retraction with many features being distorted. Therefore, there are many shortcomings that demand development of new and improved techniques.

Despite the challenges described, it is important to acknowledge the immense value of histology in medical diagnosis and prognosis. Current pathology practice delivers actionable information for managing as well as enhancing our understanding of disease. Moreover, the integrity of diagnostic information can impact in profound ways patients' lives. That is why when developing new techniques, one must appreciate the weight and responsibility carried by pathologists. Finally, medicine as a larger establishment depends on training programs and resources that are variable, based on the location of medical centers. It is not surprising that introducing new technological advances into medicine and in this case the pathology practice can face pushback. Nevertheless,the logistical challenges of introducing new approaches should not deter us from striving to provide the best patient care and evolving in response to new technology.

To explore and expand my understanding of the issues described above, I studied three challenging systems to develop a tailored approach suitable for extracting diagnostic information: brain, breast, and bone. Each of these biological systems has their unique challenges

that will be further described in subsequent chapters. In the remainder of this chapter, I will provide an overview of the imaging modalities chosen in my experiments.

1.3 Biomedical Imaging

Many scientific and engineering advancements in the last century revolutionized the way we are able to study disease processes. The application of atomic and molecular physics brought computed tomography (CT) and magnetic resonance imaging (MRI). The invention of the laser in the 1960s and subsequently spectroscopic methods enabled the interrogation of biochemical processes in biological systems. Development of the optical microscope brought a deeper understanding to tissue structure.

As new methods for tissue imaging expanded in their capability so did our understanding of their advantages and drawbacks. Many conventional methods as mentioned in the previous section involve tissue processing (freezing, formalin fixing and paraffin embedding), sectioning, and staining. Once the tissue is prepared, light microscopy is the workhorse of conventional imaging. Inherent to this process is the disruption of a biological system and the subsequent artefacts produced are a real and accepted challenge for most conventional methods.

Fluorescence-based imaging is a valuable method enabling researcher to study systems without the need for sectioning. The ability to specifically label molecules and structures of interest enables researches to explore biological structure as well as function in fixed or living specimens. The development of superresolution fluorescence microscopy permitted nanometer scale in vivo imaging of biological systems [1, 2].

Although fluorescence based approaches remain an important tool in biomedical imaging, it is worth noting that the labeling approach has limitations including potential perturbation of biological molecules or structure, limited capacity of labels, challenges with label delivery to a target, and potential toxicity.

Label-free approaches emerged to address issues with fluorescence-based imaging with

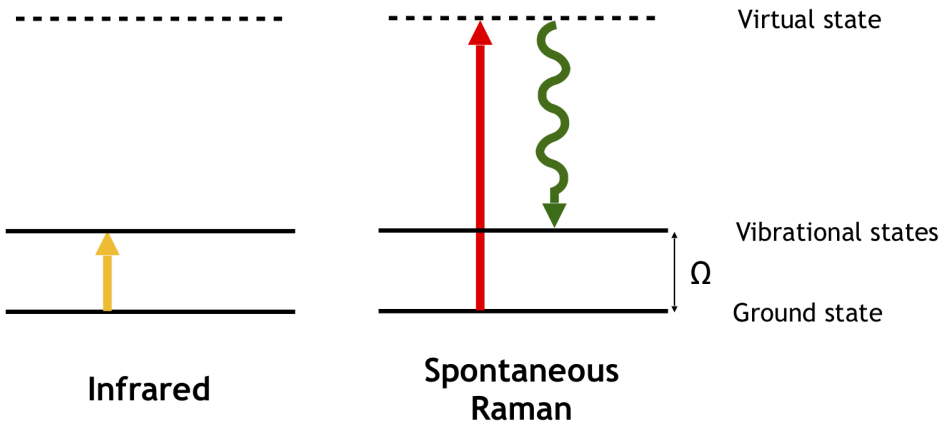

Figure 1.1: Jablonski diagram for infrared and spontaneous Raman spectroscopies.

vibrational spectroscopic imaging leading the way. Utilizing molecular "fingerprints" produced by the vibration of chemical bonds, this spectroscopic approach can provide a wealth of chemical information to shed light on the composition of tissue and chemical dynamics. Fingerprint vibration spectra can be obtained using linear IR absorption or inelastic Raman scattering (see Figure 1.1 for energy diagram). Through many technical advances, we are now able to move beyond spectroscopy to spectroscopic imaging enabling more targeted spectral tissue interrogation. IR [3] and Raman [4] spectroscopy have been utilized in a range of biomedical applications. However, the small cross section of spontaneous Raman scattering demands longer imaging time which not only runs the risk of sample damage but also makes capturing dynamic processes effectively impossible. Coherent Raman Scattering (CRS) microscopy can overcome such limitations by providing orders of magnitude enhancement to signal.

When choosing a method for imaging, it is useful to consider the inherent advantages and drawbacks of different imaging techniques. Complex biological systems can warrant more than one tool to adequately study the process of interest. This has become apparent in the research presented here, which is why the multimodal approach is used.

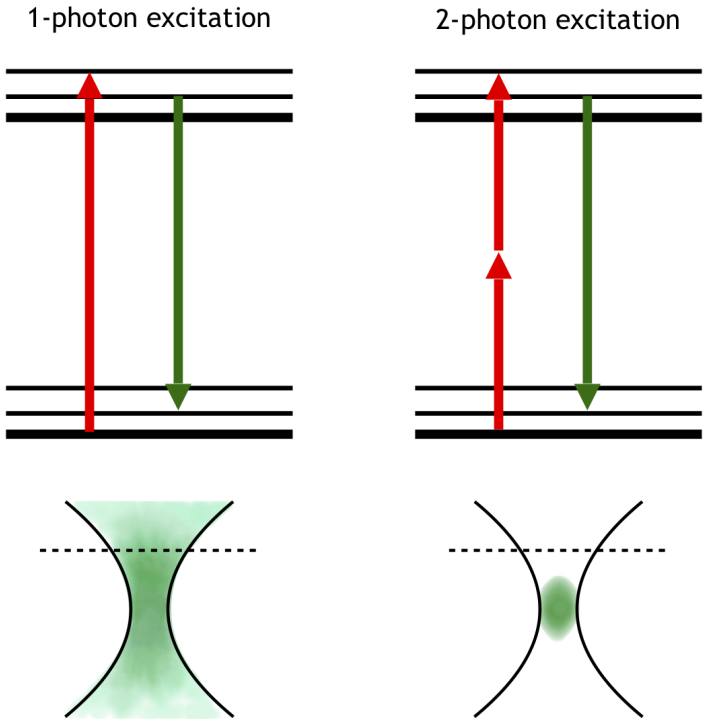

Figure 1.2: Comparison of one-photon fluorescence and two-photon fluorescence.

1.4 Multiphoton Fluorescence Microscopy

Multiphoton fluorescence microscopy is a nonlinear optical imaging technique that has been fundamental to evolving biomedical imaging. It is particularly important for imaging bulk tissue where scattering outside of the focus contributes to background as it happens in one-photon fluorescence. Instead, the nonlinearity of fluorescence excitation in multiphoton fluorescence results in signal generated only at the focus of the laser beam. This enables 3D optical sectioning in tissue. Furthermore, the multiphoton excitation at near IR wavelengths causes less photodamage making it suitable for biological systems and allowing for improved penetration depth ($\sim$ 1 mm) [5, 6, 7, 8].

Two-photon fluorescence (TPF) is the most developed among multiphoton microscopies.

Many different fluorophores have been shown to be suitable for TPF [6, 9, 10, 11, 12, 13]. In addition to fluorophores, two-photon induced autofluorescence originates mainly from endogenous fluorophores and protein structures including but not limited to NADH, collagen, porphyrins, melanin, and flavins. Typically, autofluorescence is much weaker than that from exogenous fluorophores introduced experimentally. With or without contrast agents, two-photon fluorescence is widespread in clinical applications with great advantages displayed in in vivo imaging. In this body of work, I use acridine orange (AO) to highlight nuclear features in bone.

1.5 Stimulated Raman Scattering Microscopy

1.5.1 Coherent Raman Scattering Microscopy

Vibrational spectroscopy based methods do not require contrast agents to visualize tissue. Using inherent chemical signatures, one can gain insight into biological structure in a system of interest. Using coherent vibrational processes, we can enhance signal by orders of magnitude. As a result, we can rapidly interrogate tissue without excessive laser power and reduce the risk of tissue damage.

When designing the imaging system employing CRS, it is important to understand the processes that occur when a sample encounters input photons. There are four main CRS processes that occur simultaneously when the beating frequency (ω_p - ω_s) between pump (ω_p) and Stokes (ω_s) matches the molecular vibration. One such process is coherent anti-Stokes Raman Scattering (CARS), occurring at a frequency of (ω_p - ω_s) + ω_p. Another process occurs at ω_s - (ω_p - ω_s) and is called coherent Stokes Raman scattering. Finally, there is stimulated Raman scattering (SRS) with stimulated Raman loss (SRL) at ω_p and stimulated Raman gain (SRG) at ω_s. A comparison between CARS and SRS can be found in Figure 1.3.

CARS as a third order non-linear process was first documented in 1965 by Terhune and Maker at the Ford Motor Company [14]. Since then, many advances were made to enable

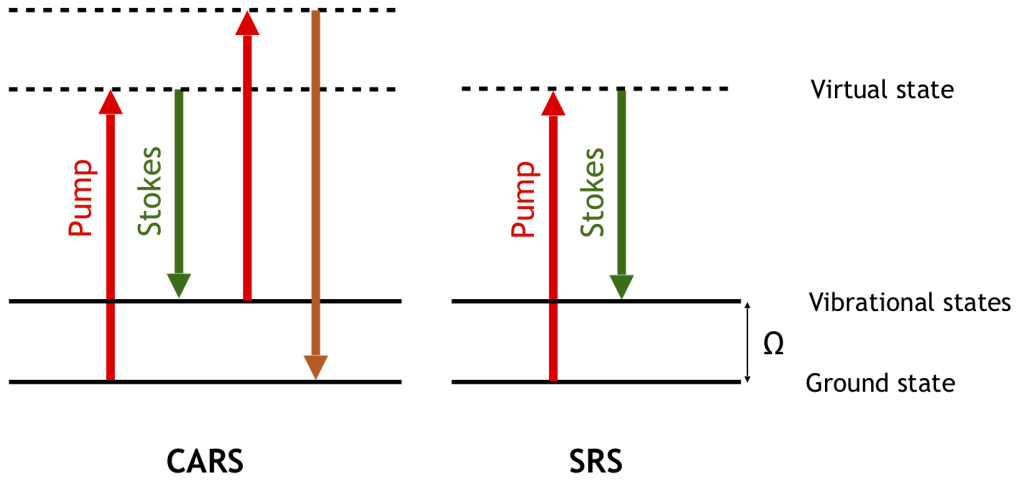

Figure 1.3: Jablonski diagram for coherent anti-Stokes Raman Scattering (CARS) and stimulated Raman scattering (SRS)

biomedical applications [15]. For CARS, the signal is generated at a new frequency different from input beams and is accompanied by a non-resonant background due to electronic contributions to four-wave mixing. The limitations of CARS include image artefacts due to spatial interference, spectral distortions due to spectral interference, and non-linear dependence of the signal on the target species concentration [16]. Despite many attempts to improve CARS microscopy, the technique still receives criticism from the biomedical imaging community along with recognition of the main successful application of CARS, lipid imaging.

As mentioned previously, CARS is not the only process occurring when conditions are met for CRS. Investigations of stimulated Raman scattering reveal that SRS microscopy is capable of overcoming the limitations posed by CARS microscopy. Superseding CARS, SRS enabled qualitative and quantitative chemical imaging with a broad range of applications to biological systems.

1.5.2 Stimulated Raman Scattering Microscopy

SRS arises under the same conditions as CARS, and either SRL or SRG can be detected. Because the excitation is stimulated, the molecular transition rate is enhanced as the difference of the excitation beams $\Delta\ \omega_p = \omega_p$ - ω_s matches the vibration frequency of the molecular transition. This enhancement is a major improvement relative to the signal strength from spontaneous Raman scattering where the transition to the vibrationally excited state is spontaneous.

The coherent excitation of the molecular vibration results from an absorbed pump photon and a generated Stokes photon. Figure 1.4 shows a summary of the principle behind stimulated Raman scattering. On the left, the energy diagram underlines that the vibrational state of interest can be probed by tuning the difference between pump and Stokes beams. The combination of pump and Stokes beams facilitates the excitation of the molecules in the sample from ground to the first vibrationally excited state via a virtual state. Because SRS is an energy transfer process, a pump photon is absorbed and a Stokes photon is generated resulting in the SRS process. Specifically, SRL of the transmitted pump and SRG of the Stokes beams are observed.

The intensity change of the transmitted pump and Stokes beams are directly proportional to the number of molecules (N) in the focal volume and the molecular Raman scattering cross-section(σ) as reflected in the following expression [17]

$$\Delta I_s \propto N \cdot \sigma \cdot I_p \cdot I_s \tag{1.1}$$

$$\Delta I_p \propto -N \cdot \sigma \cdot I_p \cdot I_s \tag{1.2}$$

Provided that the change in intensity is calibrated against the number of molecules in the focal volume or concentration of chemicals of the target species, a quantitative chemical map of the sample can be obtained. Additionally, non-linear dependence of the signal on the excitation intensities enables optical sectioning [18], which is crucial when imaging thick tissue samples [8].

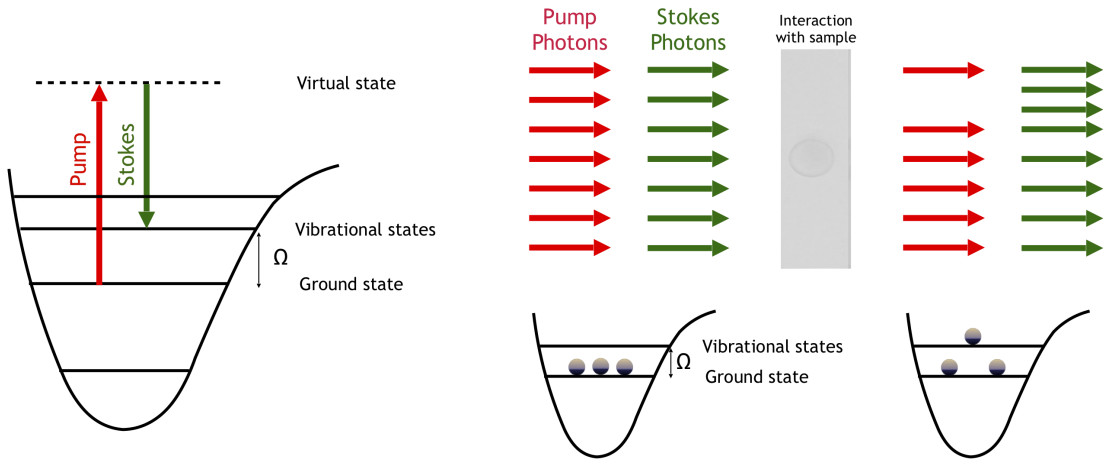

Figure 1.4: Principle behind stimulated Raman scattering. The vibrational state can be selected by tuning the difference frequency between pump and Stokes beams. SRS is a energy transfer process. A pump photon is absorbed, and a Stokes photon is generated.

Because the change in intensity is very small ($\Delta\ I_p/I_p < 10^{-4}$), a high frequency phase-sensitive detection is needed. In this work, the Stokes beam is modulated, resulting in modulation transfer to the unmodulated pump beam at the same frequency. The Stokes beam is filtered at the detection.

Consideration has to be given to the frequency of modulation. By using high frequency, higher than 1 MHz, laser noise that occurs primarily at low frequencies of thermal and mechanical fluctuations is avoided.

In a typical SRS microscopy setup, only a limited wavelength range can be scanned without time-consuming adjustments. To address this issue, "spectral focusing" can be employed [19, 20]. By sending the femtosecond laser pulses through a dispersive medium, the linear chirp is introduced through the temporal spreading of the frequency components. This leads to narrower instantaneous bandwidth. By simply varying temporal delay between the two chirped pulses, different vibrational frequencies can be accessed.

Finally, when applying SRS to thicker samples, an important limitation has to be kept in mind. Typically, SRS is performed in transmission. Efficient collection of back-scattered

signal (epi-detection) can be achieved in media where scattering dominates over absorption [21]. In the research presented here, epi-detection is utilized for bone imaging. Bony samples are dense and scatter well to allow sufficient signal collection.

1.6 SHG Microscopy

In addition to SRS and TPF, second harmonic generation (SHG) microscopy has been demonstrated to be an important tool in disease diagnosis [22]. SHG is a second order coherent process. In such process, two lower energy photons are up-converted to twice the incident frequency of the excitation beam. The very first SHG imaging applied to biological system was reported in 1986 by Freund who studied collagen fibers in a rat tail tendon [23]. Later in 2002, a practical implementation of tissue imaging was conducted by Mohler and Campagnola. Implementing high resolution and rapid data acquisition with laser scanning, Mohler and Campagnola have established SHG microscopy as a powerful imaging tool. As a result, many applications have been demonstrated in cancer, fibrosis, connective tissue disorders, atherosclerosis, among others [22].

Briefly, SHG is described by the second term of the total polarization equation for a material interacting with light and can be expressed as the following

$$P = X^{(1)}E^1 + X^{(2)}E^2 + X^{(3)}E^3 + ... \tag{1.3}$$

where P is the induced polarization, $X^{(n)}$ is the nth order nonlinear susceptibility tensor and E is the electric field vector [24]. In comparison, the third term describes SRS and CARS. Because SHG is a second-order process, the second-order symmetry imposes restrictions on what harmonophores can be imaged, and shows the signal for noncentrosymmetric systems (size scale of λ_{SHG}). Additionally, the molecular and bulk properties can be related by the following expression.

$$X^{(2)} = N_s < \beta > \tag{1.4}$$

where N_s is the density of molecules, β first hyperpolarizability, and brackets denote the orientational average.

The experimental implementation of SHG microscopy can include forward and backward SHG detection depending on the application. Using an appropriate dichroic mirror and filters before the photo multiplier tube (PMT), SHG can be easily integrated with other non-linear microscopies. In the work described in this dissertation, SHG will play an important role in breast and bone systems.

1.7 Summary

The current challenges faced by anatomic pathologists influence clinicians' ability to choose an appropriate treatment and ultimately impacts the patient. Therefore, an investigation of methods that can enhance current diagnostic capability as well as offer new perspective into disease processes by offering novel information is beneficial. Understanding this motivates the work in this dissertation.

Biomedical imaging as a field has evolved and offered many tools, some of which are being developed right now for pathology applications. To facilitate a sustainable introduction and implementation of novel analysis tools requires close collaboration of biomedical imaging scientists with pathologists introducing opportunities for interdisciplinary training. It is my hope that this volume of work is a first step in this direction.

Chapter 2

INTRAOPERATIVE ASSESSMENT OF SKULL BASE TUMORS USING STIMULATED RAMAN SCATTERING MICROSCOPY

2.1 Preface

Shortly before I joined the Fu lab, a project relating to the intraoperative assessment of skull base tumors was started by Dr. Dan Fu and Andrew Francis in collaboration with Dr. Gordana Juric-Sekhar and Dr. Laligam Sekhar. After the application to receive funding was successful, the tissue collection was initiated. The initial tissue imaging was first conducted by Andrew Francis and later was continued by me. This was also the time when Andrew Francis contributed significantly to my training in optics. As I became more involved the project slowly transition to me, and I became the primary graduate researcher responsible for its completion.

One of the many challenges was developing a recoloring routine to produce images suitable for pathology diagnosis. I had to rely on much of the pathology knowledge imparted on me by my Post Sophomore Fellowship in pathology which I completed before resuming my graduate studies. The project was truly interdisciplinary and relied on very close collaborations between tech developing scientists, pathologists, and surgeons. Designing the evaluation approach was done in collaboration with Dr. Gordana Juric-Sekhar and myself. A crucial part of the project was also an evaluation of resulting images by the pathologists. Drs. Patrick Cimino, Caitlin Latimer, and Louis Gonzalez-Cuyar provided the needed feedback and evaluation.

Kseniya S. Shin; Andrew T. Francis; Andrew H. Hill; Mint Laohajaratsang; Patrick J. Cimino; Caitlin S. Latimer; Luis F. Gonzalez-Cuyar; Laligam N. Sekhar; Gordana Juric-Sekhar; and Dan Fu; "Intraoperative assessment of skull base tumors using stimulated Raman scattering microscopy," *Scientific Reports* **9**, 20392 (2019).

2.2 Abstract

Intraoperative consultations, used to guide tumor resection, can present histopathological findings that are challenging to interpret due to artefacts from tissue cryosectioning and conventional staining. Stimulated Raman histology (SRH), a label-free imaging technique for unprocessed biospecimens, has demonstrated promise in a limited subset of tumors. Here, we target unexplored skull base tumors using a fast simultaneous two-channel stimulated Raman scattering (SRS) imaging technique and a new pseudo-hematoxylin and eosin (H&E) recoloring methodology. To quantitatively evaluate the efficacy of our approach, we use modularized assessment of diagnostic accuracy beyond cancer/non-cancer determination and neuropathologist confidence for SRH images contrasted to H&E-stained frozen and formalin-fixed paraffin-embedded (FFPE) tissue sections. Our results reveal that SRH is effective for establishing a diagnosis using fresh tissue in most cases with 87% accuracy relative to H&E-stained FFPE sections. Further analysis of discrepant case interpretation suggests that pseudo-H&E recoloring underutilizes the rich chemical information offered by SRS imaging, and an improved diagnosis can be achieved if full SRS information is used. In summary, our findings show that pseudo-H&E recolored SRS images in combination with lipid and protein chemical information can maximize the use of SRS during intraoperative pathologic consultation with implications for tissue preservation and augmented diagnostic utility.

2.3 Introduction

The overarching purpose of intraoperative consultations for tumor surgeries is to obtain crucial information that informs surgical treatment. The tools currently employed include microscopic assessment of a submitted specimen through cytological preparations or cryosectioning and subsequent staining of the tissue by hematoxylin and eosin (H&E). The challenges of generating a diagnostically adequate H&E slide of cryosectioned tissue are organ-specific. In central nervous system specimens, the main challenge often results from limited sample size and general texture heterogeneity of the submitted tissue. In such cases, texture heterogeneity manifests itself as a freeze artefact - the diffuse or focal splitting of sections or cellular rarefaction resulting in loss of diagnostic information [25]. The presence of these artefacts in microscopic sections can result in misinterpretations and subsequent diagnostic pitfalls [26].

In addition to the inherent challenges of cryosectioning, the location of the tumor can add complexity to management. One group of tumors that poses many challenges is skull base tumors which include meningiomas, pituitary adenomas, schwannomas, hemangiopericytomas, chordomas, various types of sarcomas, carcinomas, and metastases among other entities [27]. Skull base tumors face unique challenges due to their low occurrence, presence in deep locations, proximity to critical neurovascular structures, and extension beyond anatomic boundaries [28]. Accurate intraoperative tissue diagnosis is essential during skull base tumor surgery to maximize tumor removal, as a non-resected tumor can lead to recurrence, treatment failure, and overall poor outcome [29]. In particular, a rapid diagnosis during the removal of skull base tumors can help the surgeon to choose how aggressive the resection should be. In addition, in some patients, a rapid diagnosis can help to delineate the margins of tumor resection. Additionally, there is an increasing need to preserve tissue from small pathology specimens for downstream molecular ancillary testing, and an intraoperative technique aimed at preserving tissue would be preferable in these cases.

Many advanced optical imaging techniques have been developed to detect neoplastic cells

and to provide diagnostic information with varying degrees of success, including optical coherence tomography [30, 31], confocal microscopy [32], two-photon fluorescence combined with second harmonic generation [33, 34, 35], Raman spectroscopy [36], and coherent Raman scattering (CRS) microscopy [37]. Among the previous work, CRS stands out from other imaging techniques as it provides both morphological and chemical information at a submicron resolution without any staining or chemical labels [38]. Two CRS methods have been established: coherent anti-Stokes Raman scattering (CARS) and stimulated Raman scattering (SRS). Both CARS and SRS use two pulse lasers (pump and Stokes) to excite intrinsic vibrational motions of molecules coherently and have been shown to be able to provide molecular contrasts that can aid cancer diagnosis [37].

In particular, it was recently demonstrated that SRS microscopy could provide H&E equivalent information for pathologists to determine cancer subtypes, thereby offering the potential for replacing frozen sectioning as an intraoperative diagnostic tool [39, 40]. Specifically, it has been shown that a two-color SRS imaging approach targeting the C-H transition of lipid and protein (Raman transition at 2850 cm^{-1} and 2930 cm^{-1}, respectively) allow direct visualization of cell nuclei. The resulting images can be recolored using linear dependence of the signal on lipid and protein content, allowing for a simple and very close simulation of H&E, i.e., stimulated Raman histology (SRH). Orringer et al. and Hollon et al. have tested the efficacy of SRS microscopy as a potential intraoperative H&E staining alternative for cases including glial and metastatic neoplasms with 92 % accuracy of tumor subtype determination as assessed by neuropathologists [39, 40]. Another recent study using the same SRH approach further validated the visual comparison of SRH images to H&E as applied to gastrointestinal tract [41]. Other studies used two-color SRS images for cancer/non-cancer identification in laryngeal squamous cell carcinoma [42] and glioblastoma infiltration in the brain [43]. However, these studies did not provide pathologist evaluation of SRH or SRS two-color images for cancer subtype determination and thus are insufficient to validate SRS as an alternative to histology. Similar to SRS, CARS microscopy has also been explored for cancer diagnosis [44, 45, 46] based on chemical contrasts. Compared to SRH, CARS is

further complicated by the presence of a non-resonant background [47, 48, 49, 50], which prevents direct conversion of CARS images to H&E images. Adding additional chemical contrasts from second harmonic generation and two-photon fluorescence, it has been shown that multicolor images can be generated and provides useful diagnostic information [51]. However, whether pathologists can use these images to provide meaningful cancer diagnosis requires further investigation.

While a few studies have validated SRH in limited settings, it remains unclear whether SRH is generally applicable to a diverse set of tumor types encountered in daily pathology practice. Employing two Raman transitions targeting lipids and proteins to generate an H&E alternative works well for entities with higher cytoplasmic lipid content as can be expected in glial neoplasms. This is because the cytoplasmic lipid signals are a primary source of contrast to visualize cell nuclei. However, skull base tumors are inherently more complex because high protein and low lipid concentrations in the cytoplasm or the stromal matrix are common and can pose a challenge in visualizing nuclei. To explore the utility and limitations of SRH in complex tumors, we have set out to conduct a more dedicated investigation of SRH application to skull base tumors. Additionally, we take a different approach from previous studies by focusing on the user (i.e., pathologist) in addition to SRH validation. With only a few publications testing the accuracy of diagnosing histological subtypes [39, 40], we emphasize assessment of how SRH performs at every step of the typical diagnostic workflow. Moreover, unlike previous studies, instead of training pathologists with SRH images, diagnosis in this study is performed without prior training and thus provides an unbiased assessment of the diagnostic accuracy achievable in an intraoperative setting.

We used a simultaneous two-channel SRS imaging method we and others have developed to enable rapid SRH assessment [52, 53]. Specifically, we performed simultaneous two-channel acquisition by using two 90° phase shifted Stokes pulses for orthogonal lock-in detection. This approach allows us to acquire protein and lipid SRS images rapidly for large pieces of tissue by eliminating wavelength switching and sequential acquisition. We image fresh resected tumor tissue collected prospectively during intraoperative consultation and validate the di-

agnostic capability of SRH through modularized review by board-certified neuropathologists. Our results reveal that SRH is effective in most cases with 87% accuracy relative to H&E stained formalin-fixed paraffin-embedded (FFPE) sections. Moreover, we find that in cases with limited lipid signal to provide the necessary contrast for nuclei visualization, rendering diagnosis is challenging when using strictly SRH, and it can be significantly improved with SRS chemical information.

2.4 Experimental Methods

2.4.1 Tissue collection and preparation

Sixteen subjects undergoing operations for skull base tumors were recruited with the approval of the University of Washington Institutional Review Board over the course of 12 months, and all research was performed in accordance with relevant guidelines and regulations. Subject eligibility was determined during preoperative evaluation by the neurosurgeon (L.N.S.) participating in this study, and written informed consent was obtained from each subject before surgery. At the time of standard intraoperative frozen section consultation, a fresh tissue sample measuring 0.3 x 0.2 x 0.1 cm on average was allocated for this study. Each piece of fresh and unlabeled tumor sample was placed on a well depression glass slide, moistened with saline and covered with a coverslip in preparation for SRS imaging. Following SRS imaging, each sample was placed in neutrally buffered formalin, processed, and embedded in paraffin for permanent sections. Samples were then sectioned and stained with H&E for standard histopathological analysis. All SRS images with corresponding FFPE sections stained with H&E of skull base tumors were reviewed by a board-certified neuropathologist (G.J-S.), who selected representative portions of SRS images for histological analysis. Slides of frozen sections or cytological preparations performed at the time of intraoperative consultation from all studied cases were also reviewed in this study in order to compare the quality of SRS images with standard intraoperative techniques and to determine the diagnostic utility of SRS microscopy.

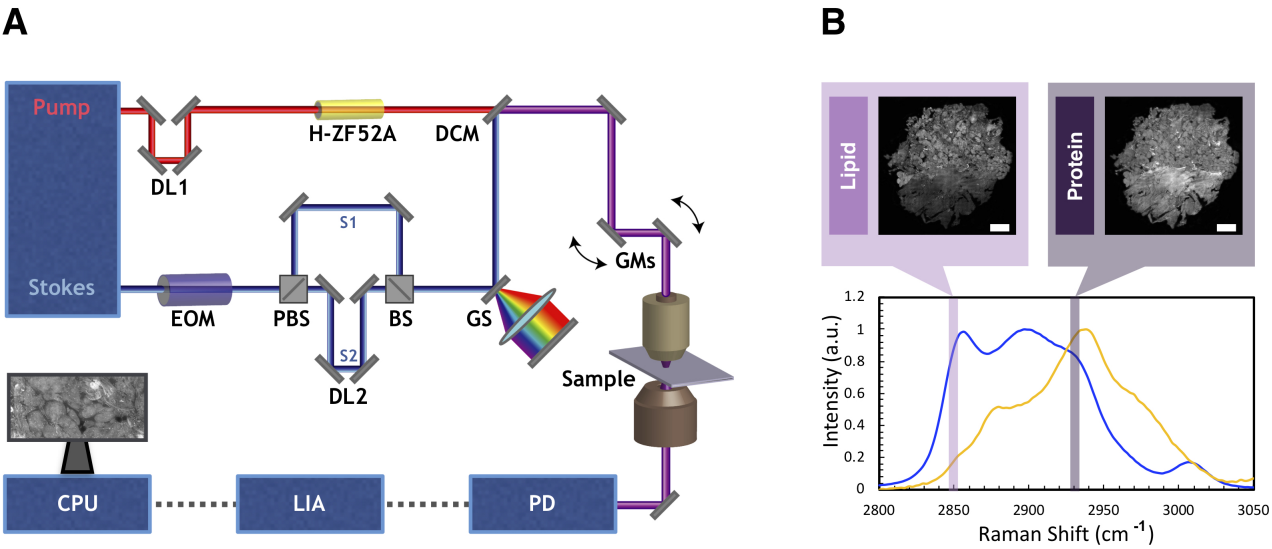

Figure 2.1: Experimental set up for SRS microscope and controls for lipid and protein channels. A) The Stokes laser is modulated by an electro-optical modulator (EOM) at 20 MHz. Tunable laser is spectrally dispersed through glass rods (tunable) and Stokes laser is dispersed through a grating stretcher (GS). They are the spatially and temporally overlapped at a dichroic mirror (DCM) and directed onto a pair of galvanomirrors (GM). The beams are then sent through a laser scanning microscope with a 25x water immersion objective. The pump beam after the condenser is detected by a photodiode (PD). The signal is processed through lock-in amplifier (LIA). The images are collected using ScanImage on computer processing unit (CPU). B) SRS spectra for oleic acid and bovine serum albumin (BSA) as controls for lipids and proteins, respectively.

2.4.2 SRS microscopy

Figure 2.1 A depicts simultaneous two-color SRS that was employed in our study [52, 53]. Briefly, the Stokes and pump pulses provided by the fixed (1040 nm center wavelength, <200 fs, >1.5 W) and tunable (798 nm center wavelength, <150 fs, 1.0 W) outputs, respectively, of a dual-output oscillator (Insight DS+, SpectraPhysics) with a repetition rate of 80 MHz. The Stokes pulse was modulated at 20 MHz using an electro-optic modulator (EOM) and split into two separate arms, one of which was then delayed by 12.5 ns (1/80 MHz) relative to the other. The two arms were recombined using a 50:50 beamsplitter and stretched to 2 ps using a grating-based pulse stretcher [54, 55]. The tunable source was centered at 798

nm, and the pulses were dispersed using 60 cm of glass rods. The average spectral width is estimated to be 300 cm^{-1} [55]. The pump and Stokes beams were then combined with a dichroic mirror and overlapped temporally using a delay line in the tunable arm. The resulting beam was sent into a home-built laser scanning microscope. A 25X Olympus water immersion objective (NA = 1.05) was used to focus the beams onto the tissue sample. At the focus, the Stokes beams had an average power of 30 mW each, and the pump had an average power of 40 mW. After passing through the condenser, the Stokes beam was filtered out, and the pump reached a silicon photodiode. SRS signal was detected with a lock-in amplifier. The two orthogonal output of the lock-in amplifier provided the simultaneous two-channel SRS signals for pseudo H&E rendering [52]. Figure 2.1 B depicts examples of SRS spectra for oleic acid and bovine serum albumin (BSA) as controls for lipids and proteins respectively.

2.4.3 Image processing

Figure 2.2 details how SRS images were processed into the pseudo-H&E images to be given to neuropathologists for analysis. The acquired lipid (Figure 2.2A) and protein (Figure 2.2B) images (285 μm x 285 μm per frame) were field-normalized and stitched to recover a complete tissue image (2-6 mm in size). Subsequently, the lipid channel was subtracted from protein channel, as previously demonstrated, to generate lipid corrected protein image (Figure 2.2C) [56]. Using a custom-generated color scale in Image J, the lipid and lipid-corrected protein channels were recolored to match the conventional H&E (Figures 2.2D and 2.2E) and combined to form a single image for histological analysis by pathologists (Figure 2.2F).

2.4.4 Survey methodology

A validation survey was conducted in order to establish the diagnostic utility of SRS simulated H&E images (SRH) compared to standard intraoperative pathology, which typically

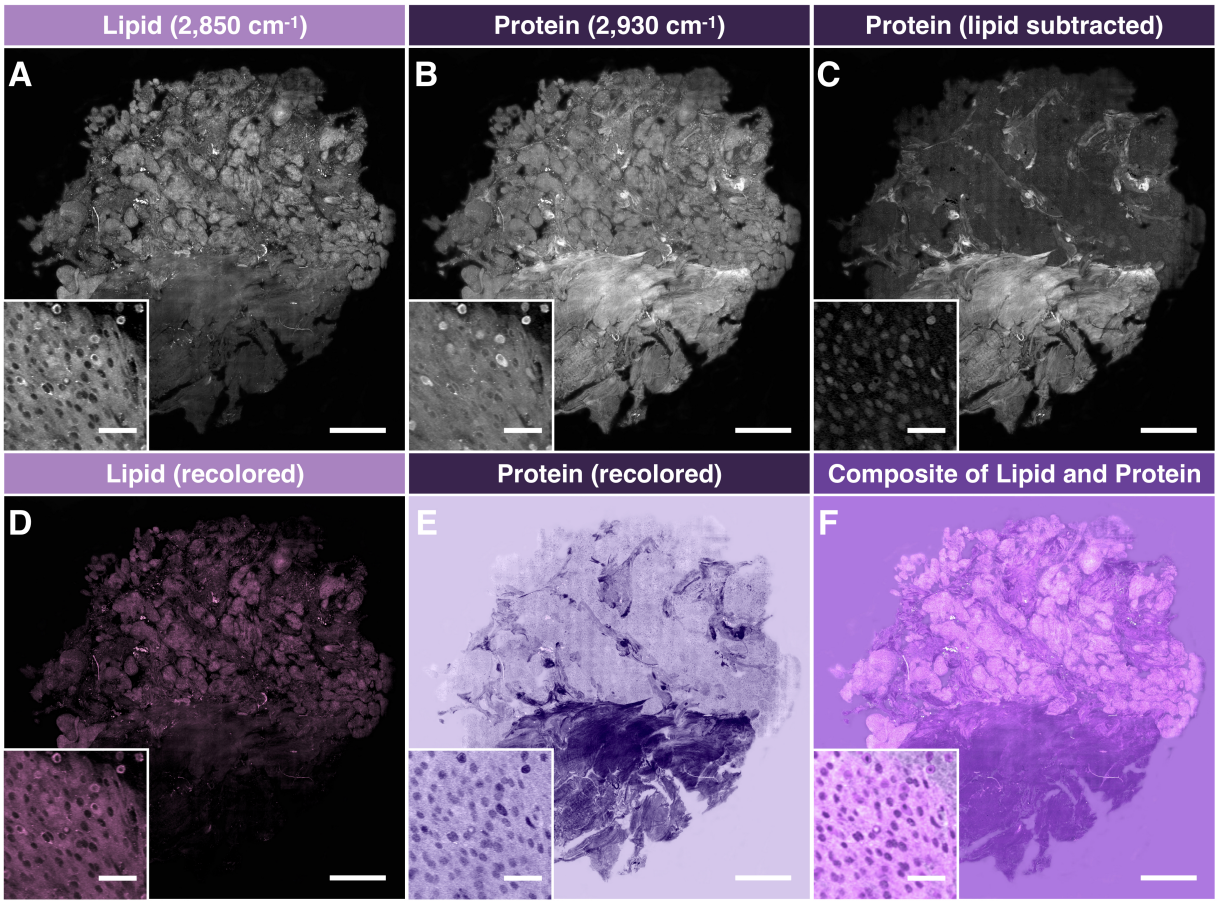

Figure 2.2: Image processing of stitched SRS imaging data (Meningioma, WHO grade I). A) Stitched field-normalized data for lipid channel. B) Stitched field-normalized data for protein channel. C) Lipid data subtracted from protein, utilizing lipid and protein images in A and B. D) Recoloring result of lipid data. E) Recoloring result of protein data. F) Composite image of D and E. Whole tissue scale bar: 1 mm. Inset scale bar: 50 μm.

includes the frozen section and cytological preparation of the specimen routinely stained with H&E. The survey was performed by three neuropathologists (P.J.C., C.S.L., and L.F.G.-C.) who were blind to the diagnosis. They received a short clinical and radiographic summary of each case to mimic the circumstance of an intraoperative consultation but had no knowledge of SRS imaging and no training on SRH images. All sixteen studied cases were enrolled in the survey, which consisted of three phases: 1. Review of SRS generated images (SRH); 2. Review of the H&E-stained FFPE sections of the same specimen, and; 3. Review of the H&E-stained frozen sections or cytological preparations performed at the time of the neoplasm extraction for intraoperative diagnosis. Each phase included a series of multiple-choice questions focused on neoplastic appearance (epitheliod, spindle cell, myxoid, chondroid, or other), architectural pattern (lobular, fascicular, glandular, nested, papillary, sheeting, or other), and nuclear shape (rounded, elongated, and other). After the initial assessment, the evaluators participated in the diagnostic interpretation of each case that included differential diagnosis (a list of neoplasms that fit the neoplasm description, architectural pattern, and nuclear shape they have assigned to the case in combination with a clinical and radiographic summary provided) and final diagnosis. Finally, each participant was required to quantify their level of confidence in their diagnosis. The results of the survey were compared to the assessment by collaborating pathologist G.J.-S. (histopathological features and differential diagnosis) and the neuropathology report (final diagnosis).

2.4.5 Statistical analysis of survey data

For each pathologist, percent agreement and Cohen's kappa (κ_C) were calculated while comparing each modality (SRH, H&E frozen, and H&E permanent) to the assessment by the collaborating pathologist G. J.-S. (histopathological features and differential diagnosis) and the neuropathology report (final diagnosis) for individual case using R software. Additionally, the relative accuracy as a ratio of SRH and H&E FFPE percent agreement was calculated for comparison of SRH to the golden standard of diagnosis. Fleiss' kappa (κ_F) was calculated

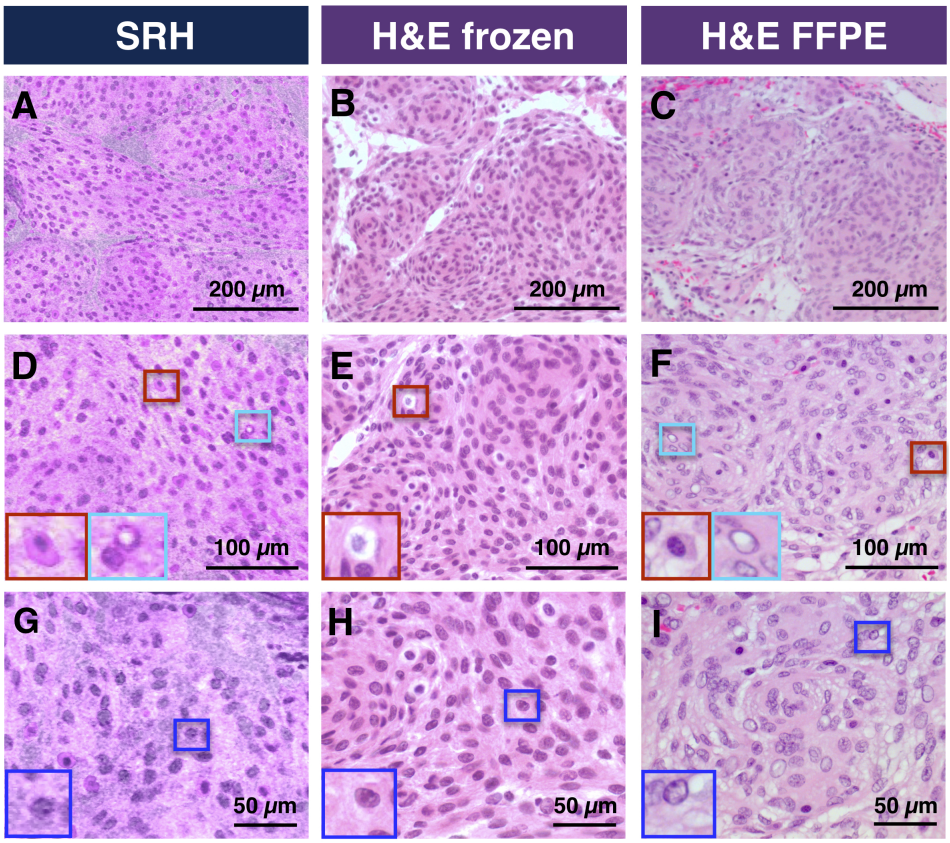

Figure 2.3: Comparison of cellular features available with SRH *versus* conventional H&E stained slides in representative case of Meningioma WHO grade I. A, B, C) Comparison of architecture features. D, E, F) Increased magnification highlighting macrophages (red box) verified by immunohistochemistry and intranuclear inclusions (cyan box). G, H, I) Nuclear features with easily identifiable nucleolus (blue box).

to assess interpathologist reliability.

2.5 SRH images provide cytoarchitectural visualization necessary for diagnosis

For a pathologist, architectural and cytological features are necessary for the diagnostic process. We use a studied meningioma case in Figure 2.3 as an example of cytoarchitectural visualization available with SRH images. The characteristic lobular architectural growth pattern of epithelioid cells is as apparent in SRS images as it would be at a lower magnification

of H&E stained frozen or FFPE sections (Figures 2.3A-2.3C). At high resolution, the SRH image shows clear cytomorphology such as round to oval nuclei with bland chromatin and inconspicuous nucleoli (Figures 2.3G-2.3I). Moreover, scattered intranuclear pseudoinclusions, common histological features identified in meningiomas, are also visualized on SRH (Figure 2.3D). Identical histological features are present in concurrent frozen and concomitant FFPE sections (Figures 2.3H and 2.3I).

Furthermore, sufficient cytomorphological features can be identified to determine other cell types. Figures 2.3D-2.3F show lipid-rich cells identified and marked by a red box as macrophages (confirmed by immunohistochemistry). While in the case of meningioma, these cells are not considered diagnostically essential, in the case of breast cancer, tumor-associated macrophages have been explored as a prognostic marker [57, 58].

2.6 SRH images reveal diagnostic features in a broad range of skull base tumors

An accurate pathologist interpretation of unique histopathological features is essential during a neurosurgical procedure. For SRH to be applicable in an intraoperative setting, SRH must deliver clear and easy to interpret images with sufficient information. To examine the capability of SRH at providing useful histopathological information, we image a broad range of skull base tumors including nine meningiomas, three schwannomas, one chordoma, one chondrosarcoma, one pituitary adenoma, and one papillary craniopharyngioma. Figure 2.4 highlights typical diagnostic features of selected skull base tumors captured by SRH in comparison with H&E stained frozen sections of the same case and H&E stained FFPE sections of the same tissue.

The advantage of SRH is the ability to image the sample without sectioning, which eliminates challenges introduced by freeze artefact from cryosectioning. This issue is exacerbated when tissue samples are challenging to cut due to the heterogeneity of texture. The three cases that serve as an example (meningioma, chordoma, and chondrosarcoma) are shown Figure 2.4. Figures 2.4A, 2.4G, and 2.4J demonstrate well-preserved diagnostic features

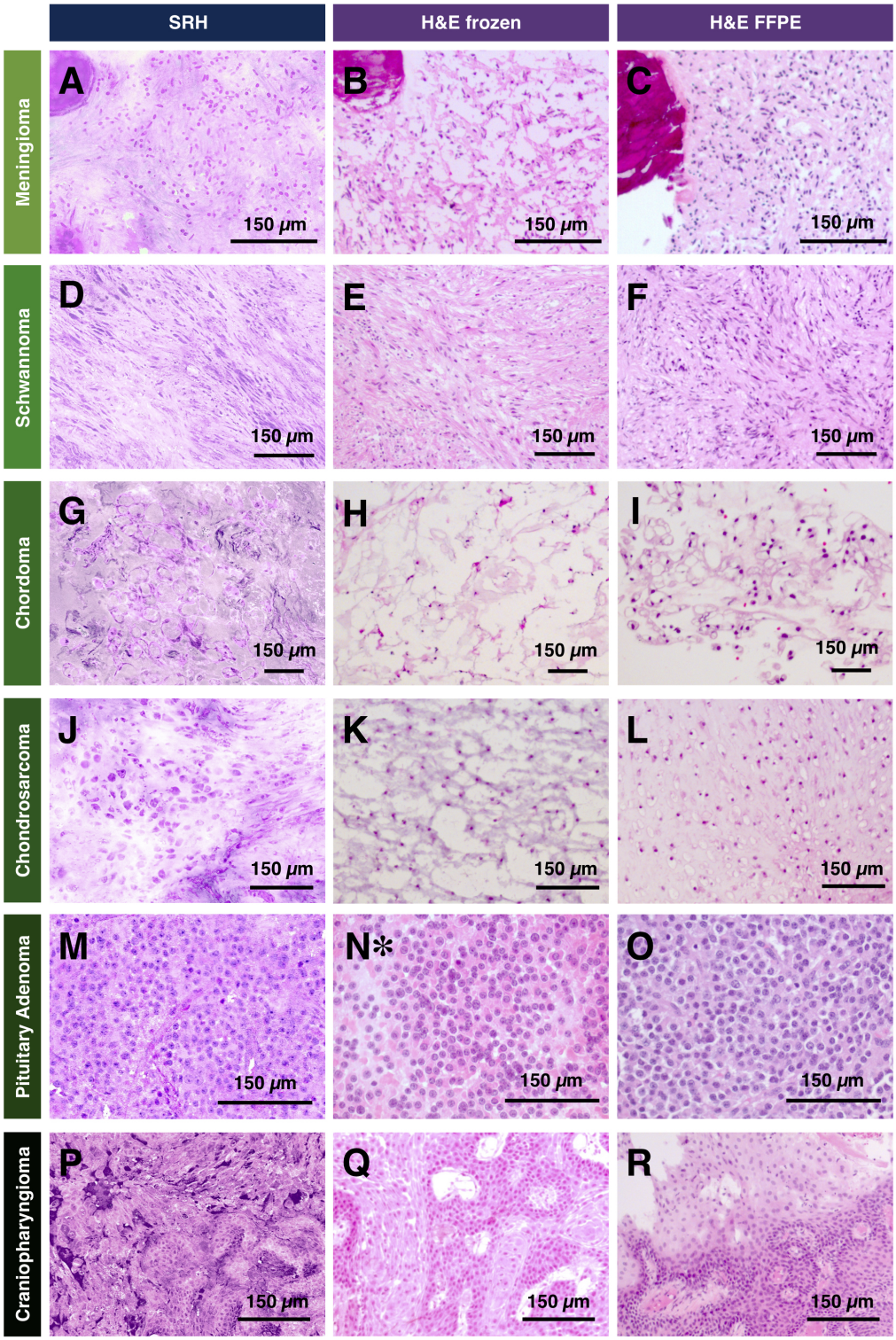

Figure 2.4: Comparison of SRH with conventional histological preparations of skull base tumors. A, B, C) Meningioma, WHO grade I. D, E, F) Schwannoma, WHO grade I. G, H, I) Chordoma. J, K, L) Chondrosarcoma, grade 2. M, N*, O) Sparsely granulated somatotroph adenoma. P, Q, R) Papillary craniopharyngioma (BRAF-mutant). *The case warranted cytological preparations only during intraoperative consultation.

in SRH images for meningioma, chordoma, and chondrosarcoma, respectively. In contrast, Figures 2.4B, 2.4H, and 2.4K show corresponding H&E stained frozen sections distorted by freeze artefact. FFPE sections providing a reference for the typical appearance of histological features are shown in Figures 2.4C, 2.4I, and 2.4L.

In the case of meningioma, the texture heterogeneity is caused by psammoma bodies (round collection of calcified material). This is a good example of the challenges faced when calcified material is present during cryosectioning. Psammoma bodies are diagnostically helpful when suspecting meningioma, which mitigates poor tissue preservation in this case specifically. On the other hand, conserving features in case of chordoma and chondrosarcoma is important for accurate identification. Figures 2.4G and 2.4I show chordoma with vague small clusters and individual epithelioid cells with pale vacuolated cytoplasm (physaliphorous cells) and prominent dense extracellular protein-rich myxoid matrix that are missing in frozen section images. Similarly, one studied chondrosarcoma (low-grade per neuropathology report) demonstrated scattered mononucleated neoplastic cells in lacunae found in an abundant cartilaginous protein-rich background (Figures 2.4J and 2.4L). These three examples highlight SRH advantage over the conventional frozen section in preventing loss of cytoarchitecture due to the extensive freeze artefact and tissue texture heterogeneity. When freeze artefacts are not a significant issue, the diagnosis on frozen section analysis can still be challenging due to ambiguous histomorphology in spindle neoplasms including schwannoma (Figures 2.4D-F) and meningioma without psammoma bodies (Figure 2.3). With SRH, the different recoloring scheme can be used to highlight those features as will be discussed later. Additionally, because SRH is non-destructive, any imaged tissue can be saved for downstream histopathological analysis, and it is a significant advantage in cases where there is limited tissue.

In other studied types of tumors, similar morphological features found typically in FFPE sections are sufficiently replicated in SRH. For example, SRH of studied pituitary adenoma reveals sheets of relatively monotonous neuroendocrine cells with a moderate amount of cytoplasm and rounded nuclei with bland and occasionally stippled chromatin, depicted

in Figure 2.4M. These histological features agree well with those observed in a concomitant H&E-stained FFPE section (Figure 2.4O) as well as concurrent cytological preparation (Figure 2.4N). Additionally, our study includes a craniopharyngioma, a squamous epithelial neoplasm characterized by cauliflower-like papillary structures and fibrovascular core, which are visible on SRH image (Figure 2.4P), FFPE (Figure 2.4R), and corresponding frozen sections stained with H&E (Figure 2.4Q).

Finally, SRH provides information on chromatin appearance, which can be used as evidence of preoperative treatment such as embolization. Preoperative endovascular embolization, adjunctive treatment of meningioma, was performed in 5 out of 9 studied meningiomas, and in one studied case resulted in noticeable cytomorphological changes captured on SRH (Figure 2.8 in Supplementary), including the vague architectural structure and neoplastic cells with pyknotic nuclei (Figure 2.4A). These histopathological features were also identified on both conventional H&E-stained FFPE sections of the same specimen and corresponding frozen sections (Figures 2.4B and 2.4C). To contrast, a meningioma case without prior embolization discussed earlier can be referenced (Figure 2.3 and Figure 2.8 in Supplementary).

Qualitative comparison of SRH images to H&E stained frozen sections shows that SRH offers an advantage over frozen section by avoiding diagnostic pitfalls due to freeze artefact. The pseudo-H&E recolored SRS images offer comparable diagnostic features that are available in H&E stained FFPE with the advantage of being non-destructive and preserving tissue for downstream diagnostic tests.

2.7 Diagnostic accuracy of SRH images compared to conventional H&E based techniques

In order to establish the diagnostic utility of SRH, we administer a survey which assesses the interaction of a given neuropathologist with SRH, H&E stained frozen, and FFPE section slides. Unlike previous studies [39, 40], our survey included modularized assessment of the pathologist experience with SRH testing beyond final diagnostic accuracy. Typically, a pathologist uses histopathological features including neoplasm description, architectural

	Neuropathologist 1			Neuropathologist 2			Neuropathologist 3			Interpathologist reliability (κ_F)		
	SRH	H&E frozen	H&E FFPE	SRH	H&E frozen	H&E FFPE	SRH	H&E frozen	H&E FFPE	SRH	H&E frozen	H&E FFPE
Neoplasm Description:												
Percent Agreement	88%	88%	88%	75%	88%	81%	75%	75%	75%			
Concordance (κ_c)	0.78	0.80	0.80	0.52	0.78	0.66	0.61	0.56	0.59	0.48	0.78	0.63
Relative Accuracy	**100%**	-	-	**92%**	-	-	**100%**	-	-			
Architectural Pattern:												
Percent Agreement	75%	75%	75%	69%	88%	81%	44%	56%	50%			
Concordance (κ_c)	0.64	0.65	0.65	0.58	0.83	0.74	0.34	0.48	0.43	0.28	0.38	0.41
Relative Accuracy	**100%**	-	-	**85%**	-	-	**88%**	-	-			
Nuclear Shape:												
Percent Agreement	94%	100%	94%	94%	94%	94%	88%	94%	94%			
Concordance (κ_c)	0.87	1.00	0.86	0.86	0.86	0.86	0.73	0.86	0.86	0.64	0.91	0.82
Relative Accuracy	**100%**	-	-	**100%**	-	-	**93%**	-	-			
Differential:												
Percent Agreement	94%	100%	100%	94%	100%	100%	94%	100%	100%			
Concordance (κ_c)	0.90	1.00	1.00	0.90	1.00	1.00	0.90	1.00	1.00	-	-	-
Relative Accuracy	**94%**	-	-	**94%**	-	-	**94%**	-	-			
Final Diagnosis:												
Percent Agreement	88%	94%	100%	75%	94%	81%	81%	100%	94%			
Concordance (κ_c)	0.80	0.90	1.00	0.61	0.90	0.68	0.66	1.00	0.90	0.57	0.87	0.79
Relative Accuracy	**88%**	-	-	**85%**	-	-	**87%**	-	-			
Confidence score	***3.13***	***3.50***	***3.50***	***2.31***	***2.81***	***3.31***	***2.94***	***3.63***	***3.56***			

Table 2.1: Survey results, comparing SRH *versus* conventional tissue processing and staining. Relative accuracy is calculated as ratio of SRH percent agreement and H&E FFPE. Confidence score is assigned as follows: 4 - highly confident, 3 - confident, 2 - somewhat confident, 1 - not at all confident.

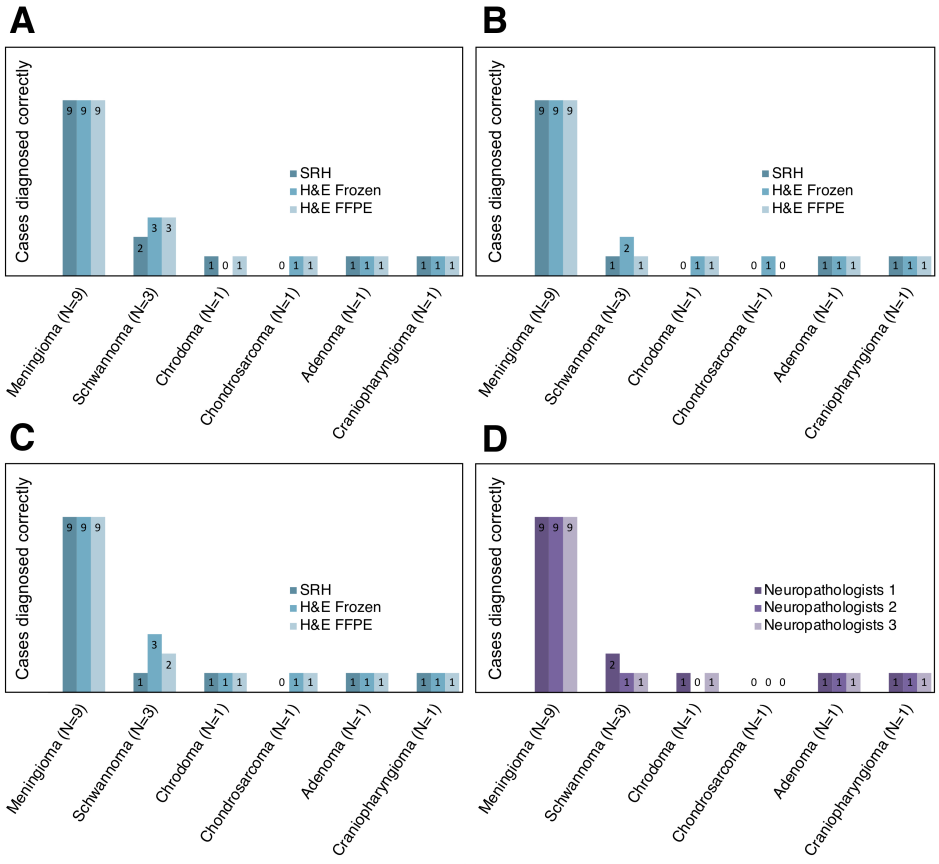

Figure 2.5: Depiction of correctly diagnosed cases for each neuropathologist and modality. A), B), C) Neuropathologist 1, 2, and 3, respectively. D) SRH only comparison for all neuropathologists.

pattern, and nuclear shape, among others in combination with clinical history and neoplasm location to progress from differential diagnosis to the final diagnosis. Because the generation of the final diagnosis is involved, we benefit from understanding what histopathological features were discrepant on SRH. Moreover, we are comparing how H&E stained frozen, and FFPE sections perform in the same situation as SRH to isolate quality drawbacks of SRH from possible pathologist variability inherent to the diagnostic process. Table 2.1 shows a summary of our survey findings. The percent agreement highlights the absolute proportion of cases that agree with the collaborating pathologist G. J.-S. (histopathological features and differential diagnosis) and the neuropathology report (final diagnosis). Concordance based on Cohen's kappa (κ_C), is also reported. Interpathologist reliability is assessed using Fleiss's kappa (κ_F). To limit the impact of interpathologist variation, we report a relative accuracy defined as a ratio of SRH percent agreement and H&E FFPE to highlight the performance of SRH relative to the gold standard.

Overall, the SRH percent agreement for histopathological features is approximately the same as the percent agreement for FFPE and frozen sections between neuropathologists. However, the interpathologist reliability for SRH is consistently lower within a given histopathological feature. These findings could be explained by the fundamental difference of tissue handling in SRH as measurements are conducted on fresh tissue and the final appearance of cellular features as well as tissue architecture could be slightly different when compared to frozen and FFPE. Additionally, the inherent differences in color scale between SRH and H&E stained sections could affect the assessment of the architectural growth pattern. For example, the myxoid and chondroid architectural growth patterns are not visualized sufficiently, as supported by our survey, on SRH due to the proteinaceous background being recolored darker than what is found typically on H&E. Despite the possible shortcomings of SRH when evaluating individual histopathological features, the differential diagnosis was developed successfully (average of 94%, Table 2.1).

Using the histopathological features and clinical history, as mentioned above, the neuropathologist narrowed down the differential diagnosis to the final diagnosis with an average

percent agreement of 81% (Table 2.1). Figure 2.5 shows a closer look at the cases used in the assessment and specifically what cases received the discrepant diagnoses. Based on our evaluation, we find two tumor types that are most prone to discrepancies in the final diagnosis when using SRH images: schwannoma and chondrosarcoma (Figure 2.5D). In the case of chondrosarcoma, only one of the three neuropathologists includes the entity on their differential diagnosis. One plausible cause for this is the component composition of this tumor type. Chondroid neoplastic cells produce a cartilaginous matrix low in lipid content with occasional intracytoplasmic hyaline globules in lower grade tumors. Because both the cartilaginous matrix and hyaline globules will have SRS signal in the protein channel with minimal lipid content for additional contrast, chondrosarcoma cases can be challenging to diagnose using SRH (Figure 2.4J). Such an issue is mainly due to the requirement of having to match the H&E color scheme.

For the case of schwannomas, we have found that neuropathologists frequently qualify their decision when arriving at a final diagnosis for spindle cell tumors such as meningioma and schwannoma. For all neuropathologists, the differential diagnosis for such cases is correct. Pathologists may remain cautious with final diagnoses during intraoperative consultations, explaining that spindle cell neoplasm can be either schwannoma or meningioma, with the understanding that differentiation between those two entities will not have a significant impact on the immediate surgical management. In such cases, the final classification can be deferred to FFPE sections where additional histological examination and ancillary stains performed as needed can provide the necessary information to arrive at a definitive diagnosis.

Finally, SRH provides enough information for a neuropathologist to render the final diagnosis with an average percent agreement of 81% and relative accuracy of 87% (Table 2.1). The neuropathologist rated confidence score correlates with percent agreement. This correlation is expected as the more confident a neuropathologist feels using SRH images, the more accurate their diagnosis is expected to be. Although the objective of our study was to see how SRH performs without the use of training data sets, it is relevant to highlight that slight differences between SRH and conventional H&E staining impacts confidence and,

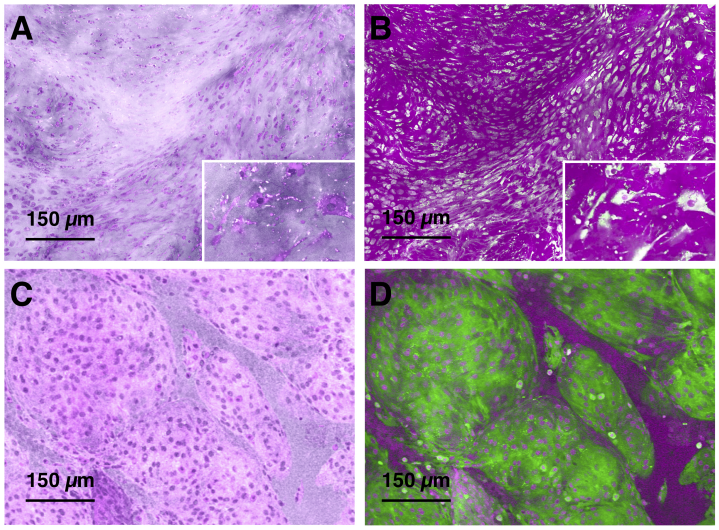

Figure 2.6: Chondrosarcoma *versus* meningioma. A) Pseudo-H&E recolored SRH of chondrosarcoma case. B) Lipid (green, appears light green in this image) and protein (magenta) SRS of chondrosarcoma case. C) Pseudo-H&E recolored SRH of meningioma case. D) Lipid (green) and protein (magenta) SRS of meningioma case.

by extension, diagnostic accuracy. This issue could be mitigated with SRH interpretation training that would be necessary for clinical application of SRH.

2.8 Additional chemical information improves diagnosis of SRH

After evaluating the types of tumors that are discrepant on SRH images, we identified that low stromal lipid concentration (as in the case of chondrosarcoma) could be challenging for pseudo-H&E recoloring. In conventional H&E staining, hematoxylin preferentially stains nucleic acids dark purple, highlighting nuclear features, whereas eosin stains protein content various shades of pink and red. Pseudo recoloring used in SRH relies on contrast from lipid and protein to recolor protein signal purple, enabling clear visualization of the nucleus. However, the requirement to pseudo-H&E recolor SRS images in SRH limits how chemical information from SRS is presented, which underutilizes the differences in protein and lipid in stromal or cytoplasmic components. The information on lipids is not available in conventional

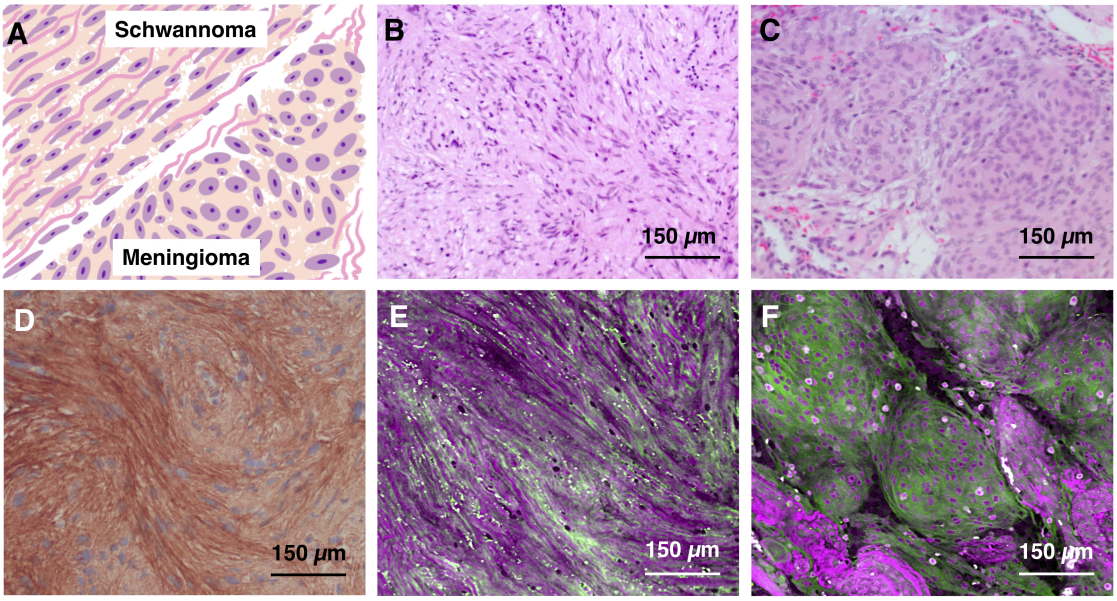

Figure 2.7: SRS images improve the identification of collagen. A) Depiction of architectural and morphological differences between meningioma and schwannoma with particular focus on collagen fibers. B) H&E of schwannoma. C) H&E of meningioma. Protein signal is shown in magenta while lipid signal is shown as green. D) Sample of collagen type IV antibody stained schwannoma case. E) SRS based image of schwannoma. F) SRS based image of meningioma.

H&E.

Although this study is focused on evaluating the diagnostic utility of SRH, it is important to emphasize that protein and lipid information from SRS is available to augment the use of SRH in intraoperative consultation. This can be exemplified in two different cases.

Firstly, the studied chondrosarcoma case was misclassified as meningioma due to perceived similarities on SRH (Figures 2.6A and 2.6C). However, direct analysis of the protein and lipid SRS images of SRS recolored in magenta and green (Figures 2.6D *versus* 2.6B) shows a high lipid signal in the case of meningioma, while in chondrosarcoma, the supporting cartilaginous matrix is protein-rich. The SRS-based data matches the general knowledge that chondrosarcoma cells can be found in a matrix that is predominantly cartilage, made almost exclusively of protein. Information provided by SRS can thus facilitate a confident diagnosis of chondrosarcoma.

Secondly, the occasional challenge of differentiating meningioma and schwannoma cases can be overcome with SRS lipid and protein information without having to resort to immunohistochemistry staining. In schwannoma, the collagen fibers often are present between neoplastic cells in contrast to meningioma, where the collagen fibers usually surround the group of neoplastic cells that can be found in a lobular pattern (Figure 2.7A). These histological features are subtle when using H&E-stained FFPE sections (Figures 2.7B and 2.7C), but can be distinguished with immunohistochemistry (Figure 2.7D). To assist with the differentiation of meningioma from schwannoma using SRS, we can highlight collagen fibers using magenta (protein) and green (lipid) colors in combination with simple linear remapping that correlates the color intensity to the concentration of the constituent of interest. In addition to simulated H&E, the protein and lipid data contrasted in the new color scheme allows for more efficient highlighting of collagen fibers and determining whether they are present in between neoplastic cells (Figure 2.7E) or are present around meningioma lobules (Figure 2.7F), allowing us to separate schwannoma from meningioma.

In summary, we highlight in Figure 2.6 and Figure 2.7 that using the lipid and protein chemical information, a pathologist could better visualize the collagen fibers in schwan-

noma cases and discern collagenous matrix of chondrosarcoma from lipid-rich tumors such as meningioma respectively. Furthermore, the SRS ability to detect collagen fibers can be used as a surrogate for immunohistochemistry, which could improve the diagnostic process intraoperatively in addition to saving money on expensive antibody reagents.

2.9 Summary and Outlook

SRH has shown great promise in intraoperative diagnosis of a limited subset of neoplastic entities, particularly glial tumors. However, the broad utility of SRH and challenges it may face in more diverse tissue remains largely unknown. Furthermore, the evaluation of the diagnostic accuracy conducted in previous studies has only focused on comparing SRH to H&E frozen sections and clinical diagnosis rendered intraoperatively [39, 40]. However, the gold standard in surgical pathology is the use of H&E stained FFPE sections in combination with ancillary studies, including immunohistochemistry, which requires time-consuming tissue processing as well as pathological interpretation. We address the gaps in testing SRH diagnostic capability using the reported original neuropathological diagnosis established for a given case and compare SRH to conventional modalities while accounting for interpathologist variability. In order to thoroughly assess the diagnostic utility of SRH, it is important to modularize the evaluation process to determine precisely the areas where SRH based technology needs improvement. We achieve that by assessing the efficacy at multiple steps on the way to final diagnosis as well as checking the neuropathologist confidence when using the new modality.

Taking our unique evaluation approach, we find that neuropathologists were able to establish a neoplasm description, architectural pattern, and nuclear shape with practically the same percent agreement as conventional modalities. Following the diagnostic process, we find that neuropathologists generate differential diagnosis successfully and final SRH diagnostic capability is very close to conventional modalities. In addition to demonstrating the diagnostic capabilities of SRH on this subset of tumors, we demonstrate supporting

findings that SRS chemical information with lipid and protein can further help diagnostic process and possibly reduce the need of immunohistochemistry use in selected cases.

At the same time, one of the main challenges that the SRS technique is likely to face in broader organ applications is the reliance on lipid and protein contrast to visualize nuclear features which are important to render a pathological diagnosis. For many neoplastic entities, protein/lipid-based simulation of H&E works well. However, for situations where lipid is limited in the cytoplasm, or otherwise nearby stroma, a map of local protein concentration provided by SRS might not be sufficient for successful visualization of a nucleus and general cellular morphology. New recoloring schemes can be considered to mediate such a problem. Nuclear segmentation has been reported in H&E stained slides, fluorescence images, and SRS images[59, 60, 61]. With nuclear segmentation, a separate recoloring technique can be employed. However, incorporating separate recoloring techniques must be generalized across different entities to reduce user variability and avoid inconsistent simulation of H&E. Such inconsistencies can prompt the pathologist to misclassify the type of neoplasm with a detrimental consequence to patients. Moreover, when designing new recoloring schemes, it is essential to use a consistent method without *a priori* knowledge of H&E as such knowledge would not be available in an intraoperative setting.

In conclusion, we have studied a diverse set of skull base tumors using fast simultaneous 2-channel SRS imaging and new pseudo-hematoxylin and eosin (H&E) recoloring methodology. Due to label-free non-destructive features of SRS technique, we demonstrated that most challenges with cryosectioning and limited amounts of fragile tissue during intraoperative consultation could quickly be addressed using SRS based approach. Using a diverse set of tumors, we determined the potential drawbacks of pseudo-H&E recoloring in selected cases involving insufficient nucleus visualization. While agreeing with previous work on SRS accuracy in intraoperative setting, we determined that SRS is capable of mostly matching the conventional H&E based technique and more importantly, additional diagnostically useful information. By following the diagnostic process that a pathologist uses, we discovered that pseudo-H&E recoloring, lipid/protein chemical information, and additional pathologist

training to interpret this new information must be considered in tandem to bring SRS into clinical practice.

2.10 Supplementary Material

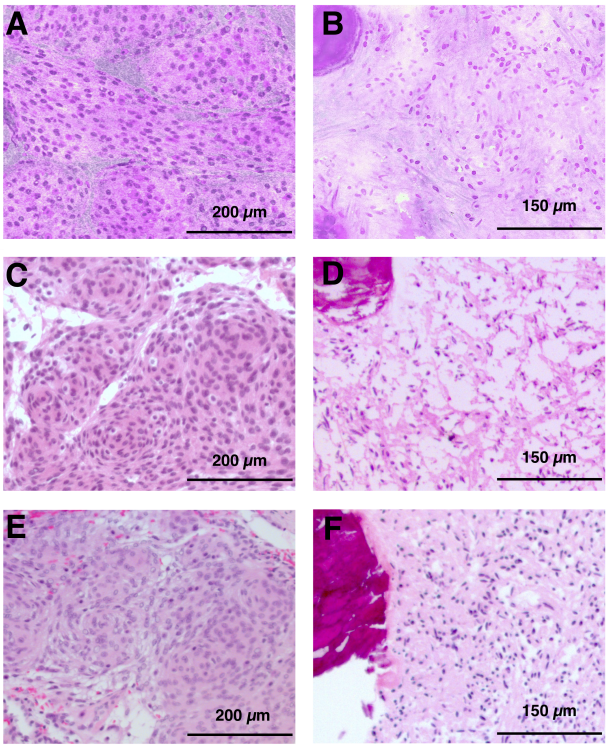

Figure 2.8: Comparison of meningioma with and without preoperative endovascular embolization treatment. A) SRH of meningioma case without preoperative embolization. B) SRH of meningioma case with preoperative embolization. C) H&E stained frozen section of meningioma case without preoperative embolization. D) H&E stained frozen section of meningioma case with preoperative embolization. E) H&E stained FFPE section of meningioma case without preoperative embolization. F) H&E stained FFPE section of meningioma case with preoperative embolization.

Chapter 3

QUANTITATIVE CHEMICAL IMAGING OF BREAST CALCIFICATIONS IN ASSOCIATION WITH NEOPLASTIC PROCESSES

3.1 Preface

During my first year with Fu lab, there was an opportunity to apply for funding through the Institute of Translational Health Sciences. While conducting the background research for possible candidates, I came across the topic of chemical composition of breast calcifications. Already at that point I began to understand the advantages SRS had to offer, including high resolution chemical information. Applying SRS hyperspectral imaging to interrogate the chemistry of breast calcifications became an important part of my work allowing me to pursue biomineralization and bone as topics of interest. In fact, over the course of research pertaining to breast calcifications, I drew a lot of inspiration from bone structure and was able to view breast calcifications in a unique manner. For example, thinking of bone and breast calcifications together prompted me to emphasize the use of SHG in this research leading to exciting results.

During the course of this project, I had to draw from the knowledge imparted by many attendings during my Post Sophomore Fellowship in pathology at the University of Washington Medicial center completed in 2017 before graduate school. In particular, Dr. Suzanne Dintzis had dedicated valuable time and resources to support the research. Also, case selection and tissue procurement was a monumental effort and the support from folks at the Northwest Biotrust (Seattle, WA) is appreciated. In particular, Sarah Bowell introduced me to many logistical issues as we looked for cases and provided a lot of support. Piper Driskell was very helpful and generous as we coordinated procurement of deidentified patient histories

and other valuable supporting material.

Another important contribution was that of Benjamin Figueroa. During 2017-2018, Benjamin Figueroa developed a parabolic fiber amplifier source setup to broaden the spectral capability of the SRS microscopy setup we used. This capability was very beneficial to my research improving the quality of chemical imaging significantly. In addition, Benjamin Figueroa supported the development of my skills with optics. Troubleshooting issues with signal, rebuilding the optical setup prior to the microscope with feedback and expertise has played an important role in my experience during graduate studies.

Finally, during this project, I had an opportunity to mentor and be supported by generous help from the undergraduates in our group: Mint Laohajaratsang and Shuaiqian Men. They both worked with me on method development, data collection, and data processing among many things. Their contribution was very important.

The following material in this chapter is reproduced with permission from:

Kseniya S. Shin; Mint Laohajaratsang; Shuaiqian Men; Benjamin Figueroa; Suzanne M. Dintzis; Dan Fu; "Quantitative chemical imaging of breast calcifications in association with neoplastic processes," *Theranostics* **10(13)**, 5865-5878 (2020). Copyright 2020 Theranostics.

3.2 Abstract

Calcifications play an essential role in early breast cancer detection and diagnosis. However, information regarding the chemical composition of calcifications identified on mammography and histology is limited. Detailed spectroscopy reveals an association between the chemical composition of calcifications and breast cancer, warranting the development of novel analytical tools to better define calcification types. Previous investigations average calcification composition across broad tissue sections with no spatially resolved information or provide

qualitative visualization, which prevents a robust linking of specific spatially resolved changes in calcification chemistry with the pathologic process. To visualize breast calcification chemical composition at high spatial resolution, we apply hyperspectral stimulated Raman scattering (SRS) microscopy to study breast calcifications associated with a spectrum of breast changes ranging from benign to neoplastic processes, including atypical ductal hyperplasia, ductal carcinoma in situ, and invasive ductal carcinoma. The carbonate content of individual breast calcifications is quantified using a simple ratiometric analysis. Our findings reveal that intra-sample calcification carbonate content is closely associated with local pathological processes. Single calcification analysis supports previous studies demonstrating decreasing average carbonate level with increasing malignant potential. Sensitivity and specificity reach $>85\%$ when carbonate content level is used as the single differentiator in separating benign from neoplastic processes. However, the average carbonate content is limiting when trying to separate specific diagnostic categories, such as fibroadenoma and invasive ductal carcinoma. Second harmonic generation (SHG) data can provide critical information to bridge this gap. SRS, combined with SHG, can be a valuable tool in better understanding calcifications in carcinogenesis, diagnosis, and possible prognosis. This study not only reveals previously unknown large variations of breast microcalcifications in association with local malignancy but also corroborates the clinical value of linking microcalcification chemistry to breast malignancy. More importantly, it represents an important step in the development of a label-free imaging strategy for breast cancer diagnosis with tremendous potential to address major challenges in diagnostic discordance in pathology.

3.3 Introduction

Calcifications associated with breast disease are critical to breast cancer screening as they are often the only discernible indicator of risk in mammography [62]. Because of their importance in diagnostic radiology, it is essential to associate features of calcifications (e.g., distribution and morphology) with the ultimate pathology diagnosis. Several studies have

found that casting-type calcifications are associated with carcinoma of high histopathological grade and more extensive disease [63, 64, 65]. The assessment and identification of casting-type calcifications is based on architectural pattern, described with terms such as "intermittent" and "branching." Carcinomas with casting-type calcifications are correlated with poor prognosis, including increased likelihood of lymph node metastasis, increased risk of recurrence, and decreased survival [66, 67, 68].

Despite their diagnostic and prognostic potential, the morphologic and chemical features of calcifications are poorly understood, in part due to technological limitations. Morphological features of calcifications identified by mammography are insufficient for accurate diagnosis and prognosis. In addition, smaller calcifications ($<$0.1mm) are undetectable using mammography [64]. While histological studies can identify smaller ($<$0.1mm) calcification, they are mostly limited to crude morphological information and prone to sectioning artifact. Accumulating evidence demonstrating the importance of calcification type in breast cancer progression underscores the need to develop tools to more fully characterize calcifications [69, 70, 71, 72]. Moving beyond morphology and distribution patterns in breast calcification, studies utilizing X-ray diffraction and electron microprobe analysis with scanning electron microscopy (SEM) have contributed to an earlier understanding of calcification chemical differences [72, 73, 74, 75]. The type I (calcium oxalate) calcifications were found in predominantly benign processes and often appeared translucent on hematoxylin and eosin (H&E) stained tissue slides. The type II (calcium hydroxyapatite) calcifications were found in both benign and malignant processes and appear intensely purple as they absorb hematoxylin on H&E slides. Spectroscopic methods such as Raman spectroscopy (RS) [76, 77, 78, 79, 80] and Fourier-transform infrared spectroscopy (FTIR) [81] demonstrated chemical differences in calcifications associated with benign and malignant breast disease. The carbonate content of hydroxyapatite has been shown to be inversely correlated with malignancy [81]. Additional studies probed the correlation of malignancy with another component of microcalcifications - whitlockite (tricalcium phosphate and magnesium-substituted beta-tricalcium phosphate) [80, 82, 83, 84, 85].

While offering information about calcification chemistry, most spectroscopic methods average calcifications within multiple ducts within a tissue section, irrespective of the heterogeneous pathologic processes among adjacent ducts. Spatially resolved methods such as FTIR imaging have limited resolution and throughput, prohibiting visualization of calcification composition variation within adjacent ducts and lobules. Moreover, tissue protein content is recognized to correlate with malignancy [81, 86], and small case set correlative studies provided supporting evidence of complex heterogeneity of calcifications [80, 87]. However, no detailed quantitative studies have been conducted focused exclusively on calcification underlying matrix co-localized with mineral components and diagnostic value of such information. To address this gap in understanding calcification variation within tissue microenvironments, we use stimulated Raman scattering (SRS) microscopy, an advanced Raman imaging technique, to map the chemical composition of breast calcifications (mineral constituents and underlying matrix) and associated neoplastic processes with unprecedented spatial resolution and chemical specificity. SRS uses two ultrashort laser pulses to coherently excite molecular vibrations with orders of magnitude higher efficiency than spontaneous Raman, thereby enabling rapid chemical imaging at submicron spatial resolution [88, 20, 61]. The photon energy difference between the two lasers corresponds to the vibrational bond energy of the molecule of interest. By sequentially tuning the frequency difference of the two excitation lasers, different Raman modes can be selectively excited and allow construction of a hyperspectral SRS dataset with each spatial pixel containing an SRS spectrum. Based on the distinct Raman features of target molecules, they can be separately imaged and quantified. SRS has now been widely used to quantify the spatial distribution of various soluble small molecules such as neurotransmitters, metabolites, and small drug molecules [89, 90, 91]. SRS has also shown promise for label-free histopathology applications, where the intrinsic vibrational contrasts of lipids and proteins are used to provide H&E equivalent information without any sectioning, fixation, or staining [61, 39, 42, 92].

We utilize the high resolution and chemical specificity SRS offers to deliver an unprecedented level of detail when analyzing calcifications. Additionally, we incorporate second

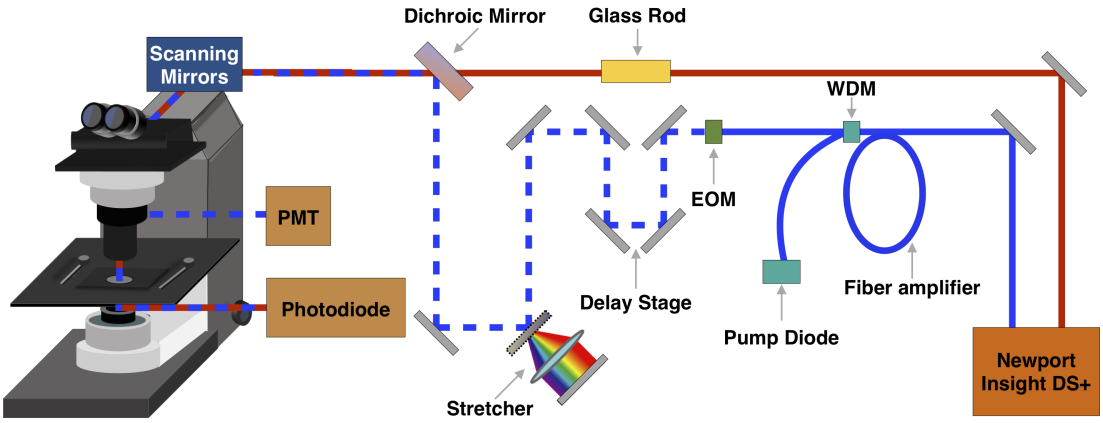

Figure 3.1: Schematic representation of stimulated Raman scattering (SRS) and second harmonic generation (SHG) microscopy experimental setup. EOM - electro-optic modulator. PMT - photo-multiplier tube. WDM - wavelength division multiplexer.

harmonic generation (SHG) which has been proven effective at visualizing collagen in the tumor microenvironment [22]. SHG added to SRS helps visualize collagen, including both stromal collagen and collagen within the calcification matrix. Our results reveal significant intra-patient heterogeneity of calcifications that are tightly associated with the underlying pathological process. Interpatient analysis demonstrates that the carbonate content percentage decreases as the malignancy potential increases. Moreover, calcifications have protein-containing underlying matrix that is unique to specific neoplastic processes. Finally, we determine that carbonate content, in combination with SHG data, is very effective in separating benign from neoplastic processes.

3.4 Experimental Methods

3.4.1 SRS and SHG imaging

A broadband femtosecond dual-beam laser system (Insight DS + from Spectra-Physics) was used for SRS and SHG (Figure 3.1). The details of the experimental setup for broadband

SRS measurements has been described in a previous publication [55]. Briefly, the two output beams from the Insight laser system are used at 80 MHz repetition rate: a tunable beam (pump) and a fixed beam (Stokes). The pump beam is centered at 798 nm for CH region and 944 nm for fingerprint region. The Stokes beam is amplified with a parabolic fiber amplifier to increase the bandwidth and pulse duration [93]. We note that the use of this laser is critically important for this study because of the improved spectral resolution, coverage, and background suppression. Temporally dispersed pump and Stokes pulses are combined at a dichroic mirror and sent into a home-built laser scanning microscope. A 25x Olympus water immersion objective (NA = 1.05) is used to focus the beams on the sample. At the focus, the pump and Stokes beams have an average power of 40 mW each. Stimulated Raman loss (SRL) signal is detected with an amplified photodiode and a lock-in amplifier (Zurich Instrument HF2LI). For SRS imaging, a stack of frames with single field of view (FOV) of 285 μm x 285 μm (512 pixels x 512 pixels) is acquired, for which the pixel dwell time is 8 μs and time to acquire each frame is 2 s. The frames are acquired every 2 cm^{-1} for total of 90 frames per stack. For SHG, a dichroic mirror (Chroma 695dcxr) is placed before the objective to allow for epi-collection of SHG signal from the sample. The SHG signal is detected by a photo-multiplier tube (Hamamatsu H10770PA-40) using 485 nm long pass and 650 nm short pass filters.

3.4.2 Calibration sample preparation

Calcium hydroxyapatite (HAP) and 10% carbonated hydroxyapatite (CHAP) were obtained from Sigma Aldrich and Clarkson Chromatography Products respectively. Both solid controls were ground using mortar and pestle. A total of five mixtures were prepared for calibration purposes (0%, 2.5%, 5.0%, 7.5%, 10% carbonate content). The calibration samples were placed between a coverslip and a microscope slide for SRS imaging.

3.4.3 Breast tissue specimens

Breast tissue was obtained from 17 patient archival cases (including biopsy and resection) managed by Northwest Biotrust, Seattle, WA. The initial case selection was based on the pathology report (calcifications present in association with desired pathological process). Slides were subsequently reviewed to confirm the histologic diagnoses (SMD, KSS). Formalin-fixed paraffin-embedded tissue blocks were retrieved from archives and sectioned at 4-μm and mounted on charged slides. One section was H&E stained to identify pathological process. The adjacent section was deparaffinized and coverslipped for SRS and SHG analysis. The areas of interest were identified in the bright field based on selected areas of interest on adjacent H&E stained slides. A total of 214 breast calcifications were imaged, including: 31 non-neoplastic calcifications (including normal ducts and adenosis), 27 fibroadenoma (FA) associated calcifications, 8 atypical ductal hyperplasia (ADH) associated calcifications, 36 ductal carcinoma in situ (DCIS) associated calcifications, 112 invasive ductal carcinoma (IDC) associated calcifications. Table 3.1 in Supplementary contains more detailed case description and additional clinical history.

3.4.4 Breast tissue specimens

Calibration samples with 0%, 2.5%, 5.0%, 7.5%, 10% carbonate content in calcium hydroxyapatite mixtures were imaged using the hyperspectral SRS microscope described above. Using SRS intensities at carbonate ($\sim$ 1070 cm^{-1}) and phosphate ($\sim$ 960 cm^{-1}) peaks corrected for background [94], the ratio was determined for each mixture (Figure 3.2A), which was plotted as a function of carbonate content percentage (Figure 3.2B). Using linear regression, the slope and intercept were determined and applied to convert the ratio described above into carbonate content percentage in hydroxyapatite.

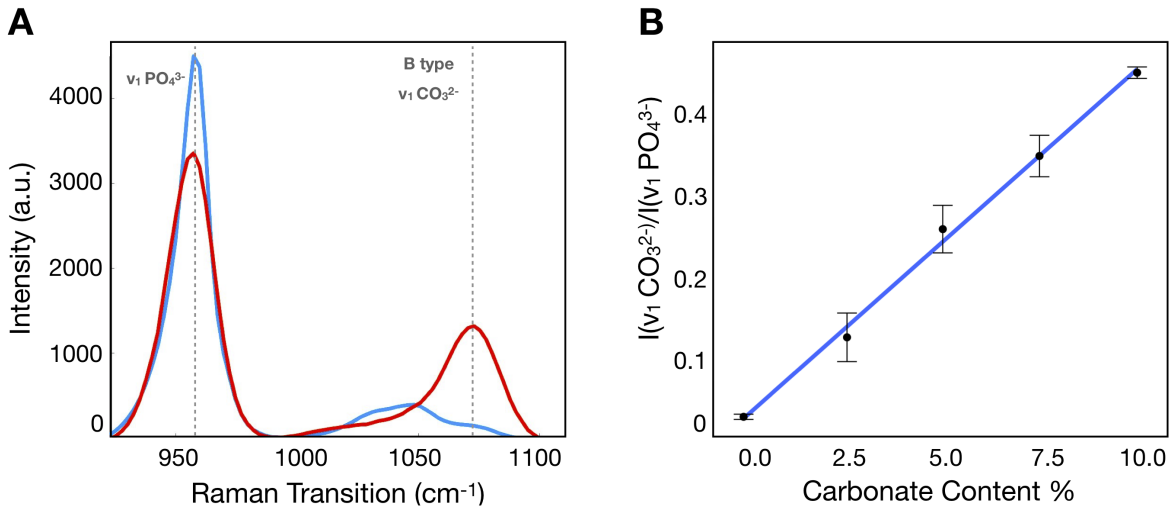

Figure 3.2: Calibration process to determine carbonate content in hydroxyapatite. A) SRS spectra of hydroxyapatite (blue) and carbonated hydroxyapatite (red) controls. B) Calibration curve correlating ratio of peaks at carbonate and phosphate Raman transitions.

3.4.5 Tissue imaging and image processing

Our imaging and data processing workflow are described in Figure 3.3A. Samples were imaged in both high wavenumber (C-H stretching) and fingerprint region of the Raman spectrum. The hyperspectral datasets were acquired in both regions. Figure 3.3B shows the SRS spectra of controls (CHAP and HAP) used to verify identified calcifications as well as collagen and cellular material (see Figure 3.10 in Supplementary for a focused presentation of cell bodies that are not easily visualized in current figure). SRS images at phosphate and carbonate Raman transitions (Figures 3.3C and 3.3D) were background corrected and divided to generate a map of carbonate to phosphate ratio. The mask based on phosphate intensity (Figure 3.3F) was applied to the images to isolate only data co-localized with phosphate (the main calcification component). Using the calibration curve determined from control samples, the ratio value was converted to carbonate content percentage (Figure 3.3G). Images at phosphate and phenylalanine Raman transitions (Figures 3.3C and 3.3E) were used to gen-

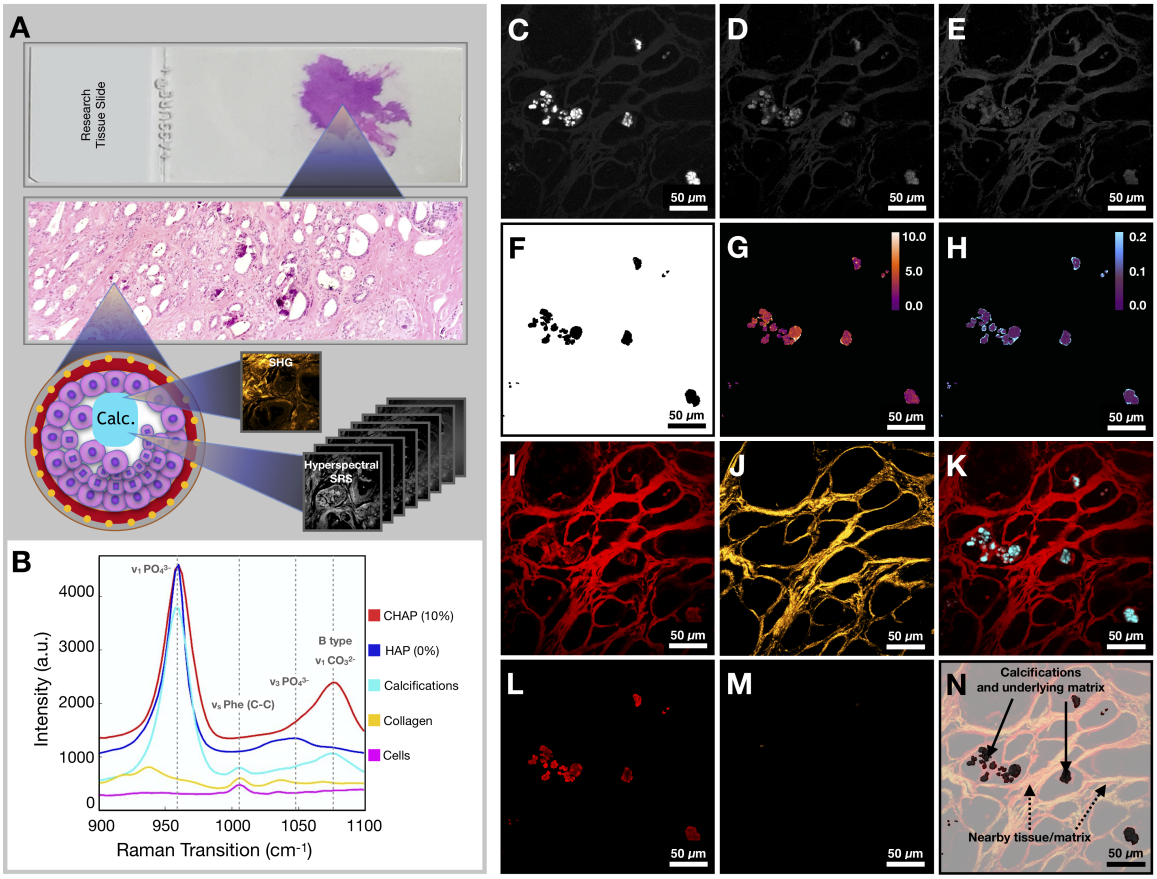

Figure 3.3: Workflow for tissue imaging and image processing. A) Diagram depicting imaging of the field of view to yield hyperspectral SRS and SHG information. B) Spectra of controls (CHAP and HAP) and spectra from various components encountered in breast tissue (calcifications, collagen, and ductal cells). C) Image at phosphate transition ($\sim$ 960 cm^{-1}). D) Image at carbonate Raman transition ($\sim$ 1070 cm^{-1}). E) Image at phenylalanine Raman transition ($\sim$ 1005 cm^{-1}). F) Phosphate image-based mask used to isolate calcifications only. G) Carbonate content % map (mask applied). H) Phenylalanine to phosphate ratio map (mask applied). I) Image at CH Raman transition ($\sim$ 2930 cm^{-1}). J) SHG image. K) Composite of CH (red) and phosphate (cyan) images. L) CH Image (mask applied). M) SHG image (mask applied). N) Diagram depicting nomenclature used in the manuscript.

erate a phenylalanine to phosphate ratio map (Figure 3.3H). Figure 3.11 in Supplementary depicts additional examples of image processing. Additionally, the SRS image corresponding to a protein Raman transition (~ 2930 cm^{-1}) was used to visualize tissue morphology of the FOV (Figure 3.3I). The SHG intensity image from the same FOV was collected to provide information on collagen (Figure 3.3J). The combination of protein and phosphate images provided visualization of the calcification location (Figure 3.3K). The mask (Figure 3.3F) was applied to CH (Figure 3.3L) and SHG images (Figure 3.3M). While the CH image was only used for verification of calcification underlying matrix (Figure 3.3N), the SHG image was masked using the same phosphate-based mask to isolate SHG signal only from collagen within calcifications for further statistical analysis.

3.4.6 Statistical analysis

For each parameter (carbonate content percentage, phenylalanine to phosphate ratio, and SHG intensity) the average, for a given category (benign, ADH, DCIS, IDC, FA), was calculated with the standard deviation reported as an error bar. The differences between categories were assessed using p-values calculated from Student's t-tests. The receiver operator curves (ROC) were calculated using R software to assess the sensitivity and specificity for each parameter. Maximum Youden's index was used to determine sensitivity and specificity values.

3.5 Results and Discussion

3.5.1 SRS imaging provides spatially resolved quantification of carbonate content in hydroxyapatite

Previously, the carbonate content in hydroxyapatite has been measured using RS [77, 79, 86, 95] without detailed understanding of spatial distribution. Here, we use pure HAP and commercially synthesized 10% CHAP to demonstrate that ratiometric analysis of SRS

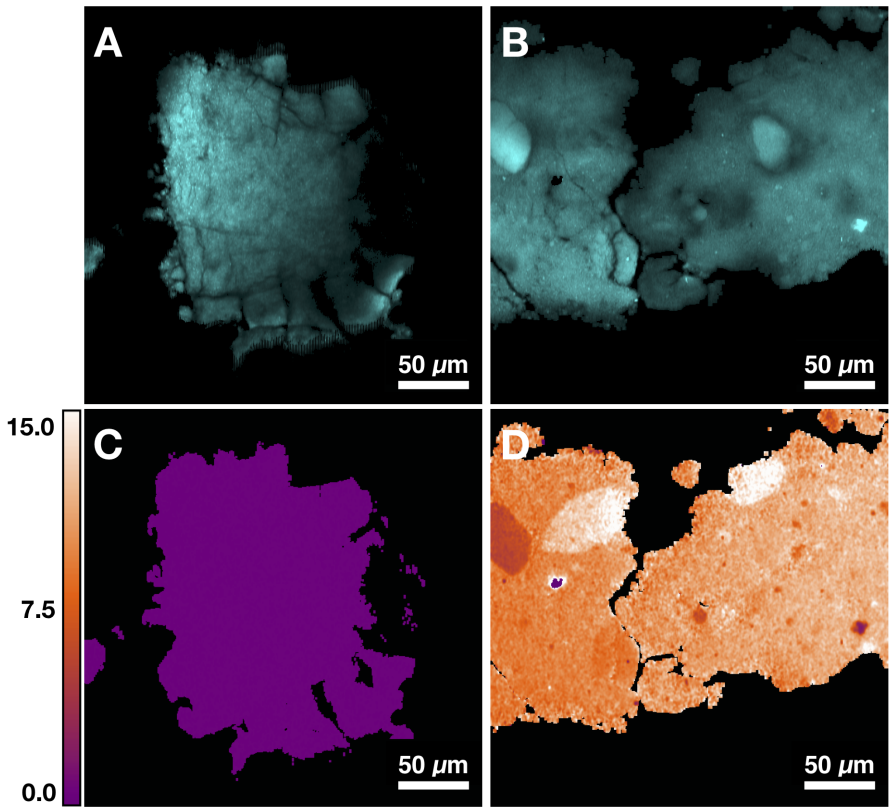

Figure 3.4: Quantification of carbonate content in hydroxyapatite (HAP) based on control samples. A) Image at phosphate Raman transition (960 cm^{-1}) for pure HAP. B) Image at phosphate Raman transition (960 cm^{-1}) for 10% carbonated hydroxyapatite (CHAP). C) Carbonate content map for HAP. D) Carbonate content map for 10% CHAP.

images can deliver a high-resolution spatial map to assess variations of carbonate content in CHAP. Reproducible and reliable quantification of carbonate content is necessary to study how tissue microenvironment influences calcification characteristics.

Figures 3.4A and 3.4B demonstrate two control samples (HAP and 10% CHAP) imaged at phosphate Raman transition. Applying calibration to ratiometric SRS image of carbonate/phosphate, the carbonate content percentage maps are generated for both control samples. Figure 3.4C shows HAP as an image with almost uniform carbonate % of 0.00 ($\pm$0.00) as expected with pure HAP. Figure reffig:Figure4BD shows heterogeneous CHAP with average carbonation substitution % of 10.34 ($\pm$1.87) due to the nonuniformity of the

synthetically prepared sample. Using the high resolution and chemical specificity of SRS, we are able to resolve the fine fluctuations of carbonate content with submicron resolution. This unique capability allows us to assess the effect of metabolic changes precipitated by presence of cancer in breast tissue on calcification composition.

3.5.2 Calcifications are heterogeneous within a single patient

Breast tissue submitted for pathological examination often contains calcifications in multiple ducts, which may represent various pathologic processes. In previous spectroscopic studies, multiple ducts are frequently measured together, which can average calcifications associated with different processes. Isolating individual breast ducts and detailing the histopathology within the ducts allows for correlation of variation in carbonate content with local pathology.

Here, we group calcifications by specific pathological processes and not by overall case diagnosis. In Figure 3.5, we demonstrate two cases in which multiple pathological processes co-occur within the same tissue slide. Figure 3.5A shows an H&E stained section of breast biopsy core with normal ducts and a focus of DCIS. Figure 3.5B highlights the proximity of the normal ducts to the edge of DCIS focus. The H&E close up of normal ducts reveals multiple calcifications (Figure 3.5C). The corresponding carbonate content map in Figure 3.5D shows the carbonate content average of 5.13%. Calcifications from the DCIS focus are shown in Figure 3.5E. The corresponding carbonate content map in Figure 3.5F shows an average carbonate content of 2.75

Figure 3.5G shows H&E stained section of another breast resection tissue with calcifications associated with DCIS as well as IDC. Figure 3.5H highlights the proximity of the DCIS containing ducts to the calcifications associated with IDC. The stroma surrounding a duct containing DCIS is infiltrated by carcinoma cells. Figures 3.5I and 3.5J show the close-up H&E and a carbonate content map for calcifications associated with DCIS, respectively. The average carbonate content is 3.25%. Figures 3.5K and 3.5L show the close-up H&E and a carbonate content map for calcifications associated with invasive component, respectively.

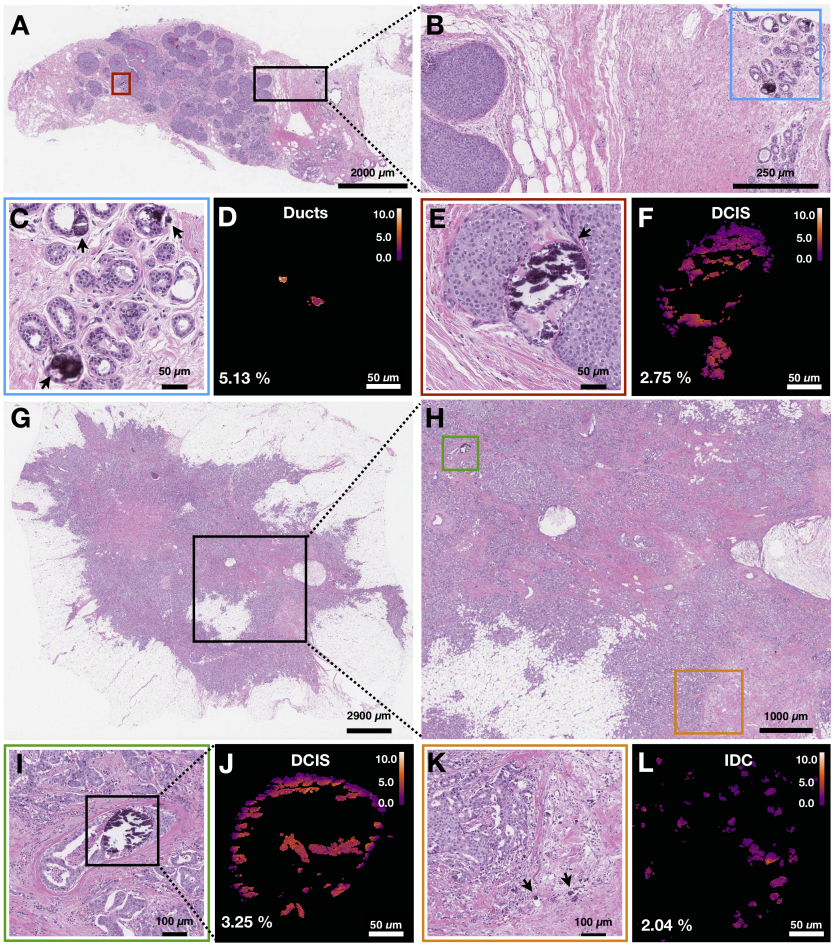

Figure 3.5: Carbonate content in calcifications varies within individual patient samples. Arrows are used to identify calcifications. A) H&E of breast biopsy core with red box highlighting DCIS ducts and black box highlighting normal ducts in close proximity to DCIS lesion edge. B) H&E close up of area highlighted in black box in A. Blue box highlights normal ducts. C, D) H&E close up and carbonate content map, respectively, of normal ducts highlighted in B. Arrows point to calcifications. E, F) H&E close up and carbonate content map, respectively, of ducts containing DCIS with associated calcifications highlighted in A. G) H&E of breast tissue resection with black box highlighting an area of DCIS admixed with IDC. H) H&E close up of area highlighted in black box (see G). Green box highlights a duct containing DCIS with associated calcifications. Orange box highlights IDC with associated calcifications. I, J) H&E close up and carbonate content map, respectively, of ducts containing DCIS with associated calcifications highlighted in H. K, L) H&E close up and carbonate content map, respectively, of IDC with associated calcifications highlighted in H.

The average carbonate content value is 2.04%.

The two cases illustrate that calcifications in the same patient case can have differing chemical composition. Although ducts are present in the same tissue section, the carbonate content associated with individual ducts is markedly different and reflects underlying pathological process. The high spatial resolution of hyperspectral SRS imaging is important to resolve calcification heterogeneity within the same patient sample and to establish the relationship between chemical composition and pathological process.

3.5.3 SRS imaging provides visualization of local breast tissue microenvironment and its influence on calcifications

Previous studies using FTIR have demonstrated that breast calcifications with lower carbonate content of CHAP correlate with malignancy [81]. Moreover, the overall protein content in tissue was noted to increase with malignancy [81, 86]. Breast calcifications may contain both organic material and mineral components. The relative amount of organic material is likely to vary in normal compared to neoplastic ducts. Furthermore, the extracellular pH becomes acidic in neoplastic tissue as a result of lactate secretion from anaerobic glycolysis [96, 97] and lower pH is likely to contribute to lower carbonate content in malignant calcifications. We hypothesize that detailed visualization of carbonate content and organic components in calcifications will reveal important features that can aid breast cancer diagnosis. Figures 3.6A-D demonstrates a graphic depiction of normal ducts progressing to IDC. The cells of the ducts undergo a series of mutations that allow bypassing of the normal checks and balances of the cell cycle. Once a cell is able to divide without internal or external controls, clonal expansion ensues. Invasive carcinoma acquires the ability to break through the basement membrane surrounding ducts and invade the stroma (gray border as depicted in Figures 3.6A-D), thereby conferring risk for lymphovascular invasion and subsequent metastasis to other organs.

The neoplastic progression from benign ducts to IDC is associated with an overall de-

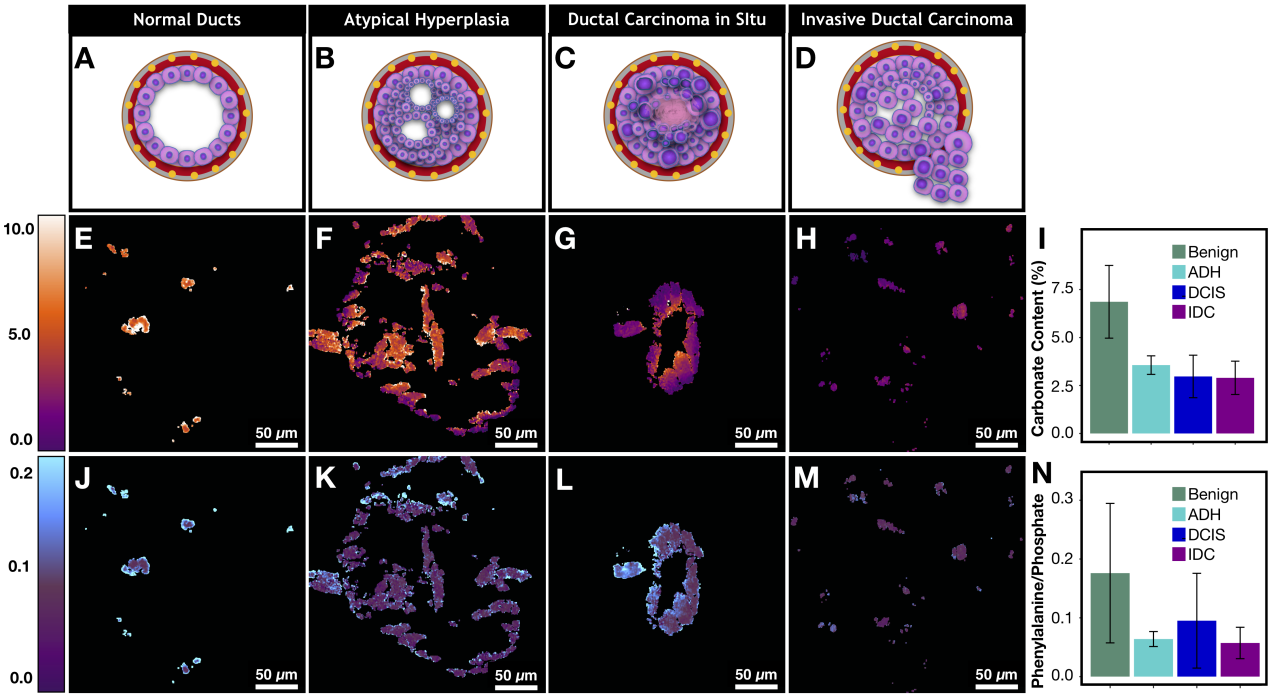

Figure 3.6: Metabolic changes associated with cancer affect calcification composition. A)-D) Graphic depiction of neoplastic progression from normal duct to invasive ductal carcinoma. E)-H) Carbonate content changes with neoplastic progression. I) Bar graph demonstrating averages for carbonate content across pathological categories. J)-M) Phenylalanine to phosphate ratio changes with neoplastic progression. N) Bar graph demonstrating averages for phenylalanine to phosphate ratio across pathological categories.

crease in calcification carbonate content (Figure 3.6I). Our results support previous findings from spectroscopic studies [81]. Decreased carbonate content is correlated with malignancy and by extension with increased cellular metabolism and uncontrolled division. Specifically, normal ducts have high carbonate content that averages around 6.9%. Meanwhile, atypical hyperplasia and DCIS calcifications (Figures 3.6F and 3.6G) show low carbonate content on the edges with values of 1-2% while the carbonate content in the center of ducts (100-300 μm in diameter) is much higher, approaching the values associated with non-neoplastic processes. Interestingly, when average carbonate content is grouped on a per patient basis, the difference between benign and malignant cases is much less pronounced (Figure 3.3 in Supplementary). This is due to the fact that local pathology around some calcifications may not agree with overall patient diagnosis. The discrepancy further highlights the advantage of calcification imaging over spectroscopy of bulk tissue and the need for spatially resolved measurement in heterogeneous tumor tissue, particularly when tissue size is limited such as in needle core biopsy.

Although precise quantification of the spatial distribution of carbonate in large calcifications is challenging due to sectioning artifact, our findings suggest that the carbonate content decrease on the edges of the calcifications directly reflects the changing microenvironment (i.e. higher acidity) associated with neoplastic cells and necrotic debris [40,41]. With invasive disease, the calcification carbonate content is very low (1-3%) and there is lower variation across a single calcification (Figure 3.6H). Together these observations suggest that low carbonate content on the edge of calcifications could potentially be used as a neoplastic indicator. A broader validation of this finding would benefit from unsectioned tissues samples where calcifications are not perturbed by microtome cutting.

In addition to carbonate content of hydroxyapatite, protein to phosphate ratio has also been suggested to correlate with breast cancer [81]. We are interested in understanding how calcifications interact with underlying tissue matrix. Using phenylalanine as a surrogate marker for protein [98, 99], phenylalanine ($\sim$ 1005 cm^{-1}) to phosphate ($\sim$ 960 cm^{-1}) ratio is used to quantify protein content in calcifications (Figures 3.6J-M). The phenylalanine

to phosphate ratio decreases overall when comparing benign breast to invasive carcinoma (Figure 3.6N). Additionally, there is a notable increase of protein content in DCIS. The ratio of the phenylalanine increases especially on the edges of the calcifications. The differences can be explained by necrosis that is present in many DCIS cases (a representative case is shown in Figure 3.6L) providing a lot of organic material to be admixed with calcifications.

Many theories have been put forth to explain different processes that can lead to calcifications associated with a specific pathological process. In necrotic tissue, it is believed that the areas of cell necrosis or previous microscopic cell injury activate phosphatases that bind calcium ions to phospholipid in the membrane, which incites further calcification [100]. This explains why calcifications formed in necrotic tissue are likely to be mixed with the necrotic debris and more heterogeneous, as supported by our observations of higher phenylalanine to phosphate ratio and larger variations in DCIS with necrosis (Figure 3.6L).

Moreover, recent studies have described an epithelial-mesenchymal transition of neoplastic cells that become capable of producing breast calcifications in breast carcinoma [101]. As transitioned cancerous cells invade stroma, calcifications are likely to be produced frequently and are likely to be relatively homogeneous with low organic content in the absence of loose organic material in the stroma. This mechanism is supported by our findings that show invasive cancer foci with small scattered calcifications and with relatively homogenous and low organic content (Figure 3.6M).

Overall, the SRS images reveal chemical features associated with the calcification microenvironment. Carbonate content is decreased at the edges of DCIS calcifications. Patterns such as these can only be highlighted with high resolution and chemical specificity available with hyperspectral SRS. Moreover, ratiometric phenylalanine to phosphate imaging can quantitate protein within calcifications. We observed a significant increase of protein content in DCIS compared to IDC. With additional validation, the calcification features imaged with SRS could become a part of an invaluable diagnostic tool.

3.5.4 Calcification and underlying protein matrix contain diagnostically relevant information

While phenylalanine SRS image offers an overall measure of protein content, it cannot provide details regarding the structure of organic material within the calcifications. Radiographic studies of calcification morphology and texture show that calcifications differ in various pathological processes [4,46]. The underlying organic matrix of calcifications, determined by the cellular process, affects mineralization. The composition of the underlying organic matrix varies considerably between FA and IDC. In past spectroscopic studies [20], fibroadenomas were grouped with non-neoplastic cases. FA is in fact a result of neoplastic stromal component and is hormonally responsive [47]. Using SRS, we found that FA has low carbonate content in calcifications. Low carbonate content by itself might lead to misclassification as malignant.

Figures 3.7A and 3.7C present protein information combined with phosphate as an example of common morphology for IDC and FA associated calcifications, respectively. From the images, the FA cases frequently have large and very dense calcifications, whereas IDC cases tend to present with smaller scattered calcifications. These basic morphological findings are consistent with mammography studies. Often on mammography, FA associated calcifications are described as popcorn calcifications. Such calcifications can appear dense, thick, and usually large ($\sim$ 2 mm) [102, 103]. In contrast, IDC is often associated with crushed stone, powdery, or casting-type calcifications [104, 105]. While the morphological differences are present for FA cases when compared to IDC cases, the carbonate content of hydroxyapatite is less differentiating with average of 2.24

On mammography, FA calcifications can persist over many years, whereas cancer associated calcifications can appear on mammography within months [102]. This temporal difference in calcification formation suggests that the underlying matrix organization may be a useful differentiation factor. Figures 3.7B and 3.7C show protein information (red) combined with SHG (gold). In FA cases, the SHG signal is prominent and highlights a basket

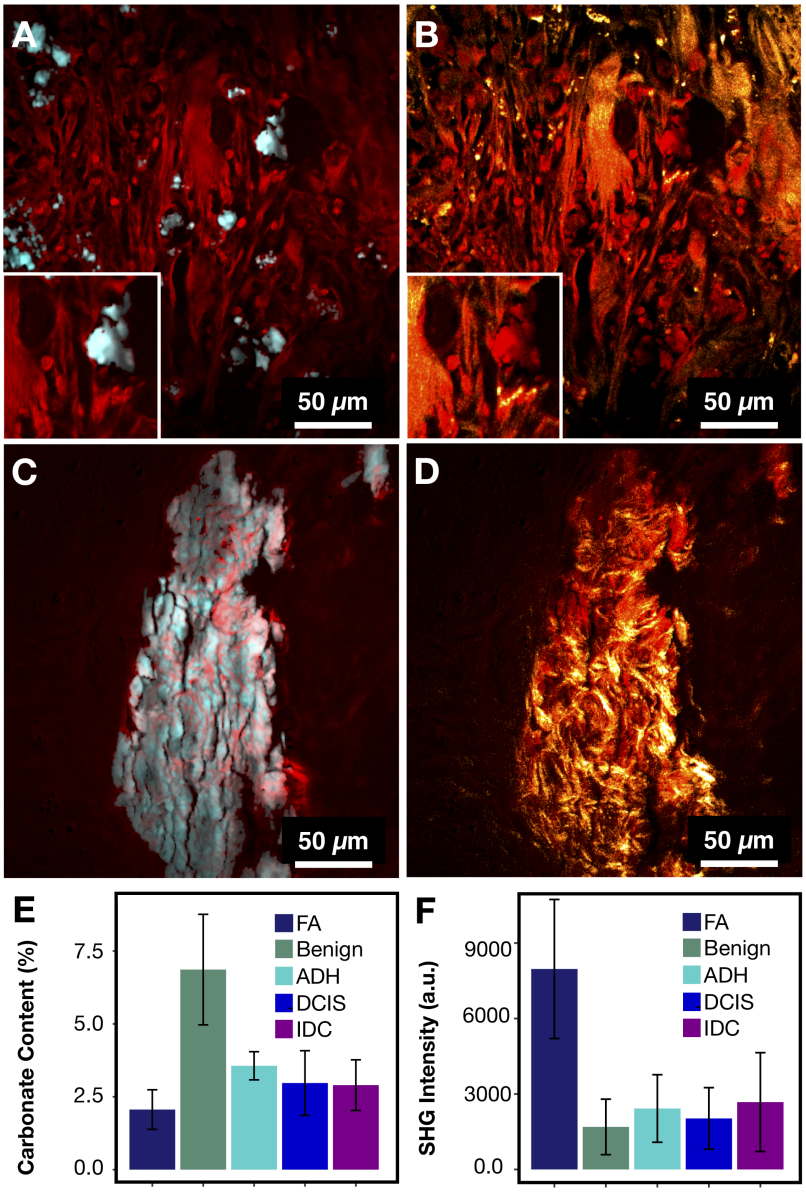

Figure 3.7: FA and IDC similarity and differences. A) IDC with protein (red) highlighting calcification underlying matrix along with stroma and phosphate (cyan) highlighting hydroxyapatite. B) IDC composite of protein (red) and SHG (gold) highlighting collagen. C) FA with protein (red) highlighting calcification underlying matrix along with stroma and phosphate (cyan) highlighting hydroxyapatite. D) FA composite of protein (red) and SHG (gold) highlighting collagen. E) Bar chart for carbonate content across all categories. F) Bar chart for SHG intensity across all categories.

weave pattern. In contrast, in IDC cases, the SHG signal highlights mostly stroma, while the calcifications themselves do not give strong SHG. Figures 3.7E-F summarize the averages of SHG signals for different pathological categories. The average SHG signal for FA is almost three time that of IDC.

In addition to distinguishing between FA and IDC, our findings offer a plausible explanation of why FA calcifications appear to be dense, large, and popcorn like. The denser organic matrix and intricate collagen network likely supports and stabilizes larger calcifications associated with FA that frequently remain unchanged for decades. In contrast, the absence of collagen or structure-reinforcing matrix in IDC calcifications lacks the structural integrity and often appear small and powdery.

In summary, FA cases can be differentiated from malignant cases using a combination of data from SRS and SHG. The differentiation is clinically crucial due to substantially different management of FA vs IDC cases. Moreover, the visualization of FA calcification underlying matrix correlates with previous radiological data.

3.5.5 Combined SRS/SHG imaging aids differentiation of neoplastic cases

Distinguishing IDC from benign ducts using standard histology is typically not considered challenging [106]. However, cases with ambiguous non-neoplastic versus neoplastic morphology, such as atypical ductal hyperplasia, demonstrate low interpathologist agreement [106]. Combining traditional H&E morphology with specific chemical signatures of calcifications could help with the overall interpretation of borderline cases and subsequently improve the diagnostic accuracy and patient outcome.

Figure 3.8A shows the receiver operating characteristic (ROC) curve for breast cancer diagnosis using carbonate content alone. The area under the curve (AUC) of 0.93 (1 for perfect model) suggests that carbonate content is a sufficient metric to separate benign from neoplastic cases. The AUC of 0.8 to 0.9 is considered excellent and above 0.9 is considered outstanding in medical practice [107]. In comparison, most recent published research [85]

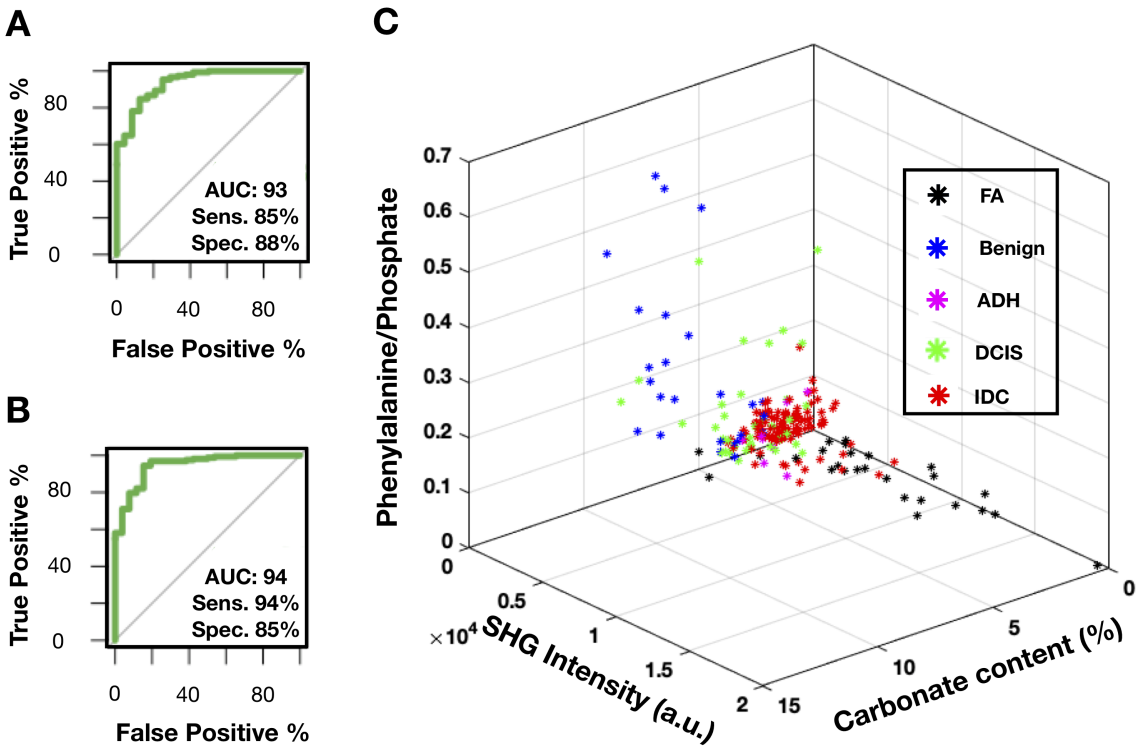

Figure 3.8: SRS and SHG imaging data statistical analysis. A) ROC curve for carbonate content as a parameter when differentiating benign and neoplastic cases. B) ROC curve for SHG intensity as a parameter when differentiating FA and IDC cases. C) Scatter plot depicting separation of cases across all diagnostic categories.

presented a complex classification model using RS data and reported ROC of 0.94 (when differentiating only pure benign and pure malignant cases). Moreover, the sensitivity of 85% and specificity of 88% as determined by maximum Youden's index is comparable to other studies utilizing carbonate content in conjunction with other parameters such as protein [81, 86]. In our case, the carbonate content alone appears to be very effective.

Provided our average carbonate content for FA category is similar to IDC, another parameter, SHG, is utilized to separate these diagnoses. Figure 3.8B presents a ROC curve for FA versus IDC determination based on SHG signal alone. The AUC of 0.94 with sensitivity of 94% and specificity of 85% as determined by maximum Youden's index supports previous observations that FA cases have markedly increased SHG signal. In contrast, IDC cases were observed to have minimal SHG signal. Using SHG intensity as a parameter, we can separate FA cases, a benign neoplastic process, from cancer.

Combining SRS determined carbonate content, phenylalanine to phosphate ratio, and SHG data, we demonstrate a successful separation for all diagnostic categories (Figure 3.8C). Benign calcifications are grouped using carbonate content with low average SHG intensity. Interestingly, DCIS (highlighted in green) calcifications lie somewhere between benign and invasive, the majority closer to invasive. Additionally, ADH mostly clustered adjacent to DCIS. This co-localization of ADH and DCIS is consistent with the general understanding that ADH is not a unique biological category, but rather a diagnostic catch-all designated to indicate ambiguous morphology. The consensus amongst pathologists is that many ADH cases are biologically indistinguishable from low-grade DCIS.

In summary, SRS data provides high sensitivity (85%) and specificity (88%) when identifying benign and invasive processes. SHG data provides a parameter separating FA from IDC cases with high sensitivity (94%) and specificity (85%). Phenylalanine to phosphate ratio provides additional separation between DCIS and IDC. Together, spectroscopy and morphology can be utilized to better establish the malignant potential in cases with ambiguous morphology on H&E alone.

3.5.6 Additional mineral species and their effect on ratiometric analysis

CHAP is not the only microcalcification species that was identified in breast cancer. Although whitlockite typically accounts for a tiny percentage of breast calcifications [22], it has been suggested that the presence of whitlockite species (tricalcium phosphate and magnesium substituted tricalcium phosphate) could potentially aid diagnosis [19,21-24]. However, the experiments to date have yielded conflicting results with some studies linking whitlockite to malignancy [19,21,22], and others associating whitlockite more frequently with benign processes [24].

Typically, whitlockite can be identified using Raman spectroscopy due to unique spectral features (red-shifted phosphate peak from 960 cm^{-1} to 970 cm^{-1}) [108]. Our hyperspectral data sets were screened for additional mineral species and whitlockite was identified only in fibroadenoma cases. Figure 3.9A demonstrates representative spectra for CHAP, HAP, FA associated calcifications composed of CHAP/HAP, and whitlockite. The spectrum of whitlockite demonstrates a red-shift as shown before [108]. Figure 3.9B shows a spatial distribution of whitlockite relative to dominant species of CHAP/HAP in a representative FA case. As expected, whitlockite is not a prominent species, which is in agreement with previously published estimates of 2% or less for whitlockite identified in calcifications [83].

Provided the spectral differences in CHAP/HAP and whitlockite, it is expected that the calculated carbonate content % for pixels attributed to whitlockite is likely to introduce a slight error if not excluded. Without considering the presence of whitlockite, the average carbonate content is 2.35% for Figure 3.9C. When considering the presence of whitlockite (by removing any pixels contributed by whitlockite), the average carbonate content is 2.38%. This suggests an error of less than 2% if we fail to include whitlockite. For most other cases, this error is even less due to lower content of whitlockite.

Figure 3.9D shows CH image in combination with SHG data to demonstrate collagen presence in both stroma and calcifications themselves. Although it is not clear why different studies disagree on what cases have whitlockite frequently associated with, it is possible that

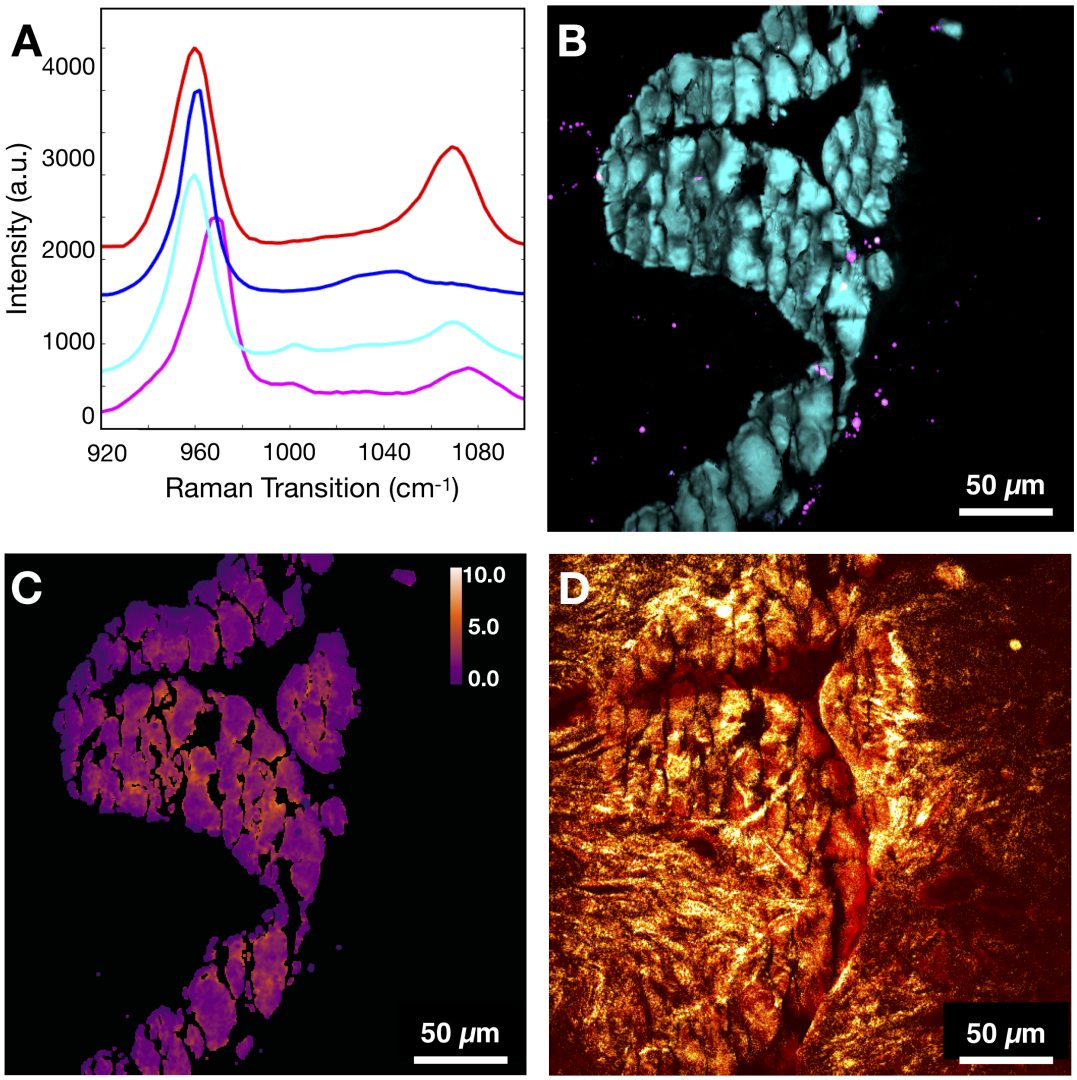

Figure 3.9: Evaluation of whitlockite contribution to dominant mineral species HAP/CHAP. A) Spectral differences of CHAP (red), HAP (blue), FA associated CHAP/HAP (cyan), and whitlockite (magenta). B) Depiction of spatial distribution of HAP/CHAP highlighted using phosphate (cyan) and whitlockite highlighted using red-shifted phosphate (magenta). C) Carbonate content map for the same FOV. D) Calcification underlying organic matrix and stroma depicted using CH Raman transition (red), and SHG (gold).

the underlying matrix does matter when considering what fragments of calcifications make it through tissue processing, paraffin embedding, and microtome cutting. To fully determine the contribution of whitlockite in microcalcifications and its diagnostic utility, imaging of fresh unprocessed tissue is needed.

3.6 Summary and Outlook

Breast calcifications are used to guide patient biopsy prior to resection. However, morphologic assessment of calcifications in mammograms provides limited diagnostic information. Spectroscopic techniques such as spontaneous RS have shown promise for in vivo breast cancer screening in conjunction with mammography. However, to date, detailed spatial and microenvironmental distribution of calcifications in carcinogenesis is poorly understood. Here, we report the first quantitative high-resolution SRS imaging of calcifications, and their association with nearby tissue matrix as well as visualization of calcified organic matrix components with SHG. We developed a simple method to quantify the carbonate content of hydroxyapatite, the main calcification species associated with cancer, based on the ratio of carbonate to phosphate Raman peak. Applying this method to a diverse set of breast calcifications associated with a range of neoplastic processes, we revealed that the microenvironment of the neoplastic processes strongly influences the local distribution of carbonate content. In particular, we observed that carbonate content decreases near the edges of the calcifications closest to neoplastic cells, which may reflect acidified microenvironment as malignant cells proliferate. Using the average carbonate content alone, we achieved a sensitivity of 85% and specificity of 88% in distinguishing benign and neoplastic cases. We expect that the spatial distribution of carbonate content can further improve the sensitivity and specificity in diagnosis. However, in sectioned tissue, the carbonate content pattern is disturbed due to sectioning artifacts (shattering of calcifications and spatial translocation). This problem can be addressed in future studies by imaging either fixed tissue or fresh tissue, where calcifications remain intact.

Besides carbonate content of calcifications, we have elucidated the unique features that distinguish chemical composition of calcifications between FA and IDC. For the first time, we demonstrate that SHG data confirms collagen in FA makes an organic matrix upon which hydroxyapatite accumulates. This matrix observed in FA calcifications is one of the main differences between FA and IDC. This collagen matrix enables robust differentiation of FA and IDC, which exhibit similar carbonate content.

In conclusion, we imaged a diverse set of breast calcifications associated with benign processes, and a range of neoplastic processes including FA, ADH, DCIS and IDC. Our findings support previous reports of carbonate content decreasing on average with increasing malignant potential. Importantly, we showed that a detailed spatial map of calcifications and their complex underlying organic matrix is highly correlated with underlying neoplastic processes and could potentially be used for breast cancer diagnosis. Additionally, the spatial heterogeneity of carbonate content could potentially be a diagnostic indicator of malignancy. Calcification underlying organic matrix, visualized using SHG in conjunction with SRS, assisted in the diagnostic differentiation of patient lesions. Our study suggests that SRS imaging of calcification can be used as an important tool for breast cancer diagnosis. The diagnosis capability will be significantly improved when combined with stimulated Raman histology (SRH), a technique that has already been shown to provide H&E equivalent information in unsectioned tissue [39, 92]. Importantly, unsectioned tissue, either fixed or fresh, provides comprehensive information on the 3D structure and composition of calcifications, which could provide additional quantitative calcification metrics (size, shape, and chemical distribution) for diagnosis. Coupling calcification and SRH imaging with SHG imaging of collagen matrix, we believe that our comprehensive approach holds tremendous potential in improving the complicated diagnostic process for breast cancer and minimizing inter-pathologist discordance. These advances will ultimately ensure the correct diagnosis and the most effective treatment for the patient.

3.7 Supplementary Material

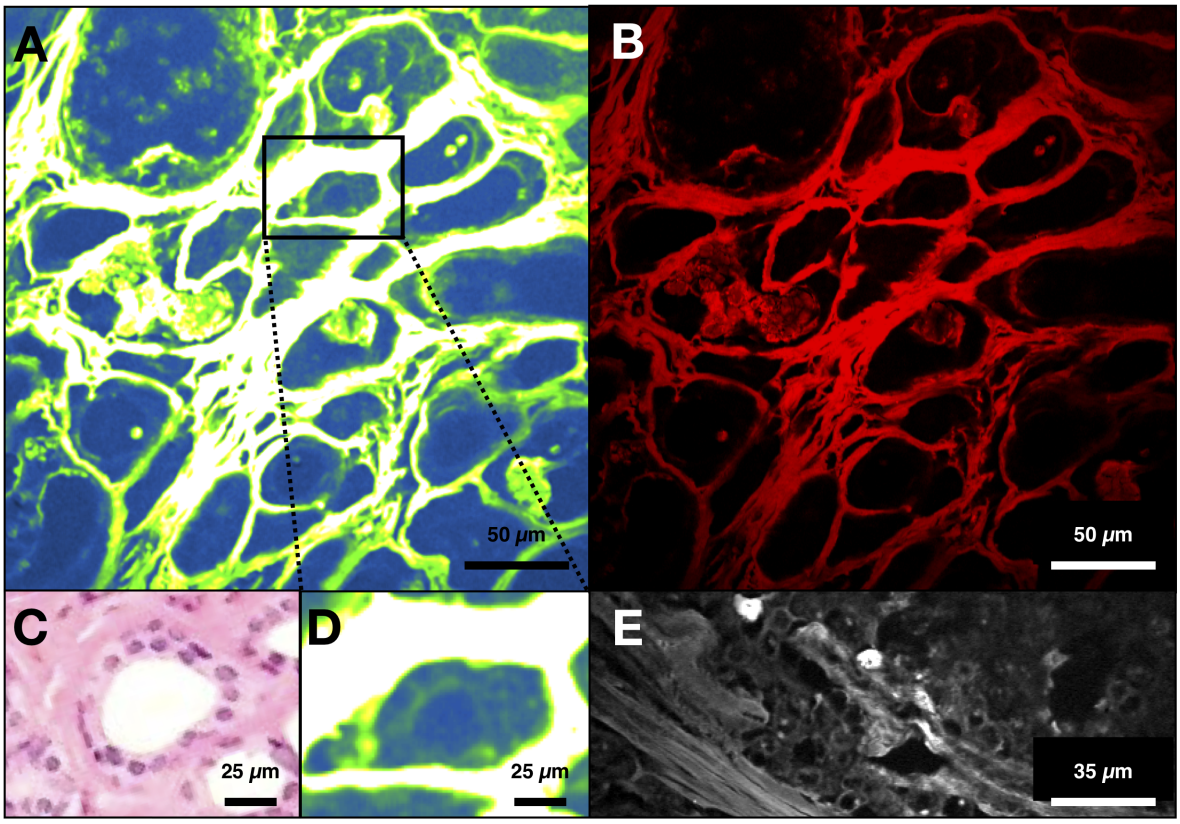

Figure 3.10: Visualizing cellular material in presence of strong CH signal from stromal collagen. A) Adenosis case presented in Figure 3 of main manuscript with adjusted intensity and color scale to assist with visualizing cellular material. B) Adenosis case as presented in Figure 3 of main manuscript. C) A close up of a duct on H&E. D) A close up of a duct from image in A). E) Additional example with easier to visualize cellular material (DCIS case).

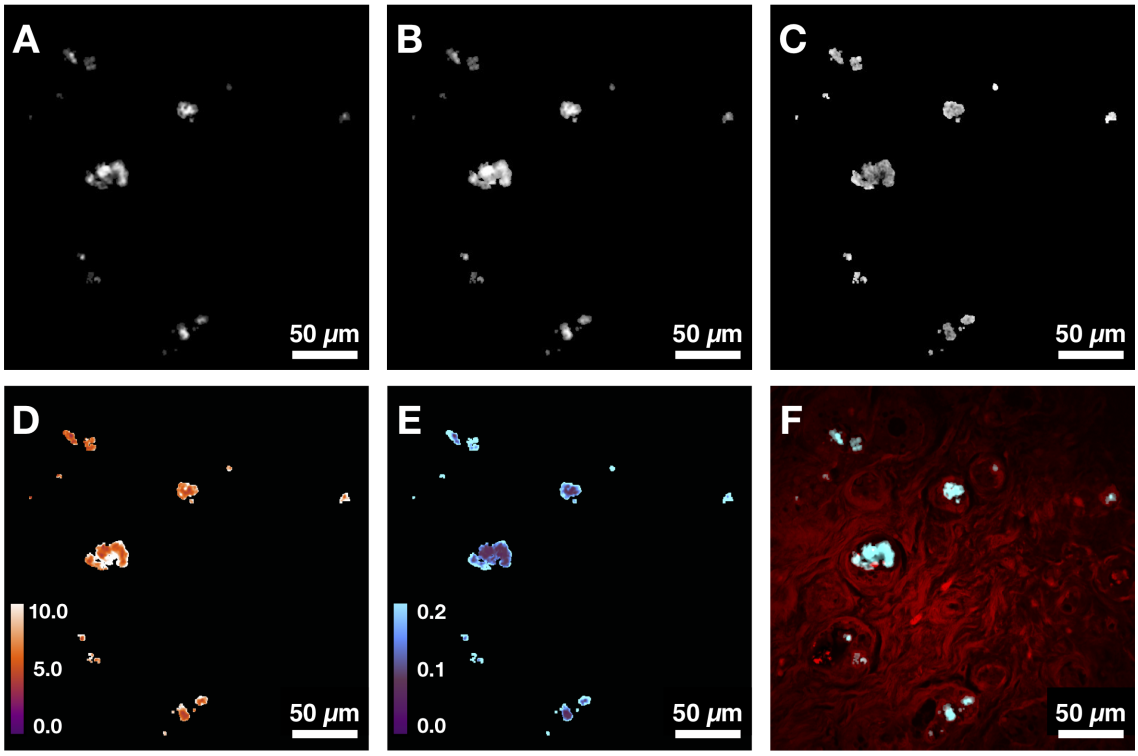

Figure 3.11: Correlating images at phosphate, carbonate, and phenylalanine Raman transitions to resulting carbonate content % and phenylalanine to phosphate ratio maps (calcifications associated with benign process). A) Image at phosphate Raman transition ($\sim$ 960 cm^{-1}). B) Image at carbonate Raman transition ($\sim$ 1070 cm^{-1}). C) Image at phenylalanine Raman transition ($\sim$ 1005 cm^{-1}). D) Carbonate content % map. E) Phenylalanine to phosphate ratio map. F) Image at CH Raman transition (red) together with image at phosphate Raman transition (cyan) to highlight calcification presence in tissue.

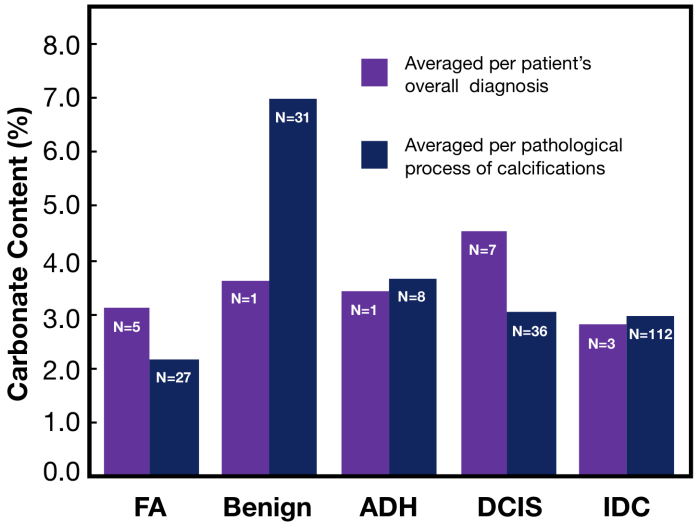

Figure 3.12: Comparing the averages for carbonate content % as calculated per patient's overall diagnosis versus per pathological process of calcifications.

Patient	Sex	Age	Specimen type	Overall diagnosis	Number of calcifications associated with specified pathology					Total number of calcifications per patient	Carbonate content % per patient
					Benign	ADH	DCIS	IDC	FA		
1	F	75	Excisional biopsy	FA	0	0	0	0	9	**9**	2.3±1.1
2	F	64	Needle core biopsy	FA	0	0	0	0	11	**11**	2.4±0.8
3	F	49	Needle core biopsy	DCIS	0	0	8	0	0	**8**	4.4±1.8
4	F	56	Needle core biopsy	DCIS	0	0	1	0	0	**1**	3.5
5	F	57	Needle core biopsy	DCIS	0	0	4	0	0	**4**	3.5±0.5
6	F	58	Excision	ADH	0	3	0	0	0	**3**	3.4±0.5
7	F	51	Excision	DCIS	0	3	0	0	0	**3**	3.9±0.3
8	F	60	Needle core biopsy	DCIS	3	0	0	0	0	**3**	7.7±0.3
9	F	40	Needle core biopsy	DCIS	1	2	0	0	0	**3**	5.7±3.9
10	F	59	Needle core biopsy	FA	0	0	0	0	4	**4**	1.6±0.6
11	F	57	Needle core biopsy	FA	18	0	0	0	0	**18**	6.4±1.6
12	F	51	Excision	Adenosis	7	0	0	0	0	**7**	3.6±0.8
13	F	60	Needle core biopsy	DCIS	2	0	19	0	0	**21**	3.8±1.2
14	F	56	Unilateral mastectomy	IDC	0	0	1	76	0	**77**	2.3±0.7
15	F	68	Lumpectomy	IDC	0	0	0	11	0	**11**	3.6±1.1
16	F	56	Unilateral mastectomy	IDC	0	0	3	25	0	**28**	2.5±0.8
17	F	32	Lumpectomy	FA	0	0	0	0	3	**3**	2.9±0.8
Total number of calcifications per each category					**31**	**8**	**36**	**112**	**27**		

Table 3.1: A patient clinical history summary together with detailed account of calcification number in each category. Carbonate content % average for each patient is provided.

Chapter 4

NON-DESTRUCTIVE CHEMICAL IMAGING OF BONE TISSUE FOR INTRAOPERATIVE AND DIAGNOSTIC APPLICATIONS

4.1 Preface

The efforts described in Chapters 2 and 3 provided the basis for the work presented in this chapter. An unappreciated advantage nonlinear optical techniques offers to anatomic pathology is capturing imaging in bone. As I will discuss further, sectioning of bone samples is not simple and being able to interrogate them without sectioning has immense potential. The work presented here is the foundation for what has the potential to be a burgeoning field of research. Bone is a fascinating system that is complex, dynamic, and fundamental to the human body.

In the process of this project, I have to express my gratitude to Dr. Eleanor Chen who supported this research by dedicating her time and resources. I learned a lot from Dr. Eleanor Chen. Additionally, I truly appreciate the effort and diligence of Brian Johnson and Nora May with Southlake Histology who worked on processing the imaged specimens. I have to credit them for an appreciation of histologists' contribution and the challenges faced on an everyday basis. Also, Marlie Reinmuth, Piper Driskell, and Sarah Bowell with Northwest Biotrust who were instrumental in specimen procurement.

The manuscript related to this work is in preparation and will be submitted shortly.

4.2 Abstract

Bone is difficult to process and image using traditional histopathological methods. Such difficulty leads to challenges in intraoperative consultation during procedures involving bone, specifically in the field of orthopedic oncology. Current approaches require bony tissue to be

sliced into thin histological sections, which is often impractical due to mineralization. However, providing intraoperative pathological information is critical to guide surgical treatment. In this study, we demonstrate that a multimodal imaging approach that combines stimulated Raman scattering (SRS) microscopy, two-photon fluorescence (TPF) microscopy, and second harmonic generation (SHG) microscopy can provide useful diagnostic information regarding intact bone tissue fragments from surgical excision or biopsy specimens. We imaged bone samples from 14 patient cases and performed comprehensive chemical and morphological analyses of both mineral and organic components of bone. Our main findings show that low carbonate content is indicative of new bone formation, which appears to be particularly prominent in neoplastic bone formation. Additionally, we conducted a morphometric analysis of bone organic matrix and determined that in addition to carbonate content, lacunae aspect ratio, angle of collagen relative to lacunae major axes, and collagen anisotropy are useful in distinguishing between normal bone growth and growth that occurs under abnormal conditions. Using a Random Forest classification method, we tested the diagnostic utility of our multimodal imaging and achieved an overall accuracy of 92% for separating several important pathological conditions. Our results demonstrate that multimodal imaging and machine learning-based analysis of bony tissue can potentially enable pathologists to provide crucial information to surgeons, especially in the field of orthopedic oncology.

4.3 Introduction

Intraoperative consultation of bone specimens plays an important role in orthopedic surgery. One of the main reasons for intraoperative consultation on a bone specimen is to determine whether an intra-osseous lesion is benign or malignant [109, 110]. In the case of a malignant lesion, separating primary bone cancer from metastasis becomes another challenge. An accurate intraoperative diagnosis guides subsequent clinical decisions on operative procedures and clinical management.

Current intraoperative pathology consultations rely heavily on gross examination, cy-

tologic preparations, and frozen sections. While these approaches work well for many organ systems, bone samples have proved to be challenging due to their mineralized content. De-mineralization protocols for bone specimens can take up to one week, rendering sectioning-dependent techniques unusable for an intraoperative setting. Additionally, the de-mineralization procedure destroys the DNA/RNA necessary for clinical molecular tests and compromises the histologic quality of tissue sections, making definitive pathologic diagnosis difficult. Although soft tissue and relevant cellular materials can sometimes supplement and guide medical treatment of musculoskeletal lesions [111, 112], they are often insufficient for making clinical decisions. Without the ability to interrogate bone tissue intraoperatively, the patient must wait for post-surgical tissue processing and possibly undergo additional procedures based on pending pathology diagnosis. Thus, there is an unmet need to develop tools capable of providing intraoperative diagnosis of bone specimens to better inform surgeons as they decide on surgical treatment.

Bone is an important specialized connective tissue composed of mineralized extracellular material (primarily type I collagen). The mineral content of bone consists mainly of hydroxyapatite [$Ca_{10}(PO_4)_6(OH)_2$], with variable amounts of carbonate and magnesium [108]. Conventional light microscopy relies on H&E staining for morphology and various special stains (e.g., Masson's trichrome and von Kossa) to visualize collagen and mineralization. Special stains require time-consuming processing procedures, which is why such approaches are only used for permanent processing of specimens after surgery.

Traditional histological techniques are inadequate to study bone specimens and visualize the internal structures. Although several ultrastructure-geared techniques provide a wealth of information about bone, they are also not suitable for intraoperative diagnosis due to the time constraints in a clinical workflow. For example, the scanning electron microscope offers high spatial resolution ($<$1 nm) along with a large depth of field and a wide field of view [113], but involves time-consuming sample preparation [114]. Similarly, small-angle x-ray scattering microscopy has been used to study bone nanostructure and its role in healing and other functions [115, 116, 117]. However, this technique also requires time consuming and

destructive sample preparation.

Optical techniques such as second harmonic generation (SHG) microscopy [117], third harmonic generation (THG) microscopy [118], Fourier-transform infrared spectroscopy (FTIR) [119], and Raman spectroscopy [120, 121, 122, 123, 124] allow for noninvasive qualitative and quantitative evaluation of bone specimens. These techniques have been used to study mostly non-neoplastic processes of bone including healing, aging, osteoporosis, and osteomyelitis [122, 125, 126, 127, 128, 129]. A few reports have probed chemical changes of mineral components occurring in a very limited collection of cancers [130, 131]. Nonetheless, our understanding of chemical changes in bone related to neoplastic processes such as osteosarcoma and chondrosarcoma remains limited. Moreover, there has been no attempt to explore chemical changes for assessing pathological conditions of bone specifically for intraoperative applications.

SRS, a powerful label-free technique capable of providing chemical information at submicron spatial resolution [88, 20, 61], has shown tremendous promise for label-free histopathology applications. It works by exploiting lipid and protein Raman contrasts to generate H&E equivalent images and is called Stimulated Raman histology (SRH) [61, 39]. Applications of SRH to intraoperative diagnosis of brain tumors [39, 92, 132] and diagnosis of endoscopically obtained biopsy tissue from gastrointestinal tract [41] demonstrate the promise of SRH as an alternative to H&E. However, the lack of contrast between bone matrix and typical cellular structures within bone makes it challenging to translate SRH to bone imaging. More recently, we have shown that SRS imaging of chemical changes of mineral content of calcified breast tissue can also provide critical diagnostic information [133]. In particular, lower carbonate levels of calcifications are strongly correlated with malignancy. We hypothesize that the chemical changes of bone composition are also reflective of underlying pathology, and SRS could potentially be used for intraoperative diagnosis of bone cancer.

This study aims to demonstrate the diagnostic utility of a multimodal approach to visualizing and analyzing the structure and chemical compositions of various bone specimens using stimulated Raman scattering (SRS) microscopy combined with two-photon fluores-

cence (TPF) and SHG. We used SRS to visualize whole intact bone specimens containing both organic and mineralized components at high spatial resolution and chemical specificity. Because no processing of surgical specimens is needed, we were able to produce an unprecedented level of detail about bone in association with pathologies frequently encountered in intraoperative settings. A simple staining procedure and robust TPF process allowed us to highlight nuclear details to assist pathologists in extracting the most diagnostic information. In addition, we acquired SHG to evaluate collagen organization [22] as an additional metric of bone response in physiological and pathological circumstances. Because SRS, TPF, and SHG share the same laser source and microscope, they can be acquired simultaneously, which greatly simplifies the imaging workflow and reduces imaging time. Our results show that chemical and morphological features obtained from the multimodal imaging method can distinguish specific categories of bone cancer with >90% accuracy and provide critical information needed for intraoperative consultation. Because our non-destructive imaging approach does not interfere with downstream histological and molecular analysis, it has the potential to fulfill a much-needed role in intraoperative diagnosis for orthopedic oncology.

4.4 Experimental Methods

4.4.1 Multimodal imaging with SRS, TPF, and SHG

The details for the broadband SRS set up were outlined in a previous publication [55]. Briefly, we used broadband femtosecond dual-beam laser system (Insight DS+ from Spectra-Physics) where a tunable beam (pump) was centered at 798 nm for CH Raman region and 944 nm for fingerprint Raman region and a fixed beam (Stokes) was centered at 1040 nm. A home-built laser scanning microscope equipped with a 25× Olympus water immersion objective (NA=1.05) was used to image the sample. The SRS signal detected in epi mode with a large area silicon photodiode, while epi-fluorescence from TPF and SHG are detected simultaneously by a photo-multiplier tube (Hamamatsu H10770PA-40). At the focus, the pump and Stokes beams had an average power of 50 mW each. For SRS imaging, a stack

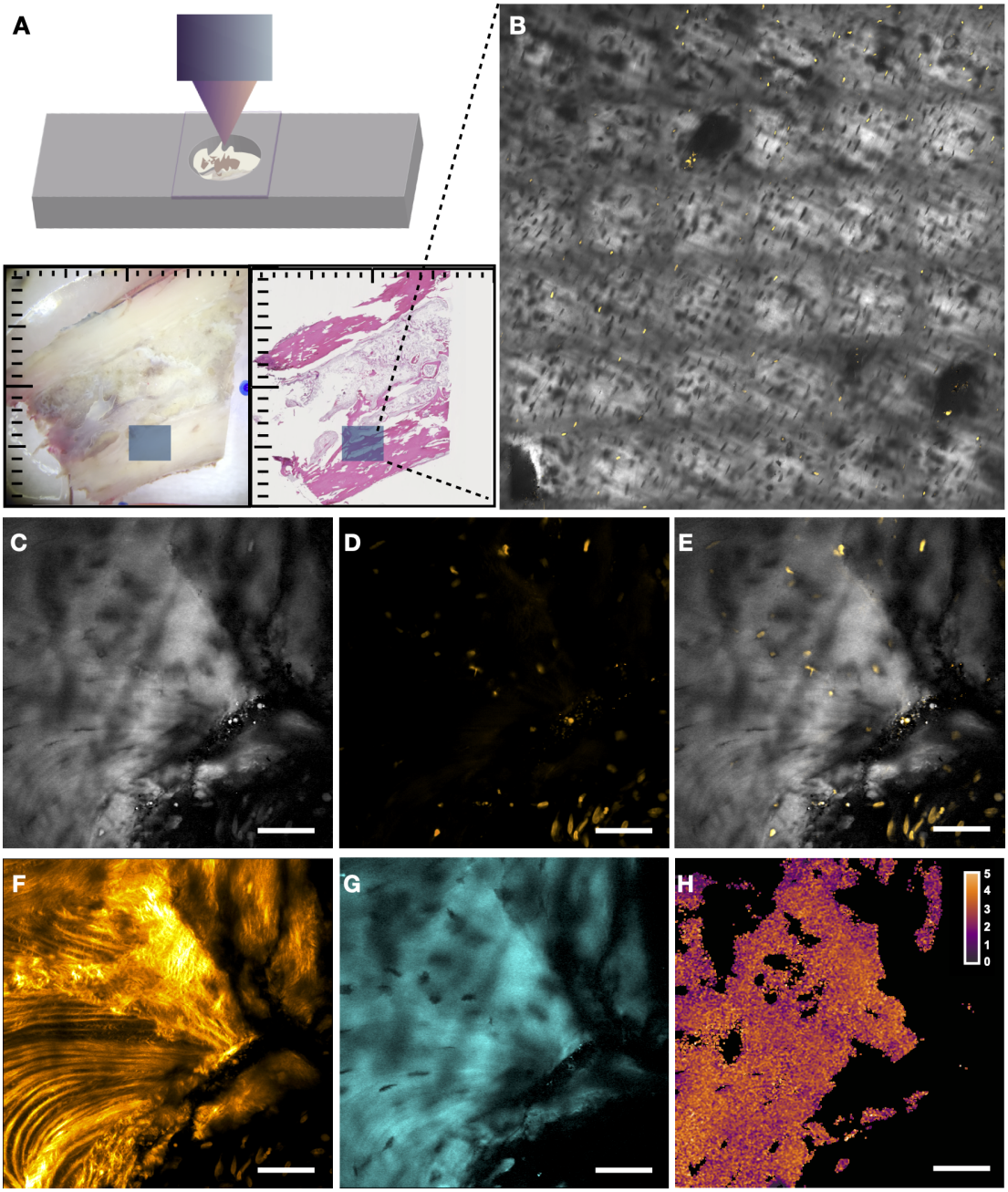

Figure 4.1: Workflow for bone tissue imaging and image processing. A) Graphical representation of a bone sample embedded in agar gel and sample holder. Gross image (left) in addition to post-imaging histology (right) are included. B) An area to visualize bone microenvironment provides overview of tissue from where subareas are selected for more detailed study using hyperspectral microscopy. Scale bar is 250 μm. C-E) Images obtained from SRS at ~2930 cm^{-1} (grey), TPF from AO stained nuclei (gold), and combination of both respectively. F) SHG image obtained to highlight collagen organization. G) SRS image at 960 cm^{-1} to highlight mineral content (cyan). H) Carbonate content % map generated using fingerprint information from SRS (see Methods section). C-H scale bar is 50 μm.

of frames with single field of view (FOV) of 285 μm $\times$ 285 μm (512 pixels $\times$ 512 pixels) was acquired, for which the pixel dwell time is 8 μs and time to acquire each frame is 2 s. The frames are acquired every 2 cm^{-1} for total of 90 frames on average. For SHG and TPF imaging a bandpass filter (520 nm $\pm$ 20 nm) was used.

Bone specimen is placed into an aluminum sample holder covered with glass coverslip (see Figure 4.1A, top image). The tissue was photographed to map imaged areas. For each sample, an area of $\sim$2 $\times$ 2 mm at the bone-soft tissue border was imaged with SRS at $\sim$2930 cm^{-1} corresponding to protein vibrational peak and TPF from acridine orange stained tissue. Detailed SRS data was collected in both CH and fingerprint Raman regions as hyperspectral stacks in selected regions of interest (ROI). Additionally, single frames of CH ($\sim$2930 cm^{-1}), TPF (tissue was stained by acridine orange), and SHG were obtained as single frames (see Figures 4.1C-F). The SRS CH data was used to determine lipid and protein components in studied tissues. The SRS fingerprint data was used to determine mineralization species present in our samples.

4.4.2 Bone tissue specimens

Bone tissue samples was obtained from 19 patient cases with IRB approval from the University of Washington. The cases were de-identified and curated by Northwest Biotrust biorepository, Seattle, WA. The case selection was based on the pathology report to include normal (rib, mandible, femoral head), non-neoplastic pathology (avascular necrosis, fracture, hypertrophic bone), primary neoplastic (osteosarcoma and chondrosarcoma), and secondary neoplastic (metastatic cancer to bone). The bone tissue was cut into 2-4 mm sections with a band saw and fixed in 10% neutrally buffered formalin.

4.4.3 Tissue staining

Before imaging, bone tissue was stained with acridine orange (5 μg/mL as dissolved in Dulbecco's phosphate buffered saline). The bone tissue was stained for ∼10 min and thoroughly washed in phosphate buffered saline before imaging.

4.4.4 Agar gel preparation

For imaging, bone tissue was imbedded into agar gel to immobilize the specimen. Agar gel (15 mg agarose/mL) was prepared by mixing 125 mmol/L NaCl, 10 mmol/L glucose, 10 mmol/L HEPES, 3.1 mmol/L CaCl2, and 1.3 mmol/L $MgCl_2$ with agar (Sigma Aldrich) [134]. The mixture was heated to 60 °C to liquify the gel for the embedding procedure.

4.4.5 Sample mapping

Gross photographs were obtained of each specimen. Before imaging each sample, the sample stage position was recorded to determine the dimensions of sample and positions of main lesional area and subareas for imaging. Additionally, the depth of images was measured relative to the cover slip surface. The recorded locations of imaged tissue within the sample was correlated with histology after the experiment to confirm diagnosis and establish microenvironment for imaged bone.

4.4.6 Calibration of SRS imaging to determine carbonate content of bone mineral content

Chemical imaging and carbonate content determination was previously described [133]. Briefly, calcium hydroxyapatite (HAP) and 10% carbonated hydroxyapatite (CHAP) were obtained from Sigma-Aldrich and Clarkson Chromatography Products respectively. Grounded powders were mixed and prepared for calibration purposes (0%, 2.5%, 5.0%, 7.5%, 10% car-

bonate content). To determine carbonate content in bone samples (Figure 4.1H), we used ratiometric SRS images at ($\sim$ 1070 cm^{-1}) and ($\sim$ 960 cm^{-1}) [133].

4.4.7 Morphometric analysis of organic bone matrix

Using a combination of manual selection and interactive machine learning and segmentation toolkit, Ilastik [135], the osteocyte lacunae were segmented and stored as individual regions of interest (ROIs). Using Particle Analyze in ImageJ, the lacunae aspect ratio, area, and angle of major axis relative to horizontal were determined. Collagen organization was interrogated through SHG images. Using ImageJ FibrilTool [136] and in-house algorithms written in Matlab and ImageJ, we determined the angle of lacunae relative to collagen as well as local anisotropy. To generate a map, a sliding box (64 $\times$ 64 pixels) with sampling every 8 pixels was used. Using the ROI manager in ImageJ, angle and anisotropy data were determined for each individual lacuna.

4.4.8 Statistical analysis

Using the parameters (aspect ratio, lacunae area, anisotropy, and angle) from the morphometric analysis and the carbonate content % obtained from SRS fingerprint data, a Random Forest classification model was generated. Specifically, we employed the TreeBagger algorithm in Matlab. We used 70% of original data for training and the remaining 30% used for testing the final accuracy.

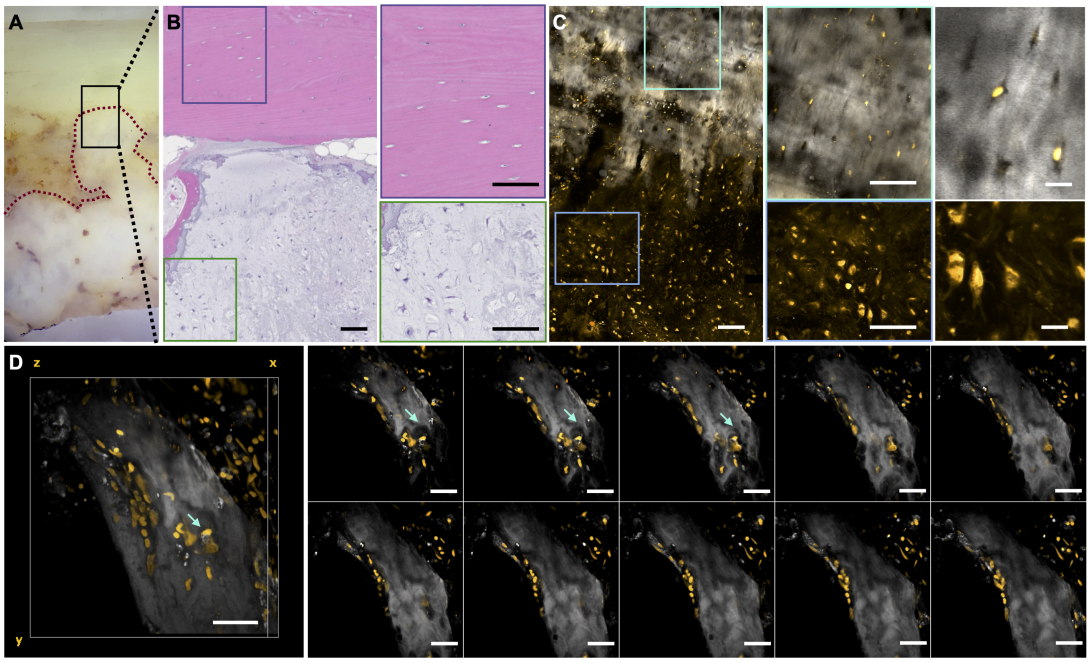

Figure 4.2: : Imaging morphology of bone specimen. A, B) Gross image of bone adjacent to chondrosarcoma focus with corresponding H&E. Scale bars are 70 μm. C) SRS/TPF imaging of the same geographical area (greys - SRS at $\sim$2930 cm^{-1} and gold - TPF from AO stained nuclei). Scale bars are 70 μm for larger view and two close ups (in blue and cyan). Scale bar is 20 μm for cellular features close up. D) 3D stack of bone remodeled by osteoclasts as indicated by cyan arrows (thickness of 150 μm).

4.5 Results and Discussion

4.5.1 Imaging morphological and architectural features of bone specimen with SRS and TPF

One of the most useful diagnostic features of H&E is the morphology and architecture of cellular organization. For traditional H&E to work, bone must be demineralized and thinly sectioned. SRH does not require tissue processing. However, the same protein and lipid contrasts used in SRH for visualizing soft tissue do not generate sufficient contrasts for bone tissue. An additional challenge is that unsectioned bone tissue is highly scattering. It requires imaging in the epi-mode, instead of transmission mode which is employed in most SRH applications to date.

Here we demonstrate that using SRS imaging at ∼2930 cm^{-1} (a CH vibrational mode predominantly for protein) and TPF of acridine orange we can visualize the morphology of bone and cellular structures within and nearby. Together SRS and TPF provide a simulacrum of the typical H&E, highlighting histologic features of bone tissue including cell type, stroma and matrix at high resolution. Both imaging modalities are implemented in the epi-mode, which is amenable to surgical tissue of any size and shape without additional processing.

Pathological bone tissues exhibit distinct morphological features. Chondrosarcoma is a malignant cartilage forming tumor that is the 3rd most common bone malignancy and is presumed to arise from the chondrocyte lineage of mesenchymal cells [137]. Our case of chondrosarcoma shows the characteristic gross appearance of white-gray lobules of a neoplasm with cartilaginous matrix (Figure 4.2A, below the red dashed line) invading bone (Figure 4.2A, above the red dashed line). Corresponding H&E (Figure 4.2B) confirms the presence of polygonal to spindled neoplastic cells in a loose cartilaginous matrix invading adjacent cortical and medullary bone. The combination of SRS and TPF images are consistent with H&E clearly showing neoplastic cells in a cartilaginous matrix adjacent to the bone (Figure 4.2C). Our findings demonstrate that the integration of SRS/TPF imaging modalities allow

for the visualization of cellular structures of neoplasm in bone specimens with high resolution, which correlates well with the histologic features seen in conventional H&E staining.

In addition to being able to image a thick tissue specimen, SRS/TPF has an intrinsic capability to provide 3D information. This can overcome one of the drawbacks of conventional histology, where the information is mostly confined to the 2D plane. If a pathologist encounters a diagnostically challenging scenario where additional H&E sections can be beneficial, it is likely to take at least 24 hours to produce additional sections for evaluation if warranted during pathological examination. In addition to the time expense, demineralizing before processing destroys tissue that might become necessary for molecular diagnostic analysis, which is frequently warranted to render a complete diagnosis. Being able to quickly review the architecture of tissue without compromising subsequent molecular studies and without excessive time involvement is paramount in the general pathology workflow and especially in an intraoperative setting.

The bone and its microenvironment are composed of various cell types. Our 3D reconstruction demonstrates the presence of osteoblasts, the cell type responsible for bone formation, lining the bone trabeculae (Figure 4.2D, indicated by a cyan arrow). With additional optical sectioning, we observe cells within cavities, known as resorption pits. This morphology is consistent with osteoclasts.

Overall, we show that SRS and TPF provide diagnostically useful morphological and architectural information that can assist a pathologist's evaluation of bone specimens intraoperatively. The intrinsic optical sectioning of SRS and TPF enables 3D assessments of specimens when desired.

4.5.2 SRS based chemical imaging provides diagnostically relevant information about the mineral content

In current pathology practice, one of the most underutilized diagnostic components of bone tissue is mineral content. Several publications suggest that the mineral component of bone is

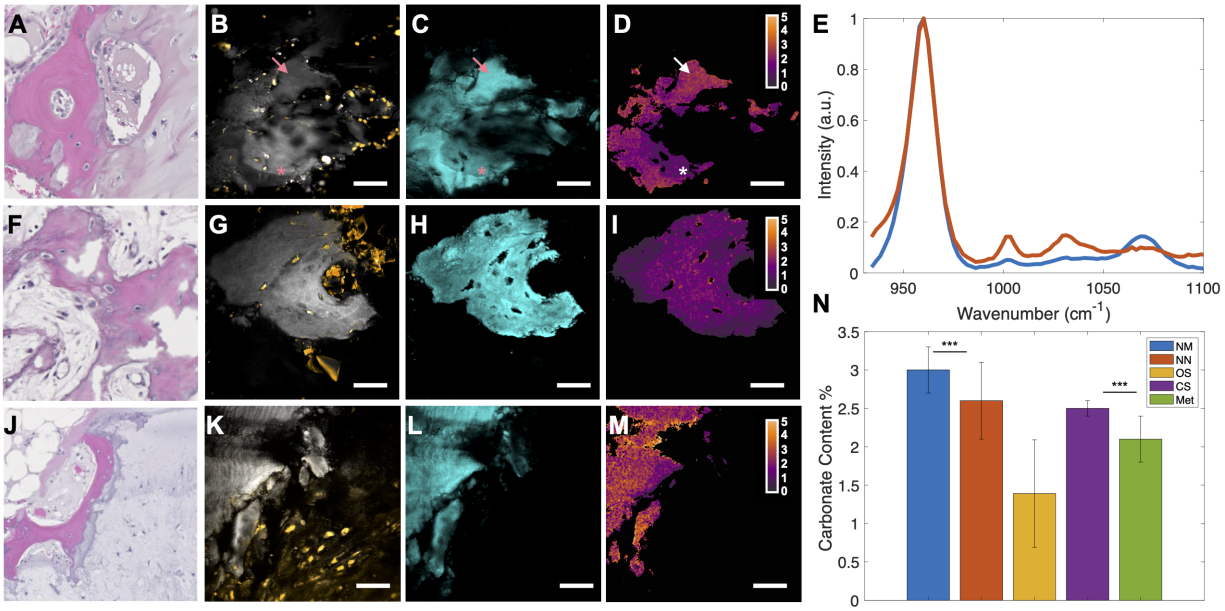

Figure 4.3: Chemical imaging of mineral bone component. A) H&E of bone healing after avascular necrosis with endochondral ossification focus shown here. B-D) Representative area showing new bone formation (greys –SRS at $\sim$ 2930 cm^{-1}, gold –TPF from AO stained nuclei collagen, cyan –SRS at $\sim$ 960 cm^{-1}, and SRS derived carbonate content map). Pink/white arrow corresponds to the mature bone. Pink/white star corresponds to osteoid. E) Spectra of two different areas identified in D). White arrow corresponds to the spectrum in blue. White star corresponds to spectrum in blue. F) H&E of osteosarcoma case with the residual neoplastic bone matrix. G-I) Representative area showing neoplastic bone matrix (greys –SRS at $\sim$ 2930 cm^{-1}, gold –TPF from AO stained nuclei collagen, cyan –SRS at $\sim$ 960 cm^{-1}, and SRS derived carbonate content map). J) H&E of bone involved by chondrosarcoma. K-M) Representative area showing bone adjacent to neoplastic cells (greys –SRS at $\sim$ 2930 cm^{-1}, gold –TPF from AO stained nuclei collagen, cyan –SRS at $\sim$ 960 cm^{-1}, and SRS derived carbonate content map). N) Bar chart of carbonate content % across groups imaged in this study (NM –normal bone, NN –non-neoplastic pathological process including bone remodeling, OS –osteosarcoma, CS –chondrosarcoma, Met –metastatic cancer). Two-sided t-test is performed and $***$ –p-value$<$0.001.

altered during cancer development [130, 131, 138]. Here, we explore the diagnostic utility of chemical information provided by SRS in the fingerprint region as we interrogate unprocessed mineralized tissue involved in both non-neoplastic and neoplastic pathologic conditions.

Figures 4.3A-D show an example of non-neoplastic bone sample. This case has a history of avascular necrosis and shows endochondral ossification, which occurs as a part of new bone formation. When imaged with SRS/TPF, multiple foci of newly formed bone were noted. A representative focus of osteoid is shown in Figures 4.3B-D (identified by star). SRS imaging at ~ 960 cm^{-1} (Figure 4.3C) demonstrates gradual mineralization of the newly formed osteoid (identified with pink star) as indicated by increasing intensity of the image while approaching the area of more mature bone (identified with pink arrow). The corresponding carbonate content % map shows a low carbonate content in that area closer to 0 (Figure 4.3 D). The spectra (Figure 4.3E) from two distinct areas of endochondral ossification (indicated with a star and an arrow in Figure 4.3D) show the difference in carbonate/phosphate ratio. Our result is consistent with previous research showing that newly mineralized osteoid consists of predominantly hydroxyapatite [139]. The mineralized content of more mature bone has a higher carbonate content.

In contrast, the analysis of carbon content in a case of osteosarcoma (representative area shown in Figure 4.3F-I) shows that the entire neoplastic bone matrix has low carbonate content. This is likely attributed to the higher acidity of the cancer microenvironment precluding the inclusion of carbonate ions [96]. It has been shown that typically, the carbonate content gradually increases as bone matrix matures [139]. However, in the case of osteosarcoma, we can speculate that higher acidity interrupts the normal process.

For comparison, we show that the bone adjacent to the neoplastic cells in a case of chondrosarcoma mostly retains high carbonate mineral content (representative area in Figures 4.3J-M). Only a slight edge near the neoplastic cells appears to be impacted by the cancer microenvironment displaying lower carbonate content. Chondrosarcoma does not produce osteoid and the impact occurs on mature bone already present. Since mature bone tends to have higher carbonate content, observing only the peripheral impact of carbonate content is

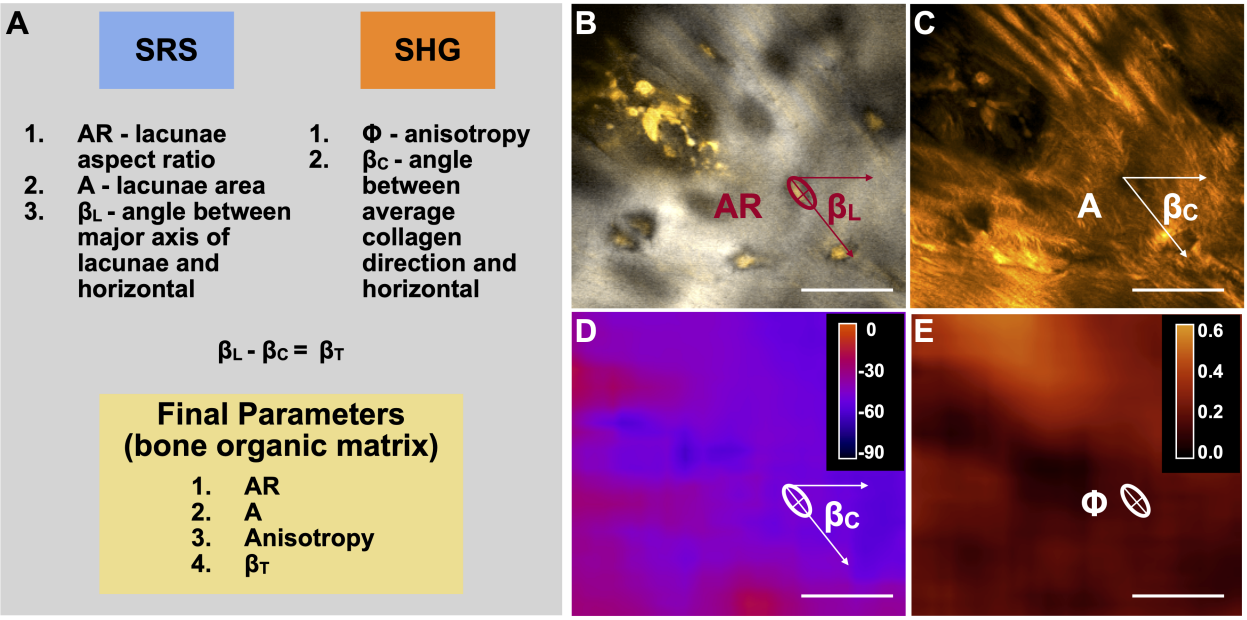

Figure 4.4: Morphometric analysis of organic bone matrix. A) Depiction of parameters used for morphometric analysis. B) Lacunae aspect ratio (AR) and angle for major axis of lacunae with horizontal (β_L) are determined from SRS (2930 cm^{-1}) data. C) Angle of collagen with horizontal (β_C) and collagen anisotropy (A) are determined from SHG using FibrilTool. Parameter β_C is defined as an angle collagen makes with horizontal. D, E) Resulting angle of collagen with horizontal and anisotropy maps used by ImageJ ROI manager to determine β_C and Φ associated with a given lacuna (highlighted with ellipse).

consistent with known behavior of neoplasm.

The carbonate content percentage is compared across all groups of non-neoplastic and neoplastic cases included in this study (Figure 4.3L). The non-neoplastic pathologic conditions are avascular necrosis, abnormal bone hypertrophy, and fracture. The neoplastic samples analyzed are primary bone neoplasms (osteosarcoma and chondrosarcoma) and metastatic cancer to bone. All pathologies show significant difference from the normal. The osteosarcoma cases appear to have the lowest carbonate content relative to normal and other groups.

4.5.3 Organic matrix changes are indicative of pathology

The organic matrix of bone is primarily composed of collagen I and is typically formed by osteoblasts. Newly formed bone matrix, osteoid, lacks mineralization, and when osteoblasts become surrounded by matrix, they differentiate into osteocytes. The lacunae, spaces where osteocytes remain for the duration of their lifetime, vary in shape and size. Lacunae are typically round to almond-shaped and then often become more oblong as they mature [140]. Because bone formation, remodeling, and repair are dynamic processes responsive to the microenvironment, we hypothesize that morphological changes of lacunae and collagen as indicative of underlying pathological processes and can be used for diagnosis.

For the morphometric analysis of osteocyte lacunae, we use SRS and SHG to obtain the parameters of interest for lacunae and collagen, respectively (Figure 4.4A), including lacuna area, aspect ratio (defined as the ratio between the major axis and the minor axis of a lacuna), collagen anisotropy (as determined by FibrilTool [136]), and angle between lacuna and collagen. The lacunae in the SRS image appeared dark and were hand segmented for this purpose (Figure 4.4B, where one lacuna is identified with red ellipse). Although we primarily use hand segmentation here, the automation of such a process is possible using machine learning platforms such as Ilastik [135]. Using particle analysis available in ImageJ, we obtain an aspect ratio of segmented lacunae (AR) as well as the area (A). Additionally, the angle of the lacunae major axis relative to the horizontal (β_L) is determined. We use SHG from collagen to measure matrix organization (Figure 4.4C). Using FibrilTool [136], we determine the average angle of collagen relative to horizontal (β_C) and anisotropy value (Φ) of the collagen fibers. For anisotropy assessment with Φ of 1 representing complete co-alignment and Φ of 0 representing complete lack of co-alignment. To generate a map of β_C and Φ, an in-house algorithm was used to apply FibrilTool to 64 $\times$ 64 pixels^2 regions while scanning across the image (see methods section for additional detail).

A corresponding Φ map is provided in Figure 4.4E. The area of lamellar growth highlighted with SHG corresponds to Φ approaching 0.5 (with Φ ranging from 0-completely

random to 1-completely co-aligned). Being able to quantify differences in anisotropy for lamellar growth versus a basketweave pattern with lower anisotropy has the potential to identify pathological conditions where collagen growth is impaired or significantly different.

We performed morphologic analysis of lacunae and collagen on a normal mandible and a hypertrophic mandible from abnormal development. When comparing the parameters as described, we observe that the difference in the organic matrix between the two cases is significant. Compared to the normal mandible (a representative field of view in Figures 4.5A-C), which shows predominantly colinear collagen as highlighted by SHG (Figure 4.5C), the collagen in the hypertrophic mandible is more disorganized, and lacunae are smaller and rounder (Figures 4.5D-E). Normal bone has a broader distribution of AR values and lacunae sizes compared to hypertrophic bone (Figure 4.5G-H). Normal bone generally has larger osteocyte lacunae (Figure 4.5H). Additionally, the angle between lacunae major axis and nearby collagen average orientation (β_T) is often closer to 0 degrees in the case of normal bone (Figure 4.5I). In contrast, in abnormal bone, the major axis angle with nearby collagen appears to have a broader distribution. The normal bone shows the range of Φ from 0 to 0.5 with median of 0.3 (Figure 4.5J). In contrast, abnormal bone has a higher degree of disorganization reflected in lower anisotropy values with medial of < 0.2.

Applying the same analysis across all samples, we summarized the differences in morphological parameters among different pathological conditions (Figure 4.6). The aspect ratio of lacunae across all pathological categories shows the most differences between normal and non-neoplastic pathology as well as metastatic cancer (see Figure 4.6A). These findings are consistent with visual observations where lacunae in osteoid or newly formed bone appear to have lower aspect ratio relative to mature bone. Moreover, the area of lacunae is variable across all groups with the most significant differences occurring between normal cases and cases that include healing bone and neoplastic bone matrix (see Figure 4.6B).

When evaluating collagen organization, normal bone and bone with metastatic cancer show the largest difference in the angle (β_T) (Figure 4.6C) and anisotropy (Φ) (Figure 4.6D). It is plausible that these parameters are capturing higher bone turnover and subsequent

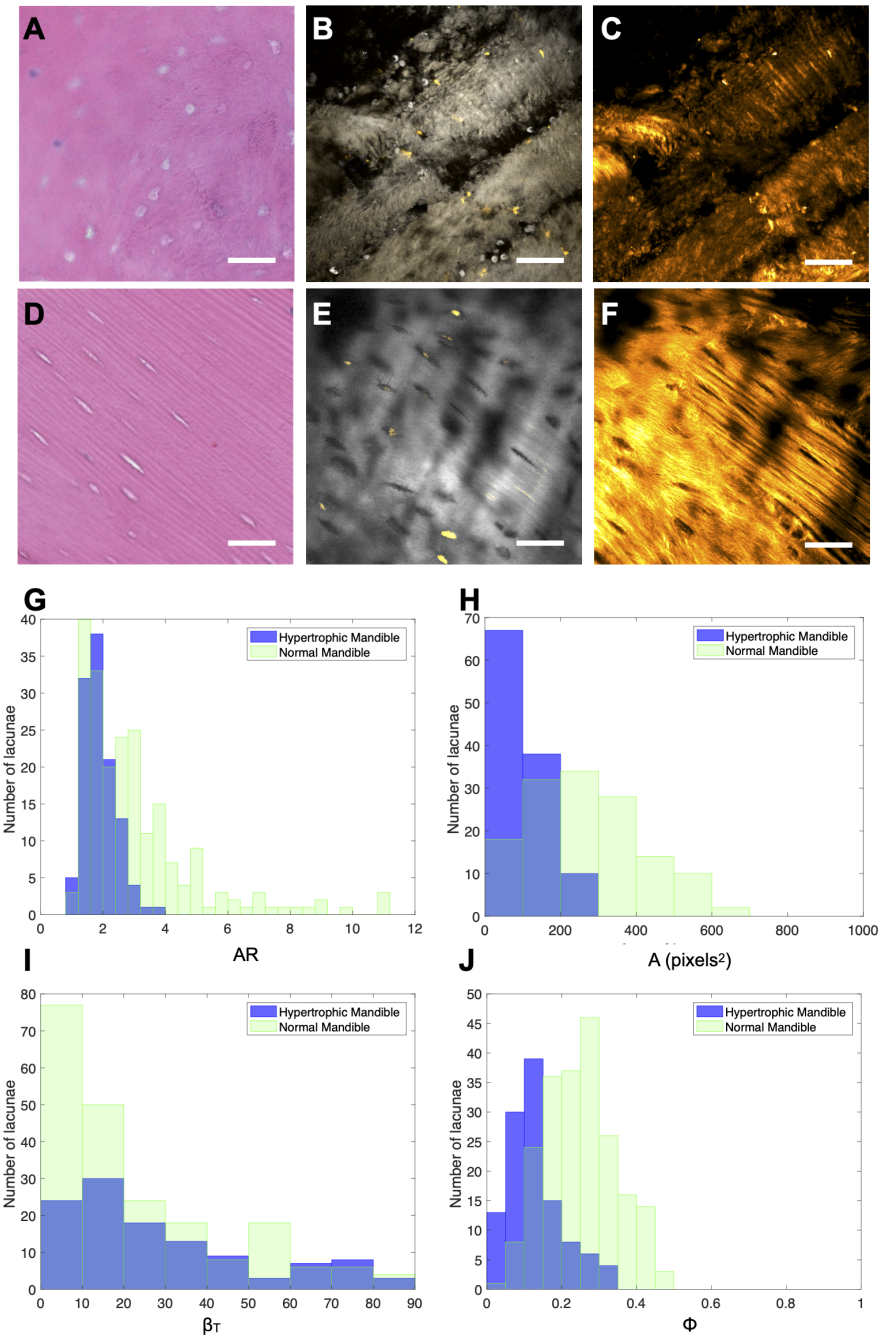

Figure 4.5: Differences in the organic bone matrix as determined by morphometric analysis and supported by histology. A-C) H&E, SRS/TPF, and SHG images of normal bone. D-F) H&E, SRS/TPF and SHG images of hypertrophic bone. G-J) Histograms for aspect ratio of lacunae (AR), lacunae area (A), angle of nearby collagen, and the major axis of lacunae (β_T), and anisotropy as determined by FibrilTool.

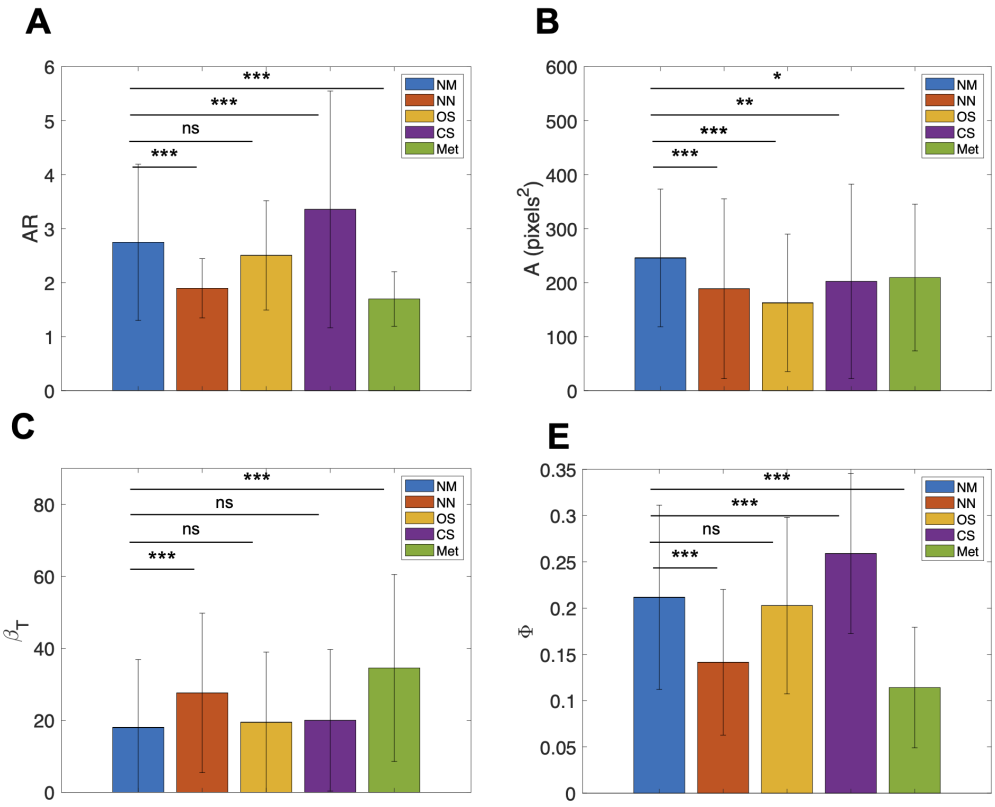

Figure 4.6: Summary of morphometric analysis for bone specimens. A) Bar chart for aspect ratio of lacunae (AR) averages. B) Bar chart for lacunae area (A). C) Bar chart for angle of nearby collagen and major axis of lacunae (β_T). D) Bar chart for anisotropy (Φ). Two-sided t-test is performed and $*$ denotes p-value < 0.05, $**$ –p-value <0.01, and $***$ –p-value<0.001. NM –normal bone, NN –non-neoplastic pathological process including bone remodeling, OS –osteosarcoma, CS –chondrosarcoma, Met –metastatic cancer.

disorganization of the matrix.

Overall, our morphometric analysis of osteocyte lacunae and nearby collagen shows the most differences in non-neoplastic cases that have increased bone remodeling (bone resorption and bone formation) as well as in cases of metastatic bone cancer. Using the organic matrix quality and detectable abnormalities can subsequently be combined with other parameters to potentially improve diagnostic accuracy.

4.5.4 Combined together morphology, organic matrix analysis, and mineral content analysis yields diagnostically useful information

As shown in the previous sections, both mineral components and morphometric analysis of lacuna and collagen matrix provide diagnostically useful information. In an intraoperative setting, it is important to determine if the lesion is benign or malignant and in the case of malignant, further subdivide into primary and secondary. We demonstrate that by combining chemical analysis and morphological analysis enabled by multimodal imaging, we can achieve high accuracy classification of specific bone cancer types. To build a robust classification algorithm with multiple parameters, we employed a supervised machine learning model. The advantage of a machine learning algorithm is that once a model is trained, predictions can be generated in almost real time which can help to guide intraoperative pathological diagnosis and subsequent patient treatment. We utilize a supervised classifier readily available in Matlab which performs a Random Forest classification called TreeBagger. It is a bootstrap-aggregated (bagged) decision tree where multiple decision trees are created using randomized subsets of the data and features from the training set for each tree. The ensemble of trees can then be applied to new data where each tree "votes" on the correct prediction where the final category is determined by the greatest number of votes. By selecting a random subset of predictors for the generation of each tree, the algorithm is able to reduce the effects of overfitting and improves generalization [141].

We combined the data from the morphometric analysis (including aspect ratio, area of la-

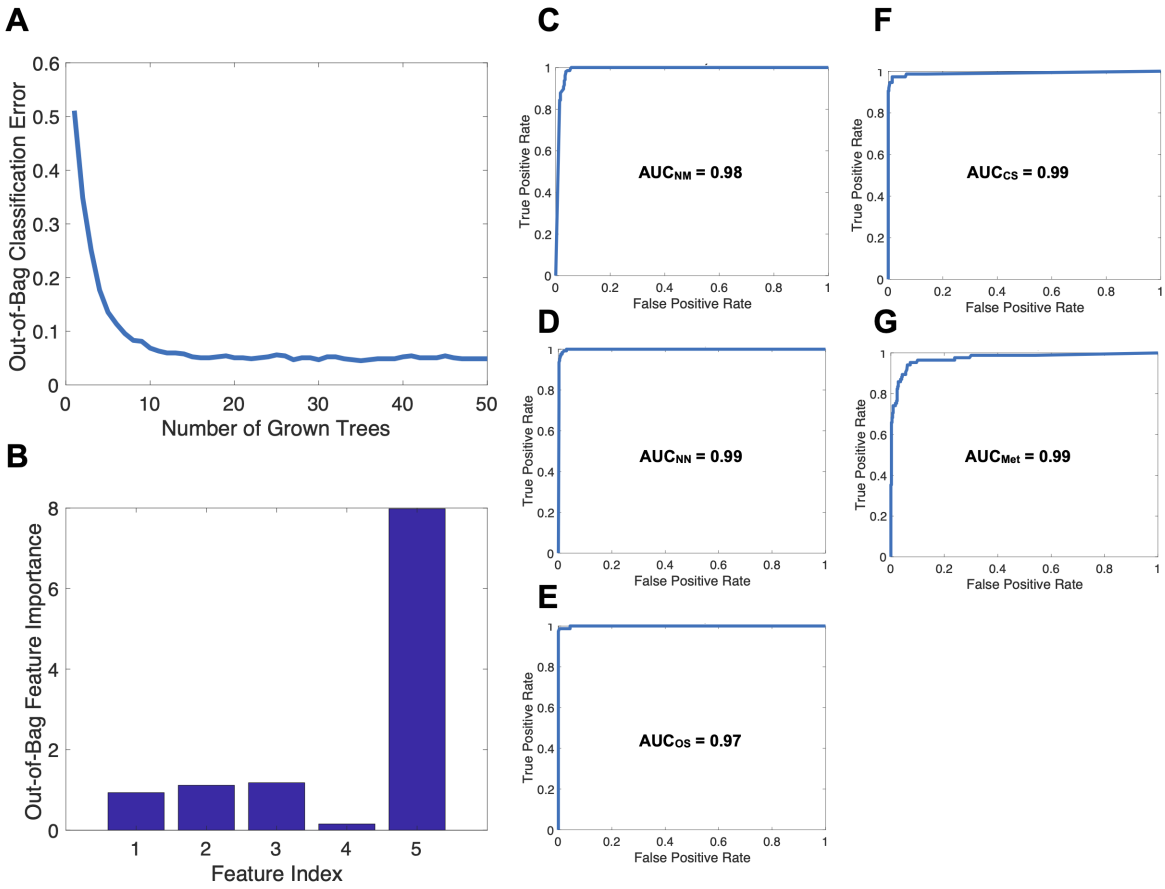

Figure 4.7: Bootstrap-aggregated (bagged) decision tree-based classification model using parameters from organic matrix morphometric analysis in conjunction with carbonate content in bone mineral matrix. A) Out-of-Bag (OOB) classification error vs number of grown trees. B) Out-of-Bag features importance versus features index (1 - AR, 2 - Φ, 3 - β_T, 4 - A, 5 - carbonate content of mineral portion of bone). C-G) ROC curves for diagnostic groups used in this study (NM –normal bone, NN –non-neoplastic pathological process including bone remodeling, OS –osteosarcoma, CS –chondrosarcoma, Met –metastatic cancer.

cunae, nearby collagen anisotropy, and angle between collagen and lacunae central axis) with carbonate content for each lacuna. Using these parameters for 791 lacunas, we constructed a classification model using a training data set consisting of randomly selected observations from the full dataset (70% of the original data) and retained a separate validation data set consisting of the remaining data (30% of the data).

By determining the minimum number of trees needed to reach an adequately reduced Out-of-Bag (OOB) classification error (Figure 4.7A), we ensure to not overfit the data. The final number of trees that was chosen for our classification model was 12. There was no significant difference in error when considering 11 or 13 trees.

Based on the results of OOB feature importance assessment (Figure 4.7B), AR, anisotropy, and angle between collagen and lacunae central axis provide similar help in determining final decisions. The most pathology indicative parameter appears to be carbonate content percentage as determined by SRS imaging.

In Figures 4.7C-G we display the results of receiver operating characteristic (ROC) curves for categories included in the analysis (normal, non-neoplastic pathology, osteosarcoma, chondrosarcoma, and metastatic cancer). All calculated areas under the curve (AUCs) were calculated to be above threshold to constitute a good classification model. Overall accuracy of predictions was calculated to be $\sim$92%.

In summary, the results of the classification model show that lacunae associated parameters obtained by morphometric analysis in conjunction with carbonate content for the mineral portion of bone can provide a good basis for assessing bone specimens in an intraoperative setting.

4.6 Summary and Outlook

Interrogation of bone specimens is severely limited by conventional histological methods due to their reliance on sectioning of tissue into 4-6 μm sections. Without the ability to visualize pathological processes, intraoperative consultations are hindered and can rely only on soft

tissue, if present. Meanwhile, patients undergo multiple surgeries that could potentially be prevented with the advent and implementation of adequate tools to assess bone samples in intraoperative settings. In this paper, we conduct the first study of this kind to demonstrate how non-linear optical techniques employing SRS, TPF, and SHG have a remarkable potential to provide much needed tools to surgeons, pathologists, and most importantly, patients.

By using SRS, we can visualize bone structure in a label-free and non-destructive manner. Being able to provide such information with relative ease and without compromising the availability of tissue is important in the context of an intraoperative setting as it preserves the tissue for subsequent molecular studies if they are deemed necessary.

TPF from acridine orange (AO) highlighted nuclei allows us to generate images that could be used similarly to those from H&E. Achieving non-destructive bone imaging allows intraoperative tissue assessment without challenges posed when trying to section mineralized bone. Using distinct Raman features of mineral components such as phosphate and carbonate, we can probe mineral components of bone and study how changes in mineral content correlate with bone pathology, including neoplastic processes. By collecting SHG from collagen fibers, we augment collected data with important information about surrounding collagen fiber organization. Additionally, we chose bone samples relevant to intraoperative settings, such as normal rib and mandible, fractured femur head, femur with avascular necrosis, and bone samples involved with primary cancer (e.g. osteosarcoma and chondrosarcoma) or metastatic cancer.

Our main findings show that carbonate content varies across different pathological categories and assists in identifying the cases where osteosarcoma is likely present. Additionally, morphometric analysis of bone organic matrix provides additional parameters (lacunae aspect ratio, angle of collagen relative to lacunae major axes, and collagen anisotropy) that prove to be useful in identifying cases where the organic matrix is abnormal, specifically in cases of abnormal bone healing/growth and metastatic cancer. We combine our techniques with a machine learning approach (Random Forest classification) and demonstrate that to-

gether, the parameters have potential utility in diagnostic pathology. The overall accuracy of 92% demonstrates that multimodal imaging and machine learning-based analysis of bony tissue has an immense potential to address the major gap in intraoperative pathology involving bony specimens.

BIBLIOGRAPHY

[1] Bo Huang, Hazen Babcock, and Xiaowei Zhuang. Breaking the Diffraction Barrier: Super-Resolution Imaging of Cells. *Cell*, 143(7):1047–1058, December 2010.

[2] M. Sauer. Localization microscopy coming of age: from concepts to biological impact. *Journal of Cell Science*, 126(16):3505–3513, August 2013.

[3] Rohit Bhargava. Infrared Spectroscopic Imaging: The Next Generation. *Applied spectroscopy*, 66(10):1091–1120, October 2012.

[4] Zanyar Movasaghi, Shazza Rehman, and Dr Ihtesham U. Rehman. Raman Spectroscopy of Biological Tissues. *Applied Spectroscopy Reviews*, 42(5):493–541, September 2007.

[5] C. Xu, W. Zipfel, J. B. Shear, R. M. Williams, and W. W. Webb. Multiphoton fluorescence excitation: new spectral windows for biological nonlinear microscopy. *Proceedings of the National Academy of Sciences*, 93(20):10763–10768, October 1996.

[6] Peter T. C. So, Chen Y. Dong, Barry R. Masters, and Keith M. Berland. Two-Photon Excitation Fluorescence Microscopy. *Annual Review of Biomedical Engineering*, 2(1):399–429, 2000.

[7] V E Centonze and J G White. Multiphoton excitation provides optical sections from deeper within scattering specimens than confocal imaging. *Biophysical Journal*, 75(4):2015–2024, October 1998.

[8] Fritjof Helmchen and Winfried Denk. Deep tissue two-photon microscopy. *Nature Methods*, 2(12):932–940, December 2005.

[9] Michael D. Cahalan, Ian Parker, Sindy H. Wei, and Mark J. Miller. Two-photon tissue imaging: seeing the immune system in a fresh light. *Nature reviews. Immunology*, 2(11):872–880, November 2002.

[10] F. Bestvater, E. Spiess, G. Stobrawa, M. Hacker, T. Feurer, T. Porwol, U. Berchner-Pfannschmidt, C. Wotzlaw, and H. Acker. Two-photon fluorescence absorption and emission spectra of dyes relevant for cell imaging. *Journal of Microscopy*, 208(2):108–115, 2002.

[11] Daniel R. Larson, Warren R. Zipfel, Rebecca M. Williams, Stephen W. Clark, Marcel P. Bruchez, Frank W. Wise, and Watt W. Webb. Water-Soluble Quantum Dots for Multiphoton Fluorescence Imaging in Vivo. *Science*, 300(5624):1434–1436, May 2003.

[12] Aikaterini Zoumi, Alvin Yeh, and Bruce J. Tromberg. Imaging cells and extracellular matrix in vivo by using second-harmonic generation and two-photon excited fluorescence. *Proceedings of the National Academy of Sciences*, 99(17):11014–11019, August 2002.

[13] Melissa C. Skala, Jayne M. Squirrell, Kristin M. Vrotsos, Jens C. Eickhoff, Annette Gendron-Fitzpatrick, Kevin W. Eliceiri, and Nirmala Ramanujam. Multiphoton Microscopy of Endogenous Fluorescence Differentiates Normal, Precancerous, and Cancerous Squamous Epithelial Tissues. *Cancer Research*, 65(4):1180–1186, February 2005.

[14] Maker P.D. Terhune, R.W. and C.M. Savage. Measurements of Nonlinear Light Scattering. *Physical Review Letters*, 14(4):681, 1965.

[15] Chi Zhang, Delong Zhang, and Ji-Xin Cheng. Coherent Raman Scattering Microscopy in Biology and Medicine. *Annual review of biomedical engineering*, 17:415–445, December 2015.

[16] Ji-Xin Cheng and Xiaoliang Sunney Xie. *Coherent Raman Scattering Microscopy*. CRC Press, April 2016.

[17] R.W. Boyd. Nonlinear Optics - 3rd Edition, 2003.

[18] W Denk, J. Strickler, and W. Webb. Two-photon laser scanning fluorescence microscopy. *Science*, 248(4951):73–76, April 1990.

[19] Esben Ravn Andresen, Pascal Berto, and Hervé Rigneault. Stimulated Raman scattering microscopy by spectral focusing and fiber-generated soliton as Stokes pulse. *Optics Letters*, 36(13):2387–2389, July 2011.

[20] Dan Fu, Gary Holtom, Christian Freudiger, Xu Zhang, and Xiaoliang Sunney Xie. Hyperspectral Imaging with Stimulated Raman Scattering by Chirped Femtosecond Lasers. *The Journal of Physical Chemistry B*, 117(16):4634–4640, April 2013.

[21] Andrew P. Evan, James E. Lingeman, Fredric L. Coe, Youzhi Shao, Joan H. Parks, Sharon B. Bledsoe, Carrie L. Phillips, Stephen Bonsib, Elaine M. Worcester, Andre J. Sommer, Sam C. Kim, William W. Tinmouth, and Marc Grynpas. Crystal-associated nephropathy in patients with brushite nephrolithiasis. *Kidney International*, 67(2):576–591, February 2005.

[22] Paul Campagnola. Second Harmonic Generation Imaging Microscopy: Applications to Diseases Diagnostics. *Analytical chemistry*, 83(9):3224–3231, May 2011.

[23] I. Freund, M. Deutsch, and A. Sprecher. Connective tissue polarity. Optical second-harmonic microscopy, crossed-beam summation, and small-angle scattering in rat-tail tendon. *Biophysical Journal*, 50(4):693–712, October 1986.

[24] Y. R. Shen. The Principles of Nonlinear Optics, John Wiley & Sons, New York, 1984, 576 pages. *John Wiley & Sons*, 4:576, 1984.

[25] Suzanne Z Powell. Intraoperative Consultation, Cytologic Preparations, and Frozen Section in the Central Nervous System. *Arch Pathol Lab Med*, 129:18, 2005.

[26] Shailja Chatterjee. Artefacts in histopathology. *Journal of Oral and Maxillofacial Pathology : JOMFP*, 18(Suppl 1):S111–S116, September 2014.

[27] D.N. Louis, H. Ohgaki, O.D. Wiestler, and W.K. Cavenee, editors. *WHO Classification of Tumours of the Central Nervous System, Fourth Edition*. World Health Organization and International Agency for Research on Cancer, fourth edition, 2007.

[28] Antonio Mazzoni and Marco Krengli. Historical development of the treatment of skull base tumours. *Reports of Practical Oncology and Radiotherapy*, 21(4):319–324, 2016.

[29] Hemen Jaju. Unfavourable results in skull base surgery. *Indian Journal of Plastic Surgery : Official Publication of the Association of Plastic Surgeons of India*, 46(2):239–246, 2013.

[30] Freddy T. Nguyen, Adam M. Zysk, Eric J. Chaney, Jan G. Kotynek, Uretz J. Oliphant, Frank J. Bellafiore, Kendrith M. Rowland, Patricia A. Johnson, and Stephen A. Boppart. Intraoperative Evaluation of Breast Tumor Margins with Optical Coherence Tomography. *Cancer research*, 69(22):8790–8796, November 2009.

[31] Carmen Kut, Kaisorn L. Chaichana, Jiefeng Xi, Shaan M. Raza, Xiaobu Ye, Elliot R. McVeigh, Fausto J. Rodriguez, Alfredo Quiñones-Hinojosa, and Xingde Li. Detection of human brain cancer infiltration ex vivo and in vivo using quantitative optical coherence tomography. *Science Translational Medicine*, 7(292):292ra100–292ra100, June 2015.

[32] Jason Bini, James Spain, Kishwer Nehal, Vikki Hazelwood, Charles DiMarzio, and Milind Rajadhyaksha. Confocal mosaicing microscopy of human skin ex vivo: spectral analysis for digital staining to simulate histology-like appearance. *Journal of Biomedical Optics*, 16(7), July 2011.

[33] Yuankai K. Tao, Dejun Shen, Yuri Sheikine, Osman O. Ahsen, Helen H. Wang, Daniel B. Schmolze, Nicole B. Johnson, Jeffrey S. Brooker, Alex E. Cable, James L. Connolly, and James G. Fujimoto. Assessment of breast pathologies using nonlinear microscopy. *Proceedings of the National Academy of Sciences*, 111(43):15304–15309, October 2014.

[34] Michael G. Giacomelli, Beverly E. Faulkner-Jones, Lucas C. Cahill, Tadayuki Yoshitake, Daihung Do, and James G. Fujimoto. Comparison of nonlinear microscopy and frozen section histology for imaging of Mohs surgical margins. *Biomedical Optics Express*, 10(8):4249, August 2019.

[35] Lucas C. Cahill, Michael G. Giacomelli, Tadayuki Yoshitake, Hilde Vardeh, Beverly E. Faulkner-Jones, James L. Connolly, Chi-Kuang Sun, and James G. Fujimoto. Rapid virtual H&E histology of breast tissue specimens using a compact fluorescence nonlinear microscope. *Laboratory investigation; a journal of technical methods and pathology*, 98(1):150–160, January 2018.

[36] Michael Jermyn, Kelvin Mok, Jeanne Mercier, Joannie Desroches, Julien Pichette, Karl Saint-Arnaud, Liane Bernstein, Marie-Christine Guiot, Kevin Petrecca, and Frederic Leblond. Intraoperative brain cancer detection with Raman spectroscopy in humans. *Science Translational Medicine*, 7(274):274ra19–274ra19, February 2015.

[37] Marcus T. Cicerone and Charles H. Camp Jr. Histological coherent Raman imaging: a prognostic review. *The Analyst*, 143(1):33–59, 2018. arXiv: 1709.07325.

[38] J.-X. Cheng and X. S. Xie. Vibrational spectroscopic imaging of living systems: An emerging platform for biology and medicine. *Science*, 350(6264):aaa8870–aaa8870, November 2015.

[39] Daniel A. Orringer, Balaji Pandian, Yashar S. Niknafs, Todd C. Hollon, Julianne Boyle, Spencer Lewis, Mia Garrard, Shawn L. Hervey-Jumper, Hugh J. L. Garton, Cormac O. Maher, Jason A. Heth, Oren Sagher, D. Andrew Wilkinson, Matija Snuderl, Sriram Venneti, Shakti H. Ramkissoon, Kathryn A. McFadden, Amanda Fisher-Hubbard, Andrew P. Lieberman, Timothy D. Johnson, X. Sunney Xie, Jay K. Trautman, Christian W. Freudiger, and Sandra Camelo-Piragua. Rapid intraoperative histology of unprocessed surgical specimens via fibre-laser-based stimulated Raman scattering microscopy. *Nature Biomedical Engineering*, 1(2):0027, February 2017.

[40] Todd C. Hollon, Spencer Lewis, Balaji Pandian, Yashar S. Niknafs, Mia R. Garrard, Hugh Garton, Cormac O. Maher, Kathryn McFadden, Matija Snuderl, Andrew P. Lieberman, Karin Muraszko, Sandra Camelo-Piragua, and Daniel A. Orringer. Rapid

Intraoperative Diagnosis of Pediatric Brain Tumors Using Stimulated Raman Histology. *Cancer Research*, 78(1):278–289, January 2018.

[41] Barbara Sarri, Flora Poizat, Sandro Heuke, Julien Wojak, Florence Franchi, Fabrice Caillol, Marc Giovannini, Marc Giovannini, Herve Rigneault, and Herve Rigneault. Stimulated Raman histology: one to one comparison with standard hematoxylin and eosin staining. *Biomedical Optics Express*, 10(10):5378–5384, October 2019.

[42] Lili Zhang, Yongzheng Wu, Bin Zheng, Lizhong Su, Yuan Chen, Shuang Ma, Qinqin Hu, Xiang Zou, Lie Yao, Yinlong Yang, Liang Chen, Ying Mao, Yan Chen, and Minbiao Ji. Rapid histology of laryngeal squamous cell carcinoma with deep-learning based stimulated Raman scattering microscopy. *Theranostics*, 9(9):2541–2554, 2019.

[43] F.-K. Lu, D. Calligaris, O. I. Olubiyi, I. Norton, W. Yang, S. Santagata, X. S. Xie, A. J. Golby, and N. Y. R. Agar. Label-Free Neurosurgical Pathology with Stimulated Raman Imaging. *Cancer Research*, 76(12):3451–3462, June 2016.

[44] Conor L. Evans and X. Sunney Xie. Coherent anti-stokes Raman scattering microscopy: chemical imaging for biology and medicine. *Annual Review of Analytical Chemistry (Palo Alto, Calif.)*, 1:883–909, 2008.

[45] Conor L. Evans, Xiaoyin Xu, Santosh Kesari, X. Sunney Xie, Steven T. C. Wong, and Geoffrey S. Young. Chemically-selective imaging of brain structures with CARS microscopy. *Optics Express*, 15(19):12076–12087, September 2007.

[46] Tobias Meyer, Norbert Bergner, Anna Medyukhina, Benjamin Dietzek, Christoph Krafft, Bernd F. M. Romeike, Rupert Reichart, Rolf Kalff, and Jürgen Popp. Interpreting CARS images of tissue within the C-H-stretching region. *Journal of Biophotonics*, 5(10):729–733, 2012.

[47] Wei Min, Christian W. Freudiger, Sijia Lu, and X. Sunney Xie. Coherent nonlinear optical imaging: beyond fluorescence microscopy. *Annual Review of Physical Chemistry*, 62:507–530, 2011.

[48] Julien Duboisset, Pascal Berto, Paulina Gasecka, Fatma-Zohra Bioud, Patrick Ferrand, Hervé Rigneault, and Sophie Brasselet. Molecular Orientational Order Probed by Coherent Anti-Stokes Raman Scattering (CARS) and Stimulated Raman Scattering (SRS) Microscopy: A Spectral Comparative Study. *The Journal of Physical Chemistry B*, 119(7):3242–3249, February 2015.

[49] Yong Yu, Prasanna V. Ramachandran, and Meng C. Wang. Shedding new light on lipid functions with CARS and SRS microscopy. *Biochimica et biophysica acta*, 1841(8):1120–1129, August 2014.

[50] T. Bocklitz, T. Meyer, M. Schmitt, I. Rimke, F. Hoffmann, F. von Eggeling, G. Ernst, O. Guntinas-Lichius, and J. Popp. Invited Article: Comparison of hyperspectral coherent Raman scattering microscopies for biomedical applications. *APL Photonics*, 3(9):092404, September 2018.

[51] Thomas W. Bocklitz, Firas Subhi Salah, Nadine Vogler, Sandro Heuke, Olga Chernavskaia, Carsten Schmidt, Maximilian J. Waldner, Florian R. Greten, Rolf Bräuer, Michael Schmitt, Andreas Stallmach, Iver Petersen, and Jürgen Popp. Pseudo-HE images derived from CARS/TPEF/SHG multimodal imaging in combination with Raman-spectroscopy as a pathological screening tool. *BMC Cancer*, 16, July 2016.

[52] Ruoyu He, Yongkui Xu, Lili Zhang, Shenghong Ma, Xu Wang, Dan Ye, and Minbiao Ji. Dual-phase stimulated Raman scattering microscopy for real-time two-color imaging. *Optica*, 4(1):44, January 2017.

[53] Andrew Francis, Kyla Berry, Yikai Chen, Benjamin Figueroa, and Dan Fu. Label-free pathology by spectrally sliced femtosecond stimulated Raman scattering (SRS) microscopy. *PLOS ONE*, 12(5):e0178750, May 2017.

[54] Ming Lai, Shui T. Lai, and Casimir Swinger. Single-grating laser pulse stretcher and compressor. *Applied Optics*, 33(30):6985–6987, October 1994.

[55] Benjamin Figueroa, Walter Fu, Tai Nguyen, Kseniya Shin, Bryce Manifold, Frank Wise, and Dan Fu. Broadband hyperspectral stimulated Raman scattering microscopy with a parabolic fiber amplifier source. *Biomedical Optics Express*, 9(12):6116–6131, December 2018.

[56] Minbiao Ji, Daniel A. Orringer, Christian W. Freudiger, Shakti Ramkissoon, Xiaohui Liu, Darryl Lau, Alexandra J. Golby, Isaiah Norton, Marika Hayashi, Nathalie Y. R. Agar, Geoffrey S. Young, Cathie Spino, Sandro Santagata, Sandra Camelo-Piragua, Keith L. Ligon, Oren Sagher, and X. Sunney Xie. Rapid, Label-Free Detection of Brain Tumors with Stimulated Raman Scattering Microscopy. *Science Translational Medicine*, 5(201):201ra119–201ra119, September 2013.

[57] Catharina Medrek, Fredrik Pontén, Karin Jirström, and Karin Leandersson. The presence of tumor associated macrophages in tumor stroma as a prognostic marker for breast cancer patients. *BMC cancer*, 12:306, July 2012.

[58] Shweta Aras and M. Raza Zaidi. TAMeless traitors: macrophages in cancer progression and metastasis. *British Journal of Cancer*, 117(11):1583–1591, November 2017.

[59] Massimo Salvi and Filippo Molinari. Multi-tissue and multi-scale approach for nuclei segmentation in H&E stained images. *BioMedical Engineering OnLine*, 17, June 2018.

[60] Juan C. Caicedo, Jonathan Roth, Allen Goodman, Tim Becker, Kyle W Karhohs, Matthieu Broisin, Molnar Csaba, Claire McQuin, Shantanu Singh, Fabian Theis, and Anne E. Carpenter. Evaluation of Deep Learning Strategies for Nucleus Segmentation in Fluorescence Images. *bioRxiv*, February 2019.

[61] Minbiao Ji, Spencer Lewis, Sandra Camelo-Piragua, Shakti H. Ramkissoon, Matija Snuderl, Sriram Venneti, Amanda Fisher-Hubbard, Mia Garrard, Dan Fu, Anthony C. Wang, Jason A. Heth, Cormac O. Maher, Nader Sanai, Timothy D. Johnson, Christian W. Freudiger, Oren Sagher, Xiaoliang Sunney Xie, and Daniel A. Orringer. Detection of human brain tumor infiltration with quantitative stimulated Raman scattering microscopy. *Science translational medicine*, 7(309):309ra163, October 2015.

[62] Louise Wilkinson, Val Thomas, and Nisha Sharma. Microcalcification on mammography: approaches to interpretation and biopsy. *The British Journal of Radiology*, 90(1069):20160594, January 2017.

[63] Madiha Naseem, Joshua Murray, John F. Hilton, Jason Karamchandani, Derek Muradali, Hala Faragalla, Chanele Polenz, Dolly Han, David C. Bell, and Christine Brezden-Masley. Mammographic microcalcifications and breast cancer tumorigenesis: a radiologic-pathologic analysis. *BMC Cancer*, 15(1):307, April 2015.

[64] G. Farshid, T. Sullivan, P. Downey, P. G. Gill, and S. Pieterse. Independent predictors of breast malignancy in screen-detected microcalcifications: biopsy results in 2545 cases. *British Journal of Cancer*, 105(11):1669–1675, November 2011.

[65] L Holmberg, Y N S Wong, L Tabár, A Ringberg, P Karlsson, L-G Arnesson, K Sandelin, H Anderson, H Garmo, and S Emdin. Mammography casting-type calcification and risk of local recurrence in DCIS: analyses from a randomised study. *British Journal of Cancer*, 108(4):812–819, March 2013.

[66] László Tabár, Hsiu-Hsi Chen, Stephen W Duffy, MF Yen, CF Chiang, Peter B Dean, and Robert A Smith. A novel method for prediction of long-term outcome of women with T1a, T1b, and 10-14 mm invasive breast cancers: a prospective study. *The Lancet*, 355(9202):429–433, February 2000.

[67] Laszlo Tabár, Hsiu-Hsi Tony Chen, M. F. Amy Yen, Tibor Tot, Tao-Hsin Tung, Li-Sheng Chen, Yueh-Hsia Chiu, Stephen W. Duffy, and Robert A. Smith. Mammographic tumor features can predict long-term outcomes reliably in women with 1-14-mm invasive breast carcinoma. *Cancer*, 101(8):1745–1759, October 2004.

[68] Huei-Shian Tsau, Amy Ming-Fang Yen, Jean Ching-Yuan Fann, Wendy Yi-Ying Wu, Cheng-Ping Yu, Sam Li-Sheng Chen, Sherry Yueh-Hsia Chiu, László Tabár, Wen-Hung Kuo, Hsiu-Hsi Chen, and King-Jen Chang. Mammographic tumour appearance and triple-negative breast cancer associated with long-term prognosis of breast cancer death: A Swedish Cohort Study. *Cancer Epidemiology*, 39(2):200–208, April 2015.

[69] Maria P. Morgan, Michelle M. Cooke, and Geraldine M. McCarthy. Microcalcifications Associated with Breast Cancer: An Epiphenomenon or Biologically Significant Feature of Selected Tumors? *Journal of Mammary Gland Biology and Neoplasia*, 10(2):181–187, April 2005.

[70] R F Cox, A Hernandez-Santana, S Ramdass, G McMahon, J H Harmey, and M P Morgan. Microcalcifications in breast cancer: novel insights into the molecular mechanism and functional consequence of mammary mineralisation. *British Journal of Cancer*, 106(3):525–537, January 2012.

[71] Siyoung Choi, Scott Coonrod, Lara Estroff, and Claudia Fischbach. Chemical and physical properties of carbonated hydroxyapatite affect breast cancer cell behavior. *Acta Biomaterialia*, 24:333–342, September 2015.

[72] S. O'Grady and M. P. Morgan. Microcalcifications in breast cancer: From pathophysiology to diagnosis and prognosis. *Biochimica et Biophysica Acta (BBA) - Reviews on Cancer*, 1869(2):310–320, April 2018.

[73] Carl Michael Büsing, Ulrich Keppler, and Volker Menges. Differences in microcalcification in breast tumors. *Virchows Archiv A*, 393(3):307–313, November 1981.

[74] L. Frappart, M. Boudeulle, J. Boumendil, Hu Chi Lin, I. Martinon, C. Palayer, Y. Mallet-Guy, D. Raudrant, A. Bremond, Y. Rochet, and J. Feroldi. Structure and composition of microcalcifications in benign and malignant lesions of the breast: Study by light microscopy, transmission and scanning electron microscopy, microprobe analysis, and X-ray diffraction. *Human Pathology*, 15(9):880–889, September 1984.

[75] L. Frappart, I. Remy, Hu Chi Lin, A. Bremond, D. Raudrant, B. Grousson, and J. L. Vauzelle. Different types of microcalcifications observed in breast pathology. *Virchows Archiv A*, 410(3):179–187, May 1987.

[76] Abigail S. Haka, Karen E. Shafer-Peltier, Maryann Fitzmaurice, Joseph Crowe, Ramachandra R. Dasari, and Michael S. Feld. Diagnosing breast cancer by using Raman spectroscopy. *Proceedings of the National Academy of Sciences of the United States of America*, 102(35):12371–12376, 2005.

[77] Marleen M. Kerssens, Pavel Matousek, Keith Rogers, and Nicholas Stone. Towards a safe non-invasive method for evaluating the carbonate substitution levels of hydroxyapatite (HAP) in micro-calcifications found in breast tissue. *The Analyst*, 135(12):3156, 2010.

[78] Anushree Saha, Ishan Barman, Narahara Chari Dingari, Luis H. Galindo, Abdus Sattar, Wendy Liu, Donna Plecha, Nina Klein, Ramachandra Rao Dasari, and Maryann Fitzmaurice. Precision of Raman Spectroscopy Measurements in Detection of Microcalcifications in Breast Needle Biopsies. *Analytical Chemistry*, 84(15):6715–6722, August 2012.

[79] R. Sathyavathi, Anushree Saha, Jaqueline S. Soares, Nicolas Spegazzini, Sasha McGee, Ramachandra Rao Dasari, Maryann Fitzmaurice, and Ishan Barman. Raman spectroscopic sensing of carbonate intercalation in breast microcalcifications at stereotactic biopsy. *Scientific Reports*, 5(1):9907, September 2015.

[80] Jennie A. M. R. Kunitake, Siyoung Choi, Kayla X. Nguyen, Meredith M. Lee, Frank He, Daniel Sudilovsky, Patrick G. Morris, Maxine S. Jochelson, Clifford A. Hudis, David A. Muller, Peter Fratzl, Claudia Fischbach, Admir Masic, and Lara A. Estroff. Correlative imaging reveals physiochemical heterogeneity of microcalcifications in human breast carcinomas. *Journal of Structural Biology*, 202(1):25–34, April 2018.

[81] R. Baker, K. D. Rogers, N. Shepherd, and N. Stone. New relationships between breast microcalcifications and cancer. *British journal of cancer*, 103(7):1034, 2010.

[82] O. Hassler. Microradiographic investigations of calcifications of the female breast. *Cancer*, 23(5):1103–1109, 1969.

[83] Robert Scott, Nicholas Stone, Catherine Kendall, Kalotina Geraki, and Keith Rogers. Relationships between pathology and crystal structure in breast calcifications: an in situ X-ray diffraction study in histological sections. *npj Breast Cancer*, 2(1):1–6, September 2016.

[84] Robert Scott, Catherine Kendall, Nicholas Stone, and Keith Rogers. Elemental vs. phase composition of breast calcifications. *Scientific Reports*, 7(1):136, March 2017.

[85] Renzo Vanna, Carlo Morasso, Beatrice Marcinnò, Francesca Piccotti, Emanuele Torti, Davide Altamura, Sara Albasini, Manuela Agozzino, Laura Villani, Luca Sorrentino, Oliver Bunk, Francesco Leporati, Cinzia Giannini, and Fabio Corsi. Raman Spectroscopy reveals that biochemical composition of breast microcalcifications correlates with histopathological features. *Cancer Research*, page canres.3204.2019, February 2020.

[86] Abigail S. Haka, Karen E. Shafer-Peltier, Maryann Fitzmaurice, Joseph Crowe, Ramachandra R. Dasari, and Michael S. Feld. Identifying microcalcifications in benign and malignant breast lesions by probing differences in their chemical composition using Raman spectroscopy. *Cancer research*, 62(18):5375–5380, 2002.

[87] Aicha Ben Lakhdar, Michel Daudon, Marie-Christine Mathieu, Alex Kellum, Corinne Balleyguier, and Dominique Bazin. Underlining the complexity of the structural and chemical characteristics of ectopic calcifications in breast tissues through FE-SEM and micro-FTIR spectroscopy. *Comptes Rendus Chimie*, 19(11):1610–1624, November 2016.

[88] Christian W. Freudiger, Wei Min, Brian G. Saar, Sijia Lu, Gary R. Holtom, Chengwei He, Jason C. Tsai, Jing X. Kang, and X. Sunney Xie. Label-free biomedical imaging with high sensitivity by stimulated Raman scattering microscopy. *Science (New York, N.Y.)*, 322(5909):1857–1861, December 2008.

[89] Dan Fu, Wenlong Yang, and Xiaoliang Sunney Xie. Label-free Imaging of Neurotransmitter Acetylcholine at Neuromuscular Junctions with Stimulated Raman Scattering. *Journal of the American Chemical Society*, 139(2):583–586, January 2017.

[90] Dan Fu, Yong Yu, Andrew Folick, Erin Currie, Robert V. Farese, Tsung-Huang Tsai, Xiaoliang Sunney Xie, and Meng C. Wang. *In Vivo* Metabolic Fingerprinting of Neutral Lipids with Hyperspectral Stimulated Raman Scattering Microscopy. *Journal of the American Chemical Society*, 136(24):8820–8828, June 2014.

[91] Dan Fu, Jing Zhou, Wenjing Suzanne Zhu, Paul W. Manley, Y. Karen Wang, Tami Hood, Andrew Wylie, and X. Sunney Xie. Imaging the intracellular distribution of tyrosine kinase inhibitors in living cells with quantitative hyperspectral stimulated Raman scattering. *Nature Chemistry*, 6(7):614–622, May 2014.

[92] Kseniya S. Shin, Andrew T. Francis, Andrew H. Hill, Mint Laohajaratsang, Patrick J. Cimino, Caitlin S. Latimer, Luis F. Gonzalez-Cuyar, Laligam N. Sekhar, Gordana Juric-Sekhar, and Dan Fu. Intraoperative assessment of skull base tumors using stimulated Raman scattering microscopy. *Scientific Reports*, 9(1):1–12, December 2019. Number: 1 Publisher: Nature Publishing Group.

[93] Benjamin Figueroa, Yikai Chen, Kyla Berry, Andrew Francis, and Dan Fu. Label-Free Chemical Imaging of Latent Fingerprints with Stimulated Raman Scattering Microscopy. *Analytical Chemistry*, 89(8):4468–4473, April 2017.

[94] Abdullah Chandra Sekhar Talari, Zanyar Movasaghi, Shazza Rehman, and Ihtesham ur Rehman. Raman Spectroscopy of Biological Tissues. *Applied Spectroscopy Reviews*, 50(1):46–111, January 2015.

[95] A. Saha, I. Barman, N. C. Dingari, S. McGee, Z. Volynskaya, L. H. Galindo, W. Liu, D. Plecha, N. Klein, R. R. Dasari, and M. Fitzmaurice. Raman spectroscopy: a real-time tool for identifying microcalcifications during stereotactic breast core needle biopsies. *Biomedical Optics Express*, 2(10):2792–2803, September 2011.

[96] Yasumasa Kato, Shigeyuki Ozawa, Chihiro Miyamoto, Yojiro Maehata, Atsuko Suzuki, Toyonobu Maeda, and Yuh Baba. Acidic extracellular microenvironment and cancer. *Cancer Cell International*, 13:89, September 2013.

[97] Veronica Huber, Chiara Camisaschi, Angela Berzi, Simona Ferro, Luana Lugini, Tiziana Triulzi, Alessandra Tuccitto, Elda Tagliabue, Chiara Castelli, and Licia Rivoltini. Cancer acidity: An ultimate frontier of tumor immune escape and a novel target of immunomodulation. *Seminars in Cancer Biology*, 43:74–89, April 2017.

[98] Márta Szaszák, Jiun Chiun Chang, Weinan Leng, Jan Rupp, David M. Ojcius, and Anne Myers Kelley. Characterizing the Intracellular Distribution of Metabolites in Intact Chlamydia-Infected Cells by Raman and Two-Photon Microscopy. *Microbes and infection / Institut Pasteur*, 15(0):461–469, June 2013.

[99] Yihui Shen, Fang Xu, Lu Wei, Fanghao Hu, and Wei Min. Live-cell quantitative imaging of proteome degradation by stimulated Raman scattering. *Angewandte Chemie (International Ed. in English)*, 53(22):5596–5599, May 2014.

[100] G. N. Tzimas, M. Afshar, A. Emadali, E. Chevet, H. Vali, and P. P. Metrakos. Correlation of cell necrosis and tissue calcification with ischemia/reperfusion injury after liver transplantation. *Transplantation Proceedings*, 36(6):1766–1768, July 2004.

[101] Manuel Scimeca, Elena Giannini, Chiara Antonacci, Chiara Adriana Pistolese, Luigi Giusto Spagnoli, and Elena Bonanno. Microcalcifications in breast cancer: an active phenomenon mediated by epithelial cells with mesenchymal characteristics. *BMC Cancer*, 14(1):286, April 2014.

[102] Patricia Lorena Arancibia Hernández, Teresa Taub Estrada, Alejandra López Pizarro, Maria Lorena Diaz Cisternas, and Carla Sáez Tapia. Calcificaciones mamarias: descripción y clasificación segn la 5.a edición BI-RADS. *Revista Chilena de Radiologia*, 22(2):80–91, April 2016.

[103] Laura Liberman and Jennifer H. Menell. Breast imaging reporting and data system (BI-RADS). *Radiologic Clinics of North America*, 40(3):409–430, v, May 2002.

[104] Emeli Mnsson, Leif Bergkvist, Gunilla Christenson, Carina Persson, and Fredrik Wärnberg. Mammographic casting-type calcifications is not a prognostic factor in unifocal

small invasive breast cancer: a population-based retrospective cohort study. *Journal of Surgical Oncology*, 100(8):670–674, December 2009.

[105] István Pálka, Katalin Ormándi, Szilvia Gaál, Krisztina Boda, and Zsuzsanna Kahán. Casting-type calcifications on the mammogram suggest a higher probability of early relapse and death among high-risk breast cancer patients. *Acta Oncologica*, 46(8):1178–1183, January 2007.

[106] Joann G. Elmore, Gary M. Longton, Patricia A. Carney, Berta M. Geller, Tracy Onega, Anna N. A. Tosteson, Heidi D. Nelson, Margaret S. Pepe, Kimberly H. Allison, Stuart J. Schnitt, Frances P. O'Malley, and Donald L. Weaver. Diagnostic Concordance Among Pathologists Interpreting Breast Biopsy Specimens. *JAMA*, 313(11):1122, March 2015.

[107] Jayawant N. Mandrekar. Receiver Operating Characteristic Curve in Diagnostic Test Assessment. *Journal of Thoracic Oncology*, 5(9):1315–1316, September 2010.

[108] Brigitte Wopenka and Jill D. Pasteris. A mineralogical perspective on the apatite in bone. *Materials Science and Engineering: C*, 25(2):131–143, April 2005.

[109] Marilyn M. Bui, Prudence Smith, Samuel V. Agresta, David Cheong, and G. Douglas Letson. Practical Issues of Intraoperative Frozen Section Diagnosis of Bone and Soft Tissue Lesions. *Cancer Control*, 15(1):7–12, January 2008.

[110] Poonam Bhaker, Harsh Mohan, Uma Handa, and Sudhir Kumar. Role of Intraoperative Pathology Consultation in Skeletal Tumors and Tumor-Like Lesions. *Sarcoma*, 2014, 2014.

[111] Eréndira G. Estrada-Villaseñor, Ernesto Delgado Cedillo, Luis Miguel Linares González, and Genaro Rico Martinez. Accuracy of intraoperative consultation for bone tumors: experience in an orthopedic hospital. *Journal of Orthopaedic Science*, 12(2):123–126, March 2007.

[112] Matthew T. Wallace, Patrick P. Lin, Justin E. Bird, Bryan S. Moon, Robert L. Satcher, and Valerae O. Lewis. The Accuracy and Clinical Utility of Intraoperative Frozen Section Analysis in Open Biopsy of Bone. *JAAOS - Journal of the American Academy of Orthopaedic Surgeons*, 27(11):410–417, June 2019.

[113] James C. Weaver, William Mershon, Martin Zadrazil, Marilyn Kooser, and David Kisailus. Wide-field SEM of semiconducting minerals. *Materials Today*, 13(10):46–53, October 2010.

[114] Furqan A. Shah. Micro-Raman Spectroscopy Reveals the Presence of Octacalcium Phosphate and Whitlockite in Association with Bacteria-Free Zones Within the Mineralized Dental Biofilm. *Microscopy and Microanalysis: The Official Journal of Microscopy Society of America, Microbeam Analysis Society, Microscopical Society of Canada*, 25(1):129–134, 2019.

[115] Yifei Liu, Inderchand Manjubala, Hanna Schell, Devakara R. Epari, Paul Roschger, Georg N. Duda, and Peter Fratzl. Size and habit of mineral particles in bone and mineralized callus during bone healing in sheep. *Journal of Bone and Mineral Research*, 25(9):2029–2038, 2010.

[116] Rebecca M. Hoerth, Michael Kerschnitzki, Marta Aido, Ingo Schmidt, Manfred Burghammer, Georg N. Duda, Peter Fratzl, Bettina M. Willie, and Wolfgang Wagermaier. Correlations between nanostructure and micromechanical properties of healing bone. *Journal of the Mechanical Behavior of Biomedical Materials*, 77:258–266, January 2018.

[117] Raghu Ambekar, Michael Chittenden, Iwona Jasiuk, and Kimani C. Toussaint. Quantitative second-harmonic generation microscopy for imaging porcine cortical bone: Comparison to SEM and its potential to investigate age-related changes. *Bone*, 50(3):643–650, March 2012.

[118] Rachel Genthial, Emmanuel Beaurepaire, Marie-Claire Schanne-Klein, Franoise Peyrin, Delphine Farlay, Cécile Olivier, Yohann Bala, Georges Boivin, Jean-Claude Vial, Delphine Débarre, and Aurélien Gourrier. Label-free imaging of bone multiscale porosity and interfaces using third-harmonic generation microscopy. *Scientific Reports*, 7(1):3419, June 2017.

[119] Eleftherios P Paschalis, Elizabeth Shane, George Lyritis, Grigoris Skarantavos, Richard Mendelsohn, and Adele L Boskey. Bone Fragility and Collagen Cross-Links. *Journal of bone and mineral research : the official journal of the American Society for Bone and Mineral Research*, 19(12):2000–2004, December 2004.

[120] Michael D. Morris and Gurjit S. Mandair. Raman Assessment of Bone Quality. *Clinical Orthopaedics and Related Research*, 469(8):2160–2169, August 2011.

[121] Catarina Costa Moura, Rahul S. Tare, Richard O. C. Oreffo, and Sumeet Mahajan. Raman spectroscopy and coherent anti-Stokes Raman scattering imaging: prospective tools for monitoring skeletal cells and skeletal regeneration. *Journal of The Royal Society Interface*, 13(118):20160182, May 2016.

[122] Mohamed Khalid, Tanujjal Bora, Ahmed Al Ghaithi, Sharanjit Thukral, and Joydeep Dutta. Raman Spectroscopy detects changes in Bone Mineral Quality and Collagen Cross-linkage in Staphylococcus Infected Human Bone. *Scientific Reports*, 8(1):9417, June 2018.

[123] Ather Farooq Khan, Muhammad Awais, Abdul Samad Khan, Sobia Tabassum, Aqif Anwar Chaudhry, and Ihtesham Ur Rehman. Raman Spectroscopy of Natural Bone and Synthetic Apatites. *Applied Spectroscopy Reviews*, 48(4):329–355, May 2013.

[124] Gurjit S Mandair and Michael D Morris. Contributions of Raman spectroscopy to the understanding of bone strength. *BoneKEy Reports*, 4, January 2015.

[125] Alexander J. Makowski, Mathilde Granke, Oscar D. Ayala, Sasidhar Uppuganti, Anita Mahadevan-Jansen, and Jeffry S. Nyman. Applying Full Spectrum Analysis to a Raman Spectroscopic Assessment of Fracture Toughness of Human Cortical Bone:. *Applied Spectroscopy*, July 2017.

[126] Mustafa Unal, Sasidhar Uppuganti, Calen J. Leverant, Amy Creecy, Mathilde Granke, Paul Voziyan, and Jeffry S. Nyman. Assessing glycation-mediated changes in human cortical bone with Raman spectroscopy. *Journal of Biophotonics*, 11(8):e201700352, 2018.

[127] Mustafa Unal, Sasidhar Uppuganti, Selin Timur, Anita Mahadevan-Jansen, Ozan Akkus, and Jeffry S. Nyman. Assessing matrix quality by Raman spectroscopy helps predict fracture toughness of human cortical bone. *Scientific Reports*, 9(1):1–13, May 2019.

[128] Karen A. Esmonde-White, Gurjit S. Mandair, Farhang Raaii, Jon A. Jacobson, Bruce S. Miller, Andrew G. Urquhart, Blake J. Roessler, and Michael D. Morris. Raman Spectroscopy of Synovial Fluid as a Tool for Diagnosing Osteoarthritis. *Journal of biomedical optics*, 14(3):034013, 2009.

[129] Dan Faibish, Susan M. Ott, and Adele L. Boskey. Mineral Changes in Osteoporosis A Review. *Clinical orthopaedics and related research*, 443:28–38, February 2006.

[130] Hao Ding, Jeffry S. Nyman, Julie A. Sterling, Daniel S. Perrien, Anita Mahadevan-Jansen, and Xiaohong Bi. Development of Raman spectral markers to assess metastatic bone in breast cancer. *Journal of Biomedical Optics*, 19(11):111606, 2014.

[131] Chi Zhang, Paul T. Winnard Jr, Sidarth Dasari, Scott L. Kominsky, Michele Doucet, Swaathi Jayaraman, Venu Raman, and Ishan Barman. Label-free Raman spectroscopy provides early determination and precise localization of breast cancer-colonized bone alterations. *Chemical Science*, 9(3):743–753, 2018.

[132] Todd C. Hollon, Balaji Pandian, Arjun R. Adapa, Esteban Urias, Akshay V. Save, Siri Sahib S. Khalsa, Daniel G. Eichberg, Randy S. D'Amico, Zia U. Farooq, Spencer Lewis, Petros D. Petridis, Tamara Marie, Ashish H. Shah, Hugh J. L. Garton, Cormac O. Maher, Jason A. Heth, Erin L. McKean, Stephen E. Sullivan, Shawn L. Hervey-Jumper, Parag G. Patil, B. Gregory Thompson, Oren Sagher, Guy M. McKhann, Ricardo J. Komotar, Michael E. Ivan, Matija Snuderl, Marc L. Otten, Timothy D. Johnson, Michael B. Sisti, Jeffrey N. Bruce, Karin M. Muraszko, Jay Trautman, Christian W. Freudiger, Peter Canoll, Honglak Lee, Sandra Camelo-Piragua, and Daniel A. Orringer. Near real-time intraoperative brain tumor diagnosis using stimulated Raman histology and deep neural networks. *Nature Medicine*, 26(1):52–58, January 2020.

[133] Kseniya S. Shin, Mint Laohajaratsang, Shuaiqian Men, Benjamin Figueroa, Suzanne M. Dintzis, and Dan Fu. Quantitative chemical imaging of breast calcifications in association with neoplastic processes. *Theranostics*, 10(13):5865–5878, 2020.

[134] Andy Y. Shih, Jonathan D. Driscoll, Patrick J. Drew, Nozomi Nishimura, Chris B. Schaffer, and David Kleinfeld. Two-Photon Microscopy as a Tool to Study Blood Flow and Neurovascular Coupling in the Rodent Brain:. *Journal of Cerebral Blood Flow & Metabolism*, February 2012.

[135] Stuart Berg, Dominik Kutra, Thorben Kroeger, Christoph N. Straehle, Bernhard X. Kausler, Carsten Haubold, Martin Schiegg, Janez Ales, Thorsten Beier, Markus Rudy, Kemal Eren, Jaime I. Cervantes, Buote Xu, Fynn Beuttenmueller, Adrian Wolny, Chong Zhang, Ullrich Koethe, Fred A. Hamprecht, and Anna Kreshuk. ilastik: interactive machine learning for (bio)image analysis. *Nature Methods*, 16(12):1226–1232, December 2019.

[136] Arezki Boudaoud, Agata Burian, Dorota Borowska-Wykrt, Magalie Uyttewaal, Roman Wrzalik, Dorota Kwiatkowska, and Olivier Hamant. FibrilTool, an ImageJ plug-in to quantify fibrillar structures in raw microscopy images. *Nature Protocols*, 9(2):457–463, February 2014.

[137] N. Pernick. Chondrosarcoma (primary, secondary, periosteal).

[138] Xiaohong Bi, Julie A. Sterling, Alyssa R. Merkel, Daniel S. Perrien, Jeffry S. Nyman, and Anita Mahadevan-Jansen. Prostate cancer metastases alter bone mineral and matrix composition independent of effects on bone architecture in mice–a quantitative study using microCT and Raman spectroscopy. *Bone*, 56(2):454–460, October 2013.

[139] S. Stewart, D. A. Shea, C. P. Tarnowski, M. D. Morris, D. Wang, R. Franceschi, D.-L. Lin, and E. Keller. Trends in early mineralization of murine calvarial osteoblastic

cultures: a Raman microscopic study. *Journal of Raman Spectroscopy*, 33(7):536–543, July 2002.

[140] Barbara R. McCreadie, Scott J. Hollister, Mitchell B. Schaffler, and Steven A. Goldstein. Osteocyte lacuna size and shape in women with and without osteoporotic fracture. *Journal of Biomechanics*, 37(4):563–572, April 2004.

[141] Leo Breiman. Random Forests. *Machine Learning*, 45(1):5–32, October 2001.